UNIVERSITY OF MOLISE

Department of Medicine and Health Sciences "V. Tiberio"

PhD in
TRANSLATIONAL AND CLINICAL MEDICINE
XXXIII CYCLE

SDS-Areas-06-09:
MED/36 IMAGING AND RADIOTHERAPY
ING-IND/11 ENVIRONMENTAL TECHNICAL PHYSICS

PhD Thesis

MODELLING HEAT TRANSFER IN TISSUES TREATED WITH THERMAL ABLATION

Tutors:
Prof. Luca Brunese

Prof. Giuseppe Peter Vanoli

PhD Student:
Claudio Tucci
160495

Coordinator:
Prof. Marco Sarchiapone

Academic Year 2019/2020

ACKNOWLEDGMENTS

I want to thank:

- The Department of Medicine and Health Sciences "V. Tiberio" (DIMES) of University of Molise,
- Prof. Enrique Berjano and Dr. Macarena Trujillo of the Universitat Politècnica de València, Valencia (UPV) to have given to me the opportunity and the honor to work with him and his research team at UPV,
- Prof. Assunta Andreozzi and Dr. Marcello Iasiello for their continuous support during all the three years of my PhD and for the contribution to this thesis work.

Finally, a special thanks to Prof. Luca Brunese and Prof. Giuseppe Peter Vanoli, who gave me the opportunity to develop my doctorate project in these three years.

ABSTRACT

Thermal ablation is more and more recognized as an important alternative in cancer treatments, for which the most common procedures followed are surgery, chemotherapy, and radiotherapy. Nevertheless, these common techniques pose critical issues such as: they are too invasive for human body, they can reveal serious side effects and are expensive in terms of financial costs for the national health service. Thermal ablation of tumors, instead, is a minimally invasive treatment option for cancer, with certain advantages such as minor side effects, shorter hospital stays and consequently lower costs. It consists in focusing an energy source (commonly radiofrequency or microwave) in the target zone (the tumoral tissue) by means of a probe, that causes the tumor destruction. Generally, the complete necrosis of tissue happens instantaneously at temperatures over about 60 °C, but lower temperatures with longer exposure times can be achieved. The most common approach is a percutaneous treatment performed with the aid of imaging techniques. On the other hand, the main shortcoming of performing a thermal ablation is to not achieve the complete tissue ablation, so the risk of a tumor recurrence becomes higher. In this context, an in-depth knowledge of thermal therapy physics has a key role in modelling heat transfer in thermal therapies, in order to develop more and more accurate bioheat models for clinical applications, predicting the final necrotic tissue diameters and volumes. Moreover, the lack of experimentation in this field, makes bioheat models even more significant. The first simple bioheat model was developed in 1948 by Harry H. Pennes and it is still widely used, but it has some shortcomings that make the equation not so accurate. For this reason, over the years it has been modified and more complex models have been developed.

In this thesis work, a general overview of the different employed techniques in hyperthermia treatments of biological tissues and in particular tumors is first of all introduced, together with techniques used to estimate thermal damage.

Next, in the second chapter, a wide state-of-the-art of how the distinct bioheat models have been modified over the years when applied in various hyperthermia treatments of cancer, is described.

In chapter three, transient bioheat equations based on different bioheat models, such as Pennes' model, and three porous media-based model are compared, where the porosity is the volume fraction of blood in the entire tissue domain. The considered porous media-based models are the Local Thermal Non-Equilibrium equations (LTNE), the Local Thermal Equilibrium equation (LTE), and the three-energy equations model. The models are implemented to a biological tissue modelled as a sphere with liver tissue properties. The effects of thermal ablation on the living tissue are included with a spherical energy source at the sphere center. Governing equations with the appropriate boundary conditions are solved with the finite-element software COMSOL Multiphysics®. Results are presented in terms of temperature profiles in the biological tissue, to appreciate differences due to the various bioheat models, concluding that LTNE model is preferable because it is a good compromise between accuracy and complexity.

Thus, in the next chapter, the LTNE model is applied to the same spherical biological model with tumoral properties, to investigate the pulsating energy source effects modeled with references to a cosine function with different frequencies, and such different heating protocols are compared at equal delivered energy, namely, different heating times at equal maximum power. The results are shown in terms of tissue

temperature and percentage of necrotic tissue obtained. The most powerful result achieved using a pulsating heat source instead of a constant one is the decreasing of maximum temperature in any considered case, even reaching about 30% lower maximum temperatures. Furthermore, the evaluation of tissue damage at the end of treatment shows that pulsating heat allows to necrotize the same tumoral tissue area of the non-pulsating heat source. In addition, a more complex model is developed to study a pulsating protocols application for radiofrequency ablation (RFA) of in vivo liver tissue using a cooled electrode and three different voltage levels. Three distinct heat transfer models coupled to the electrical problem are compared: the simplest but less realistic Pennes' equation and two porous media-based models, i.e., the LTNE and LTE models, both modified to take into account two-phase water vaporization (tissue and blood). Moreover, different blood volume fractions in liver are considered and the blood velocity is modeled to simulate a vascular network. The results in terms of coagulation transverse diameters and temperature fields at the end of the application show significant differences, especially between Pennes and the modified LTNE and LTE models at high voltage level. The new modified porous media-based models cover the ranges found in the few in vivo experimental studies in the literature and are closer to the published results with similar in vivo protocol. The same model is applied considering tumoral tissue surrounded by healthy tissue and the outcomes show relevant differences when the tumor is included in the model. Thus, the different electrical conductivity and thermal properties between the two types of tissues play a fundamental role in the outcomes.

In the final chapter five, the previous LTNE modified model is applied to a spherical tumoral tissue, in order to investigate the effects of different antennas configurations in thermal ablation. Single, double, and triple antennas arrangements are modelled in order to simulate the hepatic cancer treatment, which often requires the destruction of large volume lesions. Furthermore, different blood volume fractions and blood vessels are considered. The results show that using multiple antennas instead of a single antenna offers a potential solution for creating ablation zones with larger dimensions and to allow at the same time to have lower maximum tissue temperatures in all the cases compared to the single antenna configuration.

NOMENCLATURE

Latin letters		Units
a	volumetric transfer area between blood and tissue	m^{-1}
a_c	antenna constant	m^{-1}
A	kinetic energy frequency factor	s^{-1}
A_{tm}	area of the tumor	m^2
c	specific heat	$J\ kg^{-1}\ K$
c_{cell}	living cells concentration	m^{-1}
c_v	nanoparticle concentration in the blood flow	$kg\ l^{-1}$
C_w	water content	-
d	blood vessel diameter	m
d_c	coagulation diameter	m
E	modulus of the electric field	$V\ m^{-1}$
$\mathbf{E}$	electric field vector	$V\ m^{-1}$
E_{RF}	applied radiofrequency energy	J
f	frequency	Hz
$f_t(c_v)$	source term caused by alternating magnetic field	$W\ m^{-3}$
F	function depending on the radiative heat transfer	$W\ m^{-2}$
g	function depending on the radiative heat transfer	$W\ m^{-3}$
G	incident radiation	$W\ m^{-2}$
h	interfacial heat transfer coefficient	$W\ m^{-2}\ K^{-1}$
h_{fg}	product of water latent heat of vaporization and water density at 100°C	$J\ m^{-3}$
h_r	thermal convective coefficient	$W\ m^{-2}\ K^{-1}$
h_v	volumetric heat transfer coefficient	$W\ m^{-3}\ K^{-1}$
$\mathbf{H}$	magnetic field vector	T
I	scattered diffuse intensity	$W\ m^{-2}$
I_0	intensity of radiation	$W\ m^{-2}$
I_{ac}	local acoustic intensity	$W\ m^{-2}$
j_0	current density	$A\ m^{-2}$
k	thermal conductivity	$W\ m^{-1}\ K^{-1}$
k_{dis}	thermal dispersion conductivity	$W\ m^{-1}\ K^{-1}$
k_r	radiative thermal conductivity	$W\ m^{-1}\ K^{-1}$
l	length of skin tissue	m
L	specific thermal effects of chemical conversions	$m^2\ s^{-2}$
L_p^{LF}	lymphatic permeability	$m\ Pa^{-1}\ s^{-1}$
n	refractive index	-
n_{inj}	total number of injection points	-
n_{np}	number of nanoparticles	-
$N_{roll\text{-}off}$	number of roll-offs	–
P	transmitted antenna power	W
P_t	thermal damage probability	-
q	heat flux	$W\ m^{-2}$
q_c	convective heat flux	$W\ m^{-2}$

q_r	radiative heat flux	W m^{-2}
Q	power density	W m^{-3}
r	spatial coordinate	m
r_0	electrode radius	m
r_1	radius of the external sphere	m
r_2	radius of internal heated sphere in the single antenna configuration	m
r_3	radius of internal heated spheres in the double antennas configuration	m
r_4	radius of internal heated spheres in the triple antennas configuration	m
r_{dist}	tissue/outer surface relative distance	m
$\bar{r}$	distance covered by the heat generated by nanoparticles	m
r_{inj}	radial distance of the injection	m
r_{np}	mean radius of nanoparticles	m
R_1	heating zone radius	m
R_2	external radius of spherical tissue	m
R_g	universal gas constant	J mol^{-1} K^{-1}
R_{mil}	radius of magnetic loop	m
R_{CEM}	CEM_{43} criterion variable	-
S	antenna constant	m^{-1}
SAR	Specific Absorption Rate	W kg^{-1}
t	time	s
t_{on}	total time the generator is “on”	s
$t_{roll\text{-}off}$	time of first roll-off	s
t_{st}	steady state heating time	s
t_{pul}	total pulsating heating time	s
T	temperature	K
T_0	initial temperature	K
T_p	period	s
T_r	coolant temperature	K
T^*	dimensionless period	-
$\mathbf{u}$	velocity vector	m s^{-1}
u	velocity component	m s^{-1}
$u_q(t)$	step function	-
V	voltage	V
w	velocity component	m s^{-1}
W	tissue water density	kg m^{-3}
x	spatial coordinate	m
y	spatial coordinate	m
z	spatial coordinate	m
Z	Impedance	Ω

Greek letters

α	absorption coefficient	Np Hz^{-1} m^{-1}
β	extinction coefficient	m^{-1}
β_d	coefficient depending on thermal damage	-
α_{diff}	effective thermal diffusivity	m^2 s^{-1}

δ_Λ	parameter that refers to the microvascular network	-
ΔH	activation energy	J mol^{-1}
γ	water latent heat constant	J kg^{-1}
Φ	phase function	-
Γ	coordinates index	-
Γ_f	Euler gamma function	-
ε	porosity	-
θ	nanoparticles concentration	-
χ''	imaginary part of susceptibility of the magnetic nanoparticles	-
ρ	density	kg m^{-3}
P	arithmetic average of each segment contained into the tumor	m
ψ	density of nanoparticles on the vascular walls	l m^{-2}
σ	electric conductivity	S m^{-1}
σ_s	Stefan-Boltzmann constant	W m^{-2} K^{-4}
τ	relaxation time	s
τ_q	phase-lag of the heat flux	s
τ_T	phase-lag of temperature gradient	s
μ_{cr}	critical cosine of an angle	-
μ_0	dielectric vacuum permeability	H m^{-1}
ω	blood perfusion	s^{-1}
ω_{b0}	constant blood perfusion	s^{-1}
ω_p	pulsation	s^{-1}
ω_{p0}	reference pulsation	s^{-1}
ω_p^*	dimensionless pulsation	-
ω_{Pennes}	mean blood perfusion	s^{-1}
ω_{tr}	nanoshell transport albedo	-
Ω	solid angle	-
$\Omega(t)$	tissue injury degree	-

Subscripts

∞	far away from heating focus
a	arterial
b	blood
$conv$	convective
cr	critical
ch	channel conversion
dis	dispersion
e	effective

E	energy to vaporize water
ext	external
fat	fat
g	gas phase
l	liquid phase
laser	laser
max	maximum
met	metabolism
muscle	muscle
np	nanoparticles
p	probe
perf	perfusion
ref	reference
t	tissue
tot	total
tm	tumor
v	venous

1.

INTRODUCTION

1. INTRODUCTION

The word “hyperthermia” is from Greek “ὑπέρ”, *hyper* meaning “above” or “over”, and “θερμός”, *thermos*, meaning “hot”, and it can be defined as temperature increase in human body over the physiological average of about 37 °C at armpit or 37.5 °C in rectum [1]. Most people in the world, throughout their lives, have been faced problems related to hyperthermia, which can be referred to failed thermoregulation, fever, or to clinical treatments, which will be discussed in this work.

1.1. Hyperthermia applied in biological tissues

A generic overview of clinical treatments related to hyperthermia is presented in Fig. 1.

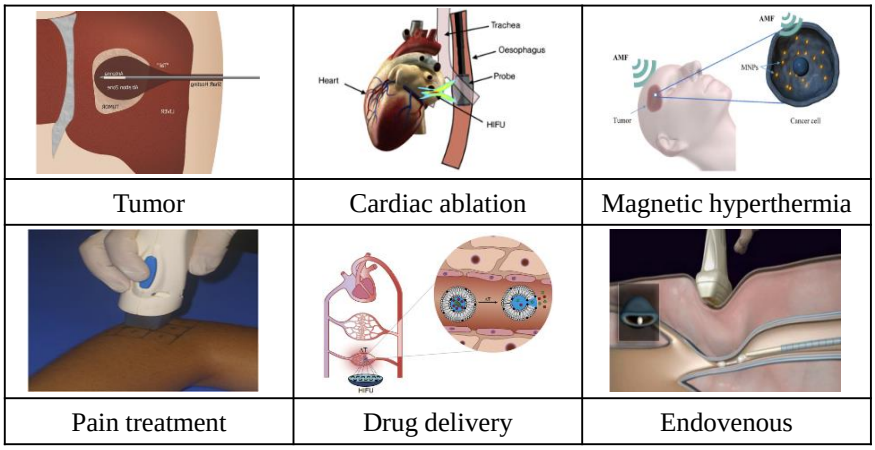

Figure 1. Different hyperthermia clinical treatments.

Tissue necrosis occurs over a threshold temperature depending on many variables [2], so, heat can be used to induce necrosis in tumor cells. Induced heat can be employed also in arrhythmias treatment such as atrial fibrillation by using heat to destroy abnormal pathways of electric conduction [3]. Magnetic hyperthermia is tumor treatment which consists in temperature gradients caused by magnetic nanoparticles subject to a high-frequency magnetic field [4]. Hyperthermia is applied for pain treatment [5] and drug delivery too [6]. Finally, varicose veins can be treated with hyperthermia since heat can destroy veins and block blood circulation [7].

1.2. Hyperthermia in cancer treatment

During the years, many studies have been carried out on the clinical application of hyperthermia in cancer therapy. Hyperthermia treatment is nowadays recognized as the fourth additional cancer therapy technique following surgery, chemotherapy and radiation techniques. In this type of cancer treatment tissue is exposed to high temperatures that can damage and kill cancer cells, usually with minimal injury to normal tissues [8]. The classification of the different hyperthermia cancer treatments is resumed in Fig. 2.

According to a first classification, three kinds of hyperthermia treatment are identified depending on the

temperature achieved in the tissue: the adjuvant hyperthermia, the real hyperthermia, and the ablative hyperthermia. Throughout the first type of treatment, temperatures of 38-41 °C are achieved; this treatment is used together with other therapies such as radiation therapy and chemotherapy, obtaining better positive results, and at the same time reducing side effects.

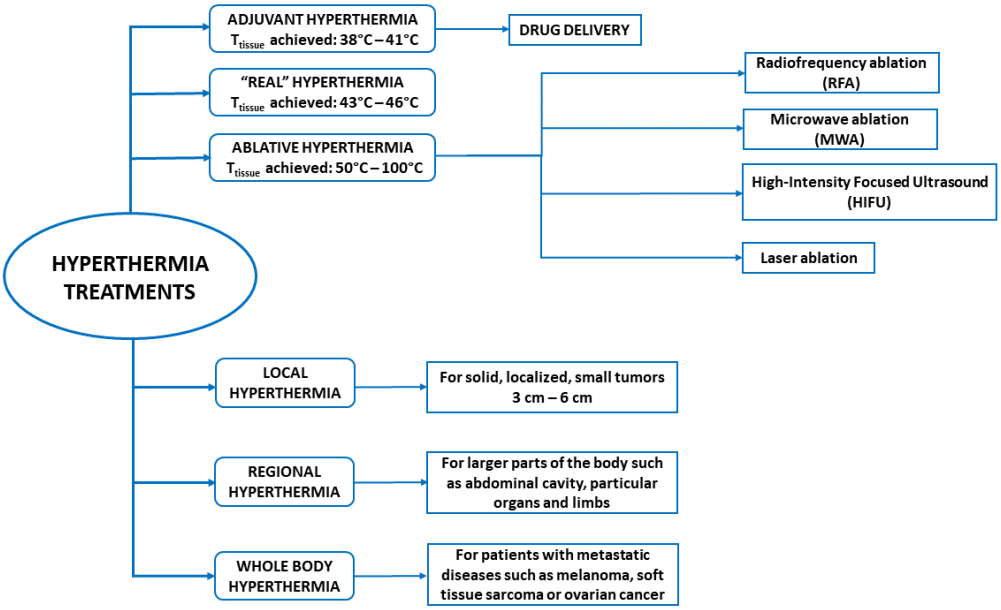

Figure 2. Classification of hyperthermia cancer treatments.

Hyperthermia is defined "real" when temperatures of 43-46 °C are reached. In this case, the irreversible cellular damage is obtained without tissue necrosis, by means of electromagnetic fields applied for 40-60 minutes. Finally, during the ablative hyperthermia treatment, temperatures raise up to 50-100 °C in a few minutes, causing the complete necrosis of tissues. Thermo-ablative techniques can be performed by using different forms of electromagnetic energy, in particular in terms of radiofrequencies (Radio Frequency Ablation, RFA), microwaves (MicroWave Ablation, MWA), acoustic waves or laser energy. The first technique uses AC current with typical frequencies of about 500 kHz, while in the second procedure frequencies are between 900 MHz and 2.5 GHz. Acoustic energy concerns a high-precision procedure known as High-Intensity Focused Ultrasound (HIFU); the focused ultrasounds can enhance tissue temperature very quickly, causing the necrosis of the tissue itself. Laser energy is employed in photocoagulation that uses optical fiber to deliver laser energy in the tumor. All these procedures are known as minimally or non-invasive treatments, involve fewer complications, a shorter hospital stay, and are potentially cheaper [9,10]. Moreover, hyperthermia therapies can be classified into three categories: local, regional, or whole-body hyperthermia [8]. The first is generally employed for solid, localized small tumors (≤ 3 cm up to 5-6 cm) and can be applied by external, intraluminal, or interstitial applicators. Usually microwaves, radio waves or ultrasounds are focused on the treatment volume. Regional hyperthermia is used for heating larger parts of the body and it is often applied in advanced tumors treatment, in particular when they are situated in the major and minor pelvis, abdomen or thighs and the temperature increase is limited to 41-42 °C. The deep-seated tumors are heated by means of external applicators, consisting of

antennas emitting microwave or radiofrequency energy**.** Regional hyperthermia can also be combined with cytostatic drugs and in this case, the temperature must be lower. Whole-body hyperthermia is an opportunity for patients with metastatic disease such as melanoma, soft tissue sarcoma or ovarian cancer. With this method, cancerous cells are destroyed or sensitized to drugs thanks to high temperatures applied to the whole organism. For this purpose, thermal chambers, hot water blankets or infrared radiators are used, increasing temperature to about 42 °C. Another important role played by hyperthermia regards the improvement of drug delivery and its efficacy in tumors. In fact, the traditional drug delivery is limited, and drugs do not reach the target volume in sufficient quantities to be efficacious [11]. Moreover, even when drug reaches the site of the tumor, it is very difficult to reach all tumor cells, because of the abnormal properties of their vasculature, such as the large intravascular distances and arteriovenous shunting [12,13]. It has been shown that in the temperature range of 39-42 °C profound physiological effects occur in tumors that can mediate enhancement in drug delivery [14] and there are many reports demonstrating that temperatures in this range increase tumor oxygenation and vascular permeability [15,16]. Furthermore, there are many preclinical reports showing that the combination of intravenous free drugs with hyperthermia improves antitumor effects [17] and a phase III trial from Europe [18] proved that chemotherapy combined with hyperthermia can improve local tumor control and progression free survival in patients with locally advanced soft tissue sarcomas compared to chemotherapy alone.

1.3. Evaluation of thermal damage

As it is resumed in Fig. 3, different phenomena are involved during hyperthermia treatments. Starting from a body set temperature of about 37 °C, vessel dilation due to thermal expansion and blood perfusion augmentation can occur up to 41 °C; at these temperatures, damages are avoided by cells answer. Irreversible damage starts between 41 °C and 46 °C, while with longer exposure times necrosis starts to become significant. Hypoxia, thrombosis formation and ischemia occur up to 52 °C, with fewer nutrients delivery. At about 60 °C, it is possible to appreciate protein denaturation and plasma membrane melting, thus cells necrosis is achieved. Over this temperature, other interesting phenomena happen. Between 60 °C and 100 °C, tissue desiccation starts, while at about 100 °C vaporization of water content happens. Over 100 °C carbonization will be achieved if temperature becomes very high (say, about 200 °). So, smoke is produced due to partial oxidation of hydrocarbons included in the tissue.

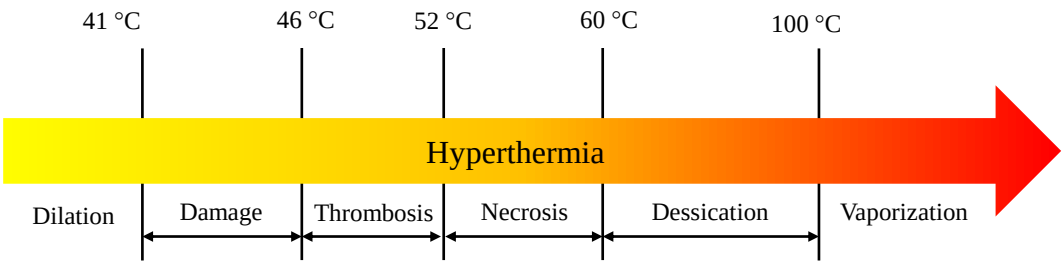

Figure 3. Involved phenomena in hyperthermia treatments.

From the heat transfer point of view, tissue necrosis is achieved as the necessary values of temperature and exposure time are obtained. Indeed, it is not sufficient to apply very large amounts of heat rates if these refer to short application times. This means that a criterion that considers both temperature and time is needed, and the thermal dose concept has been introduced through the years to overcome this issue. This concept is very important, as for example pointed out in Bourdon et al. [19] in a study about the relationship between skin exposure time, cooling duration, and temperatures of hot cups, or in Abraham et al. [20, 21], in which the authors derive correlations between exposure time and temperature conditions that cause irreversible thermal injury for skin burns. A comprehensive overview of cancer treatment hyperthermia thermal doses can be found in Dewhirst et al. [22]. The question of an appropriate thermal dose estimation has been highlighted by Sapareto and Dewey [23]. Starting from a discussion about treatments performed in too dispersed conditions in terms of temperature and time, they present a procedure to calculate an equivalent thermal dose that collects both temperature and exposure time. This thermal dose is chosen as the exposure time needed to achieve tissue damage under a prefixed reference temperature, that is chosen to be 43 °C in their work [23]. This criterion is called the Cumulative Equivalent Minutes at 43 °C (CEM_{43}). The equivalent time is obtained by combining temperature vs. time during treatment together with a mathematical description of time-temperature relationship for thermal inactivation or damage. In their model, it is obvious that the higher the temperature, the shorter the required heating time. For both in vivo and vitro system, that refer to situations with phenomena in living systems and reproduced in test tubes, respectively, an exponential relationship between two generic times t_1 and t_2 with temperatures of T_1 and T_2 has been reported starting from thermodynamics of heat inactivation [24].

$$t_1 = t_2 R_{CEM}^{(T_1 - T_2)} \tag{1}$$

$$R_{CEM} = e^{-\Delta H / [2T(T+1)]} \tag{2}$$

where ΔH represents the activation energy, T is the applied temperature, while the number 2 in Eq. (2) approximates the universal gas constant in cal/K mol. The variable R_{CEM} represents the inverse of the relative decrease for the inverse of the slope on the exponential portion of the heat inactivation survival curve for a one degree increase in temperature [24]. Dewey et al. [24] reported that R_{CEM} = 0.50 for Chinese Hamster Ovary (CHO) cells between 43 °C and 46 °C. In Sapareto and Dewey [23], the variable R_{CEM} can be assumed constant with an error of less than 2% if temperatures are between 37 and 46 °C. This variable is usually from 0.4 to 0.8 above 43 °C, and it includes a factor of 2 too if temperatures are below 43 °C. Based on this, Sapareto and Dewey [23] assumed R_{CEM} = 0.50 if temperature is higher than 43 °C, and R_{CEM} = 0.25 if it is lower than 43 °C. A monogram can be drawn (Fig. 4) in order to derive an equivalent time for the same effect at a different temperature. From this monogram, starting from known final heating time (t_f) and applied temperature (T), one can obtain time (t_{43}, also named CEM_{43}) required to achieve the equivalent damage if 43 °C would have been applied, as happens in Eq. (1) with R_{CEM} = 0.50 for T > 43 °C and R_{CEM} = 0.25 for T < 43 °C. Threshold values for t_{43} are available in literature depending on tissue

examined, and they have been obtained from experimental data referred to tissue injuries at 43 °C [25-27]. An example of t_{43} calculation is shown in Fig. 4. About 44.5 °C are continuously applied for 10 minutes, resulting in equivalently 80 minutes at 43 °C. This result can be roughly achieved with Eq. (3) with $t_2 = t_f$, T_1 = 43 °C and T_2 = 44.5 °C. Based on threshold values available for CEM_{43} from experiments [25-27], one can therefore establish if necrosis is achieved or not. Tissue temperature variations with time $T(t)$ can be introduced in the CEM_{43} criterion as follows:

$$CEM_{43} = t_{43} = \int_0^{t_f} R_{CEM}^{\left[43-T(t)\right]} dt \approx \sum_{t=0}^{t_f} R_{CEM}^{\left(43-\overline{T}_i\right)} \Delta t_i = t_f R_{CEM}^{\left(43-\overline{T}\right)} \tag{3}$$

In this equation, a summation approximation can be employed with sufficiently small Δt_i and average temperatures $\overline{T}_i$ evaluated for each Δt_i; if one assumes uniform temperature (or, if an average value is employed), then one could derive t_{43} in Eq. (3) without invoking any integral or summation, as for Eq. (1)

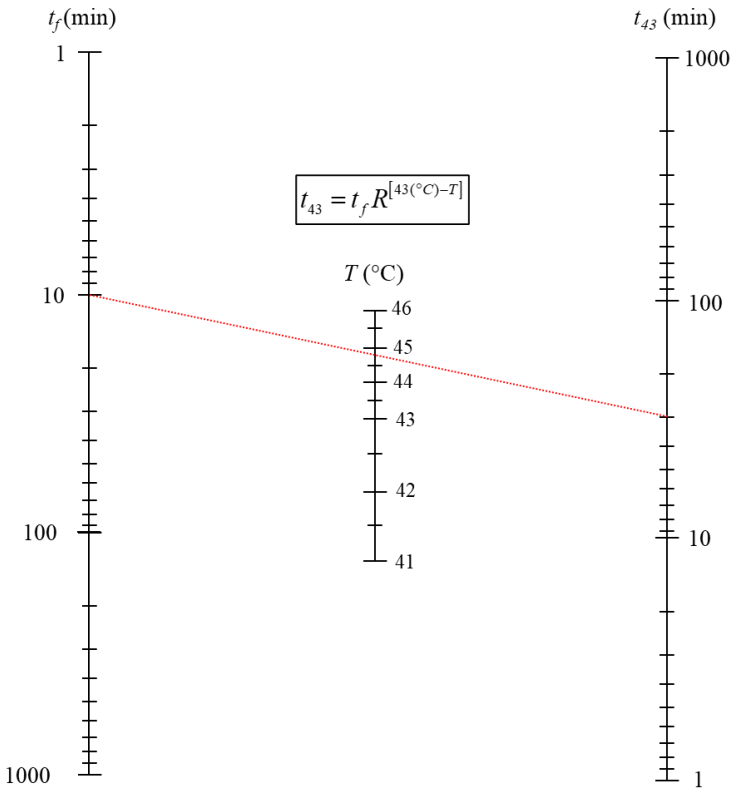

Figure 4. Monogram for t_{43} method prediction proposed by Sapareto and Dewey [23].

An alternative method to establish tissue damage is the Arrhenius damage integral criterion. With this criterion, damage is obtained from an exponential relationship between tissue exposure temperature, time, and parameters generally given by experimental studies on cells survivability. In particular, these parameters are available for many tissues, and they have been obtained fitting known exposure times and temperatures with cell surviving probabilities. However, it is noticed that the Arrhenius damage integral

criterion cannot be used a-priori since temperature evolution with time needs to be known. This approach is based on Arrhenius equation with a first-order kinetic reaction, reported in the following together with the thermal damage probability P_t that is between 0 and 1 [28].

$$\Omega_t(t) = \ln\left[\frac{c_{cell}(0)}{c_{cell}(t)}\right] = \int_0^t A e^{-\frac{\Delta H}{R_g T}} dt \tag{4a}$$

$$P_t = 1 - \mathrm{e}^{-\Omega_t(t)} \tag{4b}$$

In this expression, $\Omega_t(t)$ is the tissue injury degree, c_{cell} represents living cells concentration that depends on time, R_g is the universal gas constant, A is a kinetic energy frequency factor, and ΔH the irreversible damage reaction activation energy [25]. Parameters A and ΔH depend on tissue types, for example in liver they are A = 7.39 × 1039 1/s and ΔH = 2.577 × 105 J/mol [27], while for scald burns A = 3.1 × 1098 1/s and ΔH = 2.577 × 105 J/mol [29]. These two parameters A and ΔH can vary through a wide range of values, and they can be also temperature-depending. In particular, A could vary of several order of magnitudes, while ΔH remains of an order of magnitude of about 105 J/mol [30, 31]. Other values for the two parameters are available in Pearce [28]. From Eq. (4b), one can observe that for $\Omega_t(t)$ = 1 cell death probability is 63% (P_t = 0.63), while if $\Omega_t(t)$ = 4.6, then cell death probability becomes 99% (P_t = 0.99). This tissue injury value can therefore be assumed for completed necrosis achieved. Other two methods that can be used to quantify thermal dose, and then cells damage, are the Area Under the Curve criterion (AUC) [32] and the iso-temperature contours criterion [33]. With the AUC criterion, temperature minus baseline is integrated over time to establish thermal damage, while with the iso-temperature contours criterion one assumed that all the tissue over a prefixed temperature is necrotic. This threshold can vary between 43 °C [34, 35] and 59 °C [36], depending on many variables like tissues considered. Various papers compared distinct methods for thermal injury computation. Vallez et al. [37] suggested that CEM_{43} would be preferable for lower hyperthermia temperatures, while the Arrhenius thermal damage method is suggested for higher temperatures. An inverse-proportionality relationship between CEM_{43} and Arrehnius thermal damage criteria has been analyzed and discussed by Viglianti et al. [38]. Pearce [28] compared CEM_{43} and Arrhenius thermal damage criterions for laser-induced heating, concluding that the latter would be preferable since it allows to separately study various thermodynamically-independent processes. Mertyna et al. [32] generated different ablation measures by using radiofrequency ablation, microwave ablation and laser diffusing fibers, and they compared area under the curve, CEM_{43} and Arrhenius thermal damage criteria. The authors conclude that thermal dose should not be established based on temperature at the end of coagulation zone since this is not constant, but it depends on distance. Chang and Nguyen [27] simulated thermal and injury profiles for a radiofrequency ablation of 15 minutes, and comparisons between iso-temperature contours, CEM_{43} and Arrhenius damage criteria have been shown. They conclude that isothermal and CEM_{43} might cause significant errors in the estimation of lesion size.

2.

MODELLING HEAT TRANSFER IN TUMORS: STATE-OF-THE-ART

2. MODELLING HEAT TRANSFER IN TUMORS: STATE-OF-THE ART

Nowadays, thermal therapy is a very interesting topic in medicine, and many studies on the application of heat transfer to living tissues have been carried out in the last few decades, especially for cancer tumors treatment, from mild hyperthermia to high temperature thermal ablation, as described in the previous section. The challenge of predicting temperature in biological tissues becomes the focus of numerous researchers through the years, to improve treatment techniques and to develop new sophisticated and accurate devices. However, heat transfer in living systems is a complex topic because it entails a mixture of many mechanisms to consider, such as thermal conduction in tissues, convection and perfusion of blood, metabolic heat generation, vascular structure, changing of tissue properties depending on physiological condition and so on. Thus, studying the different heat transfer mechanisms has a key role, especially during different hyperthermia applications, as it is schematically described in Fig. 5.

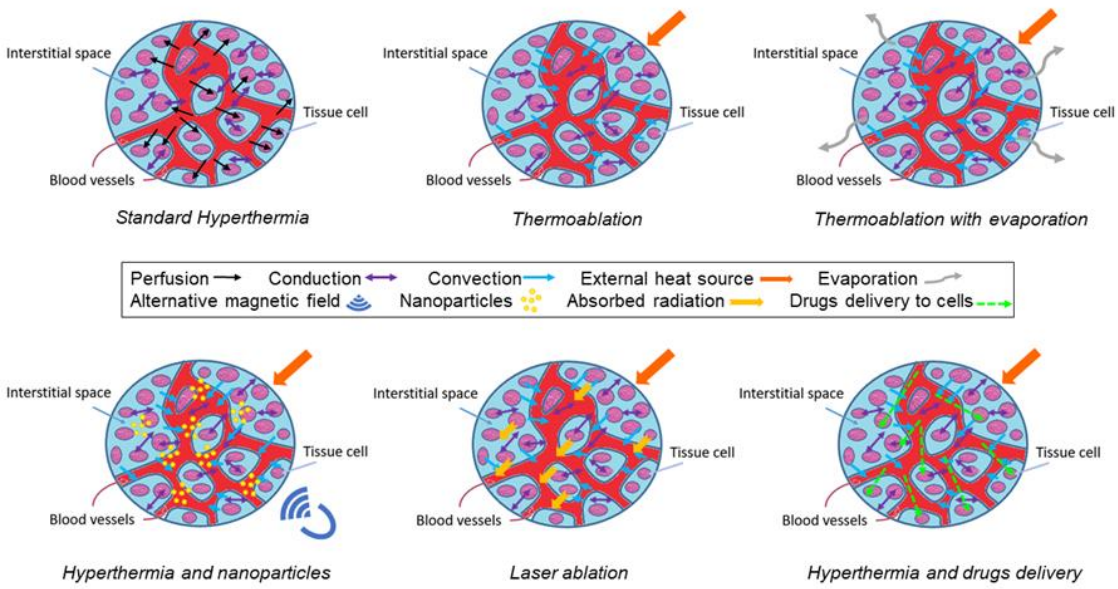

Figure 5. Heat transfer mechanisms involved in different hyperthermia applications.

In particular, modelling heat transfer in hyperthermia treatment of cancer has a key relevance in order to predict temperature profiles, because tumoral cells have to be destroyed completely, in order to avoid tumor recurrence, and at the same time the surrounding healthy tissue has to be preserved. In addition, the lack of experimentation in this field, due to ethical reasons, makes bioheat models even more significant. In this section, the attention is focused on hyperthermia treatment of cancer, showing how the models have been modified through the years when applied in specific applications.

2.1. Bioheat models applied in cancer treatment

Over the years, several mathematical models have been proposed since 1948, when Harry H. Pennes [39] introduced the “Pennes’ bioheat equation”, which describes the effect of blood perfusion and metabolic

heat generation rate on heat transfer within a living tissue. Based on an experimental analysis of human forearm, Pennes' model is written in its simplified form as:

$$\rho_t c_t \left(\frac{\partial T_t}{\partial t} \right) = \nabla \cdot \left(k_t \nabla T_t \right) + \rho_b c_b \omega_b \left(T_a - T_t \right) + Q_{met} \tag{5}$$

where t is the time and T is the temperature, subscripts t, b, a and met refer to tissue, blood, arterial blood, and metabolism, respectively, ρ is the density, c is the specific heat, k is the thermal conductivity, ω is the blood perfusion rate and Q_{met} is the heat generation due to metabolism. This model has been widely used by many researchers for numerous biological and medical applications, but it shows some shortcomings because of the various assumptions made by Pennes. In fact, it assumes uniform perfusion rate, so it does not consider blood flow direction, neglecting also important anatomical features of the circulatory network system such as the artery-vein countercurrent arrangement. Besides, Pennes' model considers only the venous blood stream as the one equilibrated with the tissue.

To overcome the shortcomings mentioned above, Wulff [40] introduced the convection heat transfer term and suggested that the blood flow contribution has to be modelled with a directional convection term in place of the scalar perfusion one. In the same year, Klinger [41] developed an analytical model like the one described Wulff [40]. He modelled a convection field based on *in vivo* vascular anatomy and he considered the spatial and temporal variations of the velocity and heat source. The limitation of Wulff [40] and Klinger [41] models is that tissue and blood volumes have to be in thermal equilibrium, which is not true everywhere.

Chen and Holmes [42] presented a model in which larger vessels are considered separately from smaller vessels and tissue, dividing the total tissue control volume into solid tissue and blood subvolumes, based on length scale analysis. The solid tissue subvolume includes scales that are not larger than one millimeter (tissues and smaller blood vessels), while the blood subvolume includes larger vessels. Furthermore, they classified blood vessels into thermally significant and insignificant vessels, showing that the major heat transfer process occurs for vessels with diameters between 50 and 500 μm. Even if Chen and Holmes [42] model represents a significant improvement of Pennes' equation, it is not easy to implement, because it needs detailed knowledge of the vascular network and blood perfusion.

Moreover, the model does not consider the effect of closely-spaced countercurrent artery-vein pairs. Weinbaum et al. [43, 44] introduced a new vascular three-layers bioheat model by considering the countercurrent blood flow and assuming that small arteries and veins are parallel, while flow direction is countercurrent. They derived three-equations model referred to heat transfer of the thermally significant artery and vein and the surrounding tissue, respectively.

Later Weinbaum and Jiji [45] proposed a simplified blood-tissue continuum model to overcome the complexity of the application of the initial model to practical situations, but also this model required more detailed anatomical data compared to others. More recently, thanks to some progress in the biological tissues measurement techniques, new models have been developed to obtain better results and improve

treatment procedures in biomedical applications such as hyperthermia therapy. Tzou [46, 47] proposed a dual phase-lag model, in which it is considered that Fourier's law of heat conduction gives erroneous results with non-homogenous inner structure as in the case of biological tissues. According to experimental results, they noted that there is non-Fourier heat conduction behaviour in living systems, resulting in a lag time between cause and effect in the propagation of a thermal disturbance imposed on the tissue.

Xuan and Roetzel [48] introduced a two-equation bioheat model in which the biological system is a porous media. It is divided into two different regions, namely, the vascular region and the extravascular region, without considering local thermal equilibrium between the two phases and introducing an equivalent effective thermal conductivity in the energy equations of blood and tissue. They proposed an interfacial convective heat transfer term instead of perfusion one.

Subsequently, Khaled and Vafai [49] and Khanafer and Vafai [50] remarked that the porous media theory is the most appropriate for the heat transfer treatment in biological tissues because of the fewer assumptions as compared to the other models.

Nakayama and Kuwahara [51] developed a generalized two-equation bioheat models for vascular and extravascular space in local thermal non-equilibrium condition, and they incorporated blood perfusion term within the two sub-volume equations. The two-equation model is extended to a three-equation model in order to consider the effect of heat transfer in closely spaced countercurrent artery-vein pair. The three equations are derived for arterial blood phase, venous blood phase and tissue phase distinctively with three different temperatures.

However, this model requires many detailed anatomical information, and its implementation is complex. In Table 1 the aforementioned bioheat models are resumed with their pros and cons in terms of accuracy and simplicity.

Table 1. Pros and cons of the most important bioheat models.

Bioheat model	Pros	Cons
Pennes' equation	✓ Very simple to apply	• Low accuracy
Two-equation bioheat model	✓ High accuracy	• More complex to implement
Local thermal equilibrium equation	✓ Less complex than two-equation model ✓ More accurate than Pennes' equation	• Lower accuracy than two-equation model
Three-energy equation model	✓ Very accurate	• It requires a lot of anatomical data difficult to find
Dual phase-lag model	✓ It allows to study the microstructure interactions with heat transport	• Difficulties in phase-lag times calculation

2.1.1. Pennes' bioheat model and its modifications

Even if it was the first, Pennes' [39] bioheat equation, Eq. (5), is still the mostly used model because of its simplicity and feasibility in hyperthermia treatment. From temperature distributions, Pennes' derived the model previously depicted in Eq. (5). He concluded that heat transfer generation is proportional to the temperature difference between tissue and arteries by means of the perfusion rate ω (s^{-1}) that is the quantity of blood perfused through the capillaries.

Pennes' bioheat equation has been modified several times through the years. Berjano [52] wrote a review on the specific topic about the state of the art of the theoretical modelling for radiofrequency ablation and in his work, the spatial distribution of temperature is always obtained by solving the Pennes' bioheat equation with some modifications. As regards the use of the Pennes' model for particular cases, first of all papers that combine the use of numerical simulation and experimental results have been described.

Yang et al. [53] proposed a modified form of the equation to predict tissue temperature during microwave ablation performed *ex vivo* in a bovine liver. During the experimentation, tissue temperature exceeds 100 °C, so in their model, evaporation has been considered with an extra term for energy needed to vaporize water, obtaining this modified equation:

$$\rho_t c_t \left(\frac{\partial T_t}{\partial t} \right) = \nabla \cdot \left(k_t \nabla T_t \right) + \rho_b c_b \omega_b \left(T_a - T_t \right) + Q_{met} + Q_{ext} - Q_E \tag{6}$$

where Q_{met} is the metabolic heat source, Q_{ext} is the microwave power density, obtained by solving the electromagnetic problem, and Q_E is the term that accounts for the energy needed to vaporize water. This last term is related to the change in water content of tissue as a function of time:

$$Q_E = -\gamma \frac{dW}{dt} \tag{7}$$

where γ is the water latent heat constant, that is equal to 2260 kJ kg^{-1}, and W is the tissue water density which is assumed to be only a function of temperature as follows:

$$W(T) = 778 \begin{cases} 1 - e^{\left(\frac{T-106}{3.42}\right)} & T \le 103°C \\ 0.037T^3 - 11.47T^2 + 1182T - 40582 & 103°C < T \le 104°C \\ e^{\left(\frac{T-80}{34.37}\right)} & T > 104°C \end{cases} \tag{8}$$

Comparing the simulation results to the experimental results, they concluded that the new method generates a more accurate prediction of tissue temperature than the original Pennes' bioheat equation.

Jaunich et al. [54] analysed the temperature distributions in skin tissue medium irradiated with a laser beam. Experimental validation is performed both on multi-layer tissue phantoms which simulate skin tissue and

having an embedded inhomogeneity simulating tumors and on freshly excised mouse skin tissue samples. The tissue temperature is calculated with Pennes' energy equation coupled with two different conduction models: the Fourier parabolic and non-Fourier hyperbolic heat conduction models. The starting Pennes' model becomes:

$$\rho_t c_t \frac{\partial T_t}{\partial t} = -\nabla \cdot q - \rho_b c_b \omega_b \left[T_t - T_a \right] - \nabla \cdot q_r \tag{9}$$

where q is the heat flux and q_r is the radiative heat flux. Radiative heat flux is expressed as:

$$\nabla \cdot q_r = \alpha \left(4n^2 \sigma_s T^4 - \int_{4\pi} \Phi I d\Omega \right) \tag{10}$$

where α is the absorption coefficient of tissue, n is the refractive index of tissue medium, σ_s is the Stephan-Boltzmann constant, Φ is the phase function, I is the scattered diffusive intensity and Ω is the solid angle. The first term on the right side of Eq. (9) is modeled by considering either Fourier or non-Fourier heat conduction approaches:

$$q = -k_t \nabla T_t \tag{11}$$

$$q + \tau \frac{\partial q}{\partial t} = -k_t \nabla T_t \tag{12}$$

where τ is the relaxation time of the medium. Numerical modelling results obtained from Fourier and non-Fourier heat conduction formulation are then compared with experimental measurements. The authors demonstrated that the hyperbolic heat conduction model is more accurate than the parabolic one, which underpredicts the peak temperature rise. They concluded that using the non-Fourier model is of prime importance for designing efficient technique of thermal treatment of tumors, because it considers the relaxation time of the tissue.

Cavagnaro et al. [55] investigated different numerical models of the dielectric and thermal property changes in temperature during *ex vivo* microwave thermal ablation.

Temperature distribution in the tissue is obtained solving the Pennes' equation written as:

$$\rho_t c_t \left(\frac{\partial T_t}{\partial t} \right) = \nabla \cdot \left(k_t \nabla T_t \right) + \rho_b c_b \omega_b \left(T_a - T_t \right) + Q_{met} + Q_{ext} \tag{13}$$

where the external source is expressed as:

$$Q_{ext} = \rho_t \mathrm{SAR} \tag{14}$$

where SAR is the Specific Absorption Rate computed by solving the Maxwell's equations, and it is calculated as:

$$\mathrm{SAR} = \frac{\sigma |\boldsymbol{E}|^2}{2\rho_t} \tag{15}$$

where σ is the effective electric conductivity and $|\mathbf{E}|^2 = E$ is the modulus of the electric field vector, obtained by means of Maxwell equations. Water vaporization based on Yang's study [53] is considered too, and the two models are modified with the temperature dependent properties. Models' outcomes with and without temperature dependent properties are finally compared with experimental data, showing that models not including the changes of the dielectric and thermal properties can be used only for very low values of the power radiated by the antenna, whereas a good agreement with the experimental values is obtained up to 20 W if water vaporization is included in the numerical model.

Shao et al. [56] proposed the employment of injected different nanoparticles to perform thermal ablation in cancer treatment of liver by means of radiofrequencies. In their work, governing equations of bioheat transfer are a modified form of the Pennes' model applied in two different regions as follows:

a) in the *living region*, tissue temperature equation is expressed as:

$$\rho_t c_t \left(\frac{\partial T_t}{\partial t} \right) = \nabla \cdot \left(k_t \nabla T_t \right) + \rho_b c_b \omega_b \left(T_a - T_t \right) + Q_{met} + Q_{ext} \tag{16}$$

where in this case Q_{ext} is the radiofrequency power density;

b) in the *damaged tissue region*, both perfusion and metabolic term are zero, so the equation becomes:

$$\rho_t c_t \left(\frac{\partial T_t}{\partial t} \right) = \nabla \cdot \left(k_t \nabla T_t \right) + Q_{ext} \tag{17}$$

Furthermore, they considered the blood perfusion variation depending on the degree of tissue/tumor damage:

$$\omega_b = \begin{cases} \omega_{b0} & \Omega(t) \le 0 \\ \omega_{b0}\left[1 + 25\Omega(t) - 260\Omega(t)^2\right] & 0 < \Omega(t) \le 0.1 \\ \omega_{b0} e^{-\Omega(t)} & \Omega(t) > 0.1 \end{cases} \tag{18}$$

where ω_{b0} is the constant blood perfusion of tissue/tumor and $\Omega(t)$ is tissue injury degree. Moreover, they

evaluated the temperature dependence of the thermal conductivity and specific heat, by means of these linear functions:

$$k(T)=\begin{cases} k_{T_{ref}}+0.0013\left(T-T_{ref}\right) & T\leq 100°\text{C} \\ k(100) & T>100°\text{C} \end{cases} \tag{19}$$

where k_{Tref} = 0.502 (W m^{-1} K^{-1}) and T_{ref} = 25 °C, and:

$$\text{c}(T)=\begin{cases} c_0 & T\leq 63.5°\text{C} \\ c_0+c_1\left(T-63.5\right) & T>63.5°\text{C} \end{cases} \tag{20}$$

where c_0 =3399.9 (J kg^{-1} K^{-1}) and c_1 =28.9 (J kg^{-1} K^{-2}).

Moreover, the thermal conductivity model for spherical nanoparticles used in this work is the Hamilton-Crosser (H-C) model [57], which predicts the thermal conductivity of nanofluids when they are injected to an intercellular space. The results of the models with and without nanoparticles injection have been validated thanks to an in-vitro experiment, and these outcomes revealed that incorporating thermally-enhancing nanoparticles promote heat transfer during radiofrequency ablation, obtaining an improved efficiency.

Guerrero Lopez et al. [58] used the Pennes' equation to calculate tissue temperature during a microwave ablation for breast cancer treatment, using the Eq. (13). For the experimental validation, the temperature measurement has been carried out both in *ex vivo* swine breast tissue and in a breast phantom with similar dielectric properties to those of human tissue. The same model has been applied in 2018 by Ortega-Palacios et al. [59] in vivo swine experimentation to test a novel 2.45 GHz double short distance slot coaxial antenna for cancer breast microwave ablation therapy. The goal of both the studies was to find the best antenna in microwave ablation, as regards the temperatures, instead, significant differences resulted comparing experimental and computational results, especially at higher input powers. These results show the inaccuracy of the simple Pennes' bioheat equation to predict temperature during hyperthermia treatment.

As regard the non-experimental works, Majchrzak et al. [60] used the Boundary Element Method (BEM) to solve the coupled problem, electromagnetic and thermal, connected with the biological tissue heating in a typical radiofrequency ablation treatment of tumor. Temperature field is described in the healthy and tumor regions distinctively by two Pennes' equations written in the form of Eq. (13) for both the different regions. This study shows the parameters of electromagnetic field allowing an optimal temperature distribution, considering that in the tumor region temperature has to be higher than 42 °C. The changes of electric field parameters cause the changes of temperature in the entire domain considered, but the choice of proper electric field parameters is difficult; in fact, both the distance between the tumor and the skin surface and its dimensions should be considered. Moreover, the method discussed can be applied when the tumor site and its dimensions are perfectly well known. In such a case, the methods of numerical simulation

are very effective tool.

Keangin et al. [61] developed a mathematical model to predict tissue temperature distribution in interstitial microwave ablation of liver cancer using a single slot antenna. They coupled electromagnetic wave equations, bioheat and mechanical deformation equations. As regards the transient bioheat equation, the Pennes' equation is written as in Eq. (13). Furthermore, liver tissue thermal conductivity and blood perfusion rate are considered linear functions of temperature as follows:

$$k_t(T) = 0.0012T + 0.4692 \tag{21}$$

$$\omega_b(T) = 0.000021T + 0.00035 \tag{22}$$

The same authors used the same model to analyse the heat transfer in liver tissue during microwave ablation using double slot antenna, [62] comparing the results obtained previously [61] and concluding that no clear difference between the two microwave coaxial antenna models has been shown due to low microwave power input from the microwave coaxial antenna during microwave ablation process (10 W). Furthermore, it has been found that the simulated results of model with deformation are corresponded closely with the experimental results by Yang et al. [53], whereas the results of model without deformation exhibited errors. Sheu et al. [63] proposed an acoustic-thermal-fluid coupled model for the purpose of predicting liver tumor temperature during a HIFU thermal ablation. As regards the energy equation for tissue heating, they divided the domain of interest into the region with tissue perfusion and the capillary region containing blood vessels. In the region without large blood vessels, the Pennes' bioheat equation has been employed:

$$\rho_t c_t \left(\frac{\partial T_t}{\partial t} \right) = \nabla \cdot \left(k_t \nabla T_t \right) - \rho_b c_b \omega_b \left(T_t - T_\infty \right) + Q_{ext} \tag{23}$$

where T_∞ is the temperature at a location far away from the heating focus and Q_{ext} is the ultrasound power deposition per unit volume, assumed to be proportional to the local acoustic intensity I_{ac} as follows:

$$Q_{ext} = 2\alpha I_{ac} \tag{24}$$

where α is the absorption coefficient expressed in (Np MHz^{-1} m^{-1}). In the region containing large vessels the equation employed in the model is:

$$\rho_t c_t \left(\frac{\partial T_t}{\partial t} \right) = \nabla \cdot \left(k_t \nabla T_t \right) - \rho_b c_b \mathbf{u}_b \cdot \nabla T_t + Q_{ext} \tag{25}$$

where $\mathbf{u}_b$ is the blood flow velocity. The authors show that HIFU frequency affects the heat deposition on

the tumor, in particular the higher the ultrasound frequency, the less amount of the heat is absorbed in the liver tumor and the smaller the focused region of the higher temperature.

Lopez Molina et al. [64] presented an analytical model to study radiofrequency ablation with needle-like internally cooled cylindrical electrode. The temperature distribution in the tissue is mathematically obtained by solving Pennes' bioheat Eq. (13) in cylindrical coordinates. The external source is the electrical power density expressed as:

$$Q_{ext} = \frac{j_0^2 r_0^2}{\sigma r^2} \tag{26}$$

where j_0 is the current density at the conductor surface, σ is the electrical conductivity, r_0 is the electrode radius and r the radial coordinate. Results showed that the maximal tissue temperature is reached ≈3 mm from the electrode, which confirms previous experimental findings. The authors also observed that the temperature distributions were similar for three coolant temperature values (5°C, 15°C and 25°C) and the differences were only notable in temperature very close to the probe.

Gupta et al. [65] developed a mathematical model describing the heat transfer in tissues during hyperthermia therapy. Their model might consider rectangular, cylindrical, or spherical coordinates. Body tissue is heated by electromagnetic radiation using a 432 MHz antenna. The boundary value problem is solved by Galerkin's method using the Bernstein. The bioheat equation solved under various coordinates and boundary conditions is a modified form of the Pennes' model and it can be written as:

$$\rho_t c_t \frac{\partial T_t(r,t)}{\partial t} = \frac{k_t}{r^\Gamma} \frac{\partial}{\partial r}\left(r^\Gamma \frac{\partial T_t(r,t)}{\partial r} \right) + \rho_b c_b \omega_b \left(T_a - T_t \right) + Q_{met} + Q_{ext} \tag{27}$$

where Γ is a coordinates index that is equal to 0, 1, 2 if references are made to rectangular, cylindrical, or spherical coordinates, respectively. The metabolic heat generation Q_{met} is expressed as a function of local tissue temperature as follows:

$$Q_{met} = 0.17 \times 2^{\frac{T-37}{10}} \tag{28}$$

The heat generation per unit volume of tissue due to electromagnetic radiation absorbed Q_{ext} is in the form:

$$Q_{ext} = \rho S P e^{a_c\left(\bar{r}-0.01\right)} \tag{29}$$

where S and a_c are the antenna constants, P is the transmitted power and $\bar{r}$ is the distance of tissue from outer surface.

An extension of the model has been proposed by Gupta et al. [66]. In their work, blood perfusion

dependence on temperature is considered as follows:

$$\rho_b\omega_b\left(T\right)=\begin{cases}\rho_b\omega_{b0} & T\le T_{cr}\\ \rho_b\omega_{b0}\left[1+\left(\dfrac{\omega_{b,\max}-\omega_{b0}}{\omega_{b0}}\right)\left(\dfrac{T-T_{cr}}{T_{\max}-T_{cr}}\right)\right] & T_{cr}<T<T_{\max}\\ \rho_b\omega_{b,\max} & T\ge T_{\max}\end{cases},\quad \begin{array}{l}T_{cr}=42.5°\text{C}\\ T_{\max}=45°\text{C}\\ \omega_{b,\max}/\omega_{b0}=25\end{array} \tag{30}$$

where $\omega_{b,max}$ is the maximum perfusion of the tissue and T_{cr} and T_{max} are fixed at 42.5 °C and 45 °C, respectively. For all simulations, they assume a ratio between $\omega_{b,max}$ and ω_{b0} equal to 25. The solution of the equations in both studies is in dimensionless form and authors obtained the time to achieve hyperthermia position in the target area based on probe shape, boundary conditions and internal heat source term. Furthermore, the effect of variation of temperature in target area between the two models has been investigated, concluding that total time for thermal therapy in tissues, when blood perfusion is temperature dependent, is less in comparison to the tissue in which blood perfusion is temperature independent.

Bermeo Varon et al. [67] employed numerical simulations to estimate state variables, like temperature distribution in tissues, during the ablation treatment of cancer induced by radiofrequency electromagnetic waves. They consider that the tumor is loaded with nanoparticles, and the Pennes' bioheat equation is as in Eq. (13). In this case, the external source depends on tissue, tumor, and nanoparticles properties, in particular, for the healthy tissue, which is assumed to be free of nanoparticles, it is written as in Eqs. (14) and (15); in the tumor, instead, the contribution due to the magnetic particles is added to the source term:

$$Q_{ext}=\frac{\sigma_t\left|\mathbf{E}\right|^2}{2}+\left(1-\theta\right)\frac{\sigma_{np}\left|\mathbf{E}\right|^2}{2}+\theta\left(\frac{9}{16}\frac{\chi''}{\mu_0\pi f R_{mil}^2}\left|\mathbf{E}\right|^2\right)+\mu_0\pi f\chi''\left|\mathbf{H}\right|^2 \tag{31}$$

where the subscript *np* refers to the tumor loaded with nanoparticles, $\theta=n_{np}\pi r_{np}^2/A_{tm}$ is the concentration of nanoparticles, that is, the total cross section of the nanoparticles divided by the area A_{tm} of the tumor, while r_{np} is the mean radius of the spherical nanoparticles and n_{np} is the number of nanoparticles, μ_0 is the dielectric vacuum permeability, f is the frequency, R_{mil} is the radius of magnetic induction loop, χ'' is the imaginary part of susceptibility of the magnetic nanoparticles and **H** is the magnetic field vector. The first term on the right side of Eq. (31) is referred to the heat dissipation in the healthy tissue, the second and the third terms refer to the heat generation in the tumor tissue with nanoparticles, while the fourth one is related to the magnetic field generated in the tumor embedded with nanoparticles. The model is solved with the Particle Filter, by means of Sampling Importance Resampling (SIR) algorithm. This study has been carried out for a 2-D domain, and the same authors developed the same model in a 3-D domain [68] finding in both cases excellent agreement between estimated and exact temperatures.

Reis et al. [69] used a 3-D nonlinear Pennes' bioheat equation with a temperature-dependent blood perfusion to model numerically the hyperthermia treatments by magnetic nanoparticles. The tissue has been modelled by considering skin, fat, and muscle layers in addition to the tumor, together with their

temperature dependence. In this study, the bioheat equation is in the form of Eq. (13) and the external heat source is the heat generated by the interaction between nanoparticles and the magnetic field, defined as:

$$Q_{ext} = \sum_{i=1}^{n_{inj}} Q_{max,i} e^{-\frac{r_{inj,i}^2}{r_{dist,i}^2}} \tag{32}$$

where r_{inj} is the radial distance of the injection site, r_{dist} is the distance covered by the heat generated by the nanoparticles, Q_{max} is the maximum power density and n_{inj} is the total number of injection points. The temperature dependent blood perfusion of fat, muscle and tumor is given, respectively, by the following functions:

$$\omega_{muscle} = \begin{cases} 0.45 + 3.55 e^{\left[-\frac{(T-45)^2}{12}\right]} & T \le 45°C \\ 4 & T > 45°C \end{cases} \tag{33}$$

$$\omega_{fat} = \begin{cases} 0.36 + 0.36 e^{\left[-\frac{(T-45)^2}{12}\right]} & T \le 45°C \\ 0.72 & T > 45°C \end{cases} \tag{34}$$

$$\omega_{tm} = \begin{cases} 0.833 & T < 37°C \\ 0.833 - 5.438 \cdot 10^{-3} (T-37)^{4.8} & 37°C \le T \le 42°C \\ 0.416 & T > 42°C \end{cases} \tag{35}$$

To solve the equations, the Finite-Difference Method (FDM) has been employed and the resulting system of nonlinear equations is then solved by a predictor-multicorrector algorithm. As regards temperature profiles, the simulation revealed that a temperature-dependent blood perfusion rate has a great influence in the results when compared to the linear model for the transient solution.

Lopez Molina et al. [70] developed an analytical solution for the temperature distribution in a radiofrequency ablation process with internally cooled needle-like electrodes when the biological tissue is not perfused. Due to cylindrical geometry of the theoretical model, the equation used is:

$$\rho_t c_t \frac{\partial T_t(r,t)}{\partial t} = k_t \left(\frac{\partial^2 T_t(r,t)}{\partial r^2} + \frac{1}{r} \frac{\partial T_t(r,t)}{\partial r} \right) + Q_{ext}(r,t) \tag{36}$$

The external source is the electrical power density expressed as in Eq. (26). They concluded that the temperature value is finite both when the spatial domain is finite and when time is finite for any spatial

domain.

In Table 2 Pennes' bioheat equation modifications depending on the physics are resumed.

Table 2. Pennes' bioheat equation modifications depending on the physics.

Pennes' bioheat equation [39]		
	$\rho_t c_t \left(\frac{\partial T_t}{\partial t}\right) = \nabla \cdot \left(k_t \nabla T_t\right) + \rho_b c_b \omega_b \left(T_a - T_t\right) + Q_{met} + Q_{ext} - Q_E$ (6)	
Source	**Term**	**Case**
Yang et al. [53]	$Q_E = -\gamma \frac{dW}{dt}$ (7) $W(T) = 778 \begin{cases} 1 - e^{\left(\frac{T-106}{3.42}\right)} & T \le 103°C \\ 0.037T^3 - 11.47T^2 + 1182T - 40582 & 103°C < T \le 104°C \\ e^{\left(\frac{T-80}{34.37}\right)} & T > 104°C \end{cases}$ (8)	MW ablation with water evaporation
Jaunich et al. [54]	$Q_{ext} = -\nabla \cdot q_r = -\alpha \left(4n^2 \sigma_s T^4 - \int_{4\pi} \Phi I d\Omega\right)$ (10)	Laser beam for skin tissue
Cavagnaro et al. [55]	$Q_{ext} = \frac{\sigma \lvert \mathbf{E} \rvert^2}{2}$ (14, 15)	MW thermal ablation
Shao et al. [56]	Living region $\omega_b = \begin{cases} \omega_{b0} & \Omega(t) \le 0 \\ \omega_{b0}\left[1 + 25\Omega(t) - 260\Omega(t)^2\right] & 0 < \Omega(t) \le 0.1 \\ \omega_{b0} e^{-\Omega(t)} & \Omega(t) > 0.1 \end{cases}$ (18)	RF ablation with nanoparticles
	Damaged region $\omega_b = 0$	
	Both regions $k(T) = \begin{cases} k_{T_{ref}} + 0.0013\left(T - T_{ref}\right) & T \le 100°\text{C} \\ k(100) & T > 100°\text{C} \end{cases}$ (19) $c(T) = \begin{cases} c_0 & T \le 63.5°\text{C} \\ c_0 + c_1\left(T - 63.5\right) & T > 63.5°\text{C} \end{cases}$ (20)	
Keangin et al. [61]	$Q_{ext} = \frac{\sigma \lvert \mathbf{E} \rvert^2}{2}$ (14, 15) $k_t(T) = 0.0012T + 0.4692$ (21) $\omega_b(T) = 0.000021T + 0.00035$ (22)	Liver thermal ablation
Sheu et al. [63]	$Q_{ext} = 2\alpha I_{ac}$ (24)	HIFU thermal ablation
Gupta et al. [65]	$Q_{met} = 0.17 \times 2^{\frac{T-37}{10}}$ (28) $Q_{ext} = \rho S P e^{a_c\left(\bar{r} - 0.01\right)}$ (29)	RF ablation

Gupta et al. [66]	$\rho_b\omega_b(T)=\begin{cases}\rho_b\omega_{b0} & T\le T_{cr}\\ \rho_b\omega_{b0}\left[1+\left(\frac{\omega_{b,\max}-\omega_{b0}}{\omega_{b0}}\right)\left(\frac{T-T_{cr}}{T_{\max}-T_{cr}}\right)\right] & T_{cr}<T<T_{\max}\\ \rho_b\omega_{b,\max} & T\ge T_{\max}\end{cases}$, T_{cr}=42.5°C, $T_{\max}$=45°C, $\omega_{b,\max}/\omega_{b0}$=25 (30)	RF ablation
Bermeo Varon et al. [67]	$Q_{ext}=\frac{\sigma_t\lvert\mathbf{E}\rvert^2}{2}+(1-\theta)\frac{\sigma_{np}\lvert\mathbf{E}\rvert^2}{2}+\theta\left(\frac{9}{16}\frac{\chi''}{\mu_0\pi f R_{mil}^2}\lvert\mathbf{E}\rvert^2\right)+\mu_0\pi f\chi''\lvert\mathbf{H}\rvert^2$ (31)	RF ablation
Reis et al. [69]	$Q_{ext}=\sum_{i=1}^{n_{inj}}A_i e^{-\frac{r_{inj,i}^2}{r_{dist,i}^2}}$ (32) $\omega_{muscle}=\begin{cases}0.45+3.55e^{\left[-\frac{(T-45)^2}{12}\right]} & T\le 45°C\\ 4 & T>45°C\end{cases}$ (33) $\omega_{fat}=\begin{cases}0.36+0.36e^{\left[-\frac{(T-45)^2}{12}\right]} & T\le 45°C\\ 0.72 & T>45°C\end{cases}$ (34) $\omega_{tm}=\begin{cases}0.833 & T<37°C\\ 0.833-5.438\cdot10^{-3}(T-37)^{4.8} & 37°C\le T\le 42°C\\ 0.416 & T>42°C\end{cases}$ (35)	Magnetic nanoparticles hyperthermia

2.1.2. Local Thermal Equilibrium and Local Thermal Non-Equilibrium Equations (LTE and LTNE)

In both Local Thermal Equilibrium (LTE) and Local Thermal Non-Equilibrium (LTNE) formulations, it is assumed that the whole volume control is a porous medium [71]. Three anatomical compartments are identified in the porous biological tissues, namely, blood vessels, cells and interstitium, as illustrated in Fig. 6. The interstitial space is further divided into the extracellular matrix and the interstitial fluid. However, for sake of simplicity, the biological tissue is divided into two distinctive regions, namely, the extra-vascular region and the vascular region.

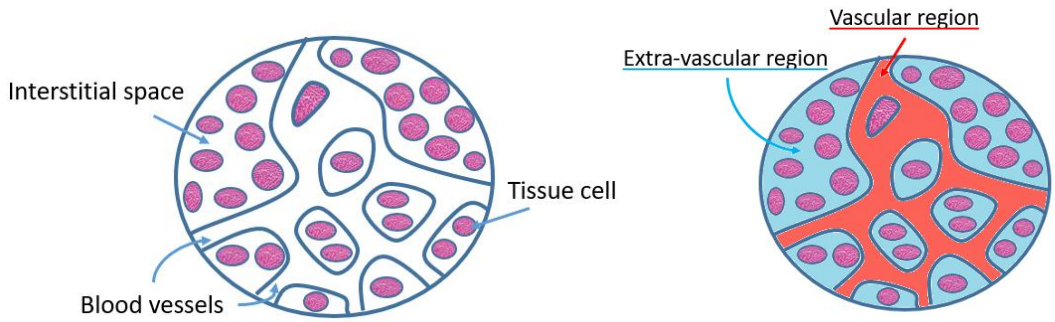

Figure 6. Anatomical scheme of a biological porous medium.

In the LTE formulation, the phases are in local thermal equilibrium, thus only one equation is needed for the energy; in the LTNE formulation, two phases with different temperatures have to be characterized with their own energy equation. The LTNE model has been proposed for biological systems by Xuan and Roetzel [48]. Governing equations are:

tissue phase:

$$(1-\varepsilon)\rho_t c_t \frac{\partial \langle T_t \rangle}{\partial t} = (1-\varepsilon) k_t \nabla^2 \langle T_t \rangle + ha\left(\langle T_b \rangle - \langle T_t \rangle\right) + (1-\varepsilon) Q_t \tag{37}$$

blood phase:

$$\varepsilon \rho_b c_b \left(\frac{\partial \langle T_b \rangle}{\partial t} + \mathbf{u}_b \cdot \nabla \langle T_b \rangle \right) = \varepsilon k_b \nabla^2 \langle T_b \rangle + ha\left(\langle T_t \rangle - \langle T_b \rangle\right) + \varepsilon Q_b \tag{38}$$

where the volume averaging technique is employed to consider the volume average quantities of the variables [17], so the symbol <> refers to the volume averaged quantity of a generic variable and will be neglected for the sake of simplicity. So, T_t and T_b are temperatures averaged over the tissue and blood volumes, ε is the porosity, i.e., the volume filled by the blood compared to the total volume, h is the heat transfer coefficient, $\mathbf{u}_b$ is the blood velocity, a is the volumetric transfer area between tissue and blood, and Q is the absorbed power density.

The same approach has been used by Yuan [72] to analyze the tumor tissue temperature during thermal ablation therapy, under thermal non-equilibrium conditions. In his work, comparisons between results from

LTNE and LTE models have been also reported to show when it is necessary to employ one of these two models. When the Local Thermal Equilibrium hypothesis is maintained, the tissue temperature is equal to blood temperature (T_t=T_b=T), thus Eqs. (37) and (38) can be combined into a single equation:

$$\left[\left(1-\varepsilon\right)\rho_t c_t + \varepsilon\rho_b c_b\right]\frac{\partial T}{\partial t} + \varepsilon\rho_b c_b \mathbf{u}_b \cdot \nabla T = \left[\left(1-\varepsilon\right)k_t + \varepsilon k_b\right]\nabla^2 T + \left(1-\varepsilon\right)Q_t + \varepsilon Q_b \tag{39}$$

Yuan concluded that the one-equation porous model is suitable for a distribution of blood vessels when the diameters are less than 30 μm and the blood velocities are lower than 0.4 cm s^{-1}.

Mahjoob and Vafai [73] analytically investigated heat transfer in tissues during hyperthermia treatment, utilizing LTNE model in porous media and finally finding exact solutions for blood and tissue phase temperature profiles as well as overall heat exchange correlations are established for the first time, for two primary tissue/organ models representing isolated and uniform temperature conditions. The two equations are written for the tissue phase and blood phase respectively as:

$$\left(1-\varepsilon\right)k_t \nabla^2 T_t + ha\left(T_b - T_t\right) + \left(1-\varepsilon\right)Q_{met} = 0 \tag{40}$$

$$\varepsilon\rho_b C_b \mathbf{u}_b \cdot \nabla T_b = (\varepsilon k_b + k_{b,dis})\nabla^2 T_b - ha\left(T_b - T_t\right) \tag{41}$$

where the metabolic heat Q_{met} is considered as heat source for the solid phase. It is important to underline that velocity is set to be uniform through the domain as explained also in [74]. Results indicate the importance of utilizing the local thermal non-equilibrium model especially at higher metabolic heat generation and within biological media with lower vascular volume fraction. In fact, a decrease in the metabolic heat generation or an increase in the organ/tissue's vascular volume fraction enhances temperature uniformity within the media resulting in a more effective hyperthermia treatment. Mahjoob and Vafai [75] extended the analytical solution of the previous work [73] for bioheat transfer for double layer biological media, performing the analysis for the same primary tissue/organ models, namely, isolated core region and uniform core temperature conditions. The same analysis has been also applied for consecutive variable cross-sectional biological media [76].

Dombrovsky et al. [77] developed a combined thermal model for transient temperature field during laser heating of embedded gold nanoparticles. They coupled a modified two-flux approximation model for the radiative heat transfer and a local thermal equilibrium equation for the temperature field. The LTE equation is:

$$\rho_t c_t \frac{\partial T}{\partial t} - \varepsilon \rho_b c_b \mathbf{u}_b \nabla T = \nabla \cdot \left(k \nabla T \right) + \left(1 - \varepsilon \right) Q_{met} + Q_{ext} \tag{42}$$

where Q_{ext} represents the heat generation due to absorption of laser radiation by gold nanoshells, expressed in this form:

$$Q_{ext} = \alpha \frac{\left(1 - \mu_{cr} \right) g + F}{1 - \omega_{tr} \mu_{cr}} \tag{43}$$

with α the absorption coefficient, ω_{tr} the nanoshell transport albedo, μ_{cr} the critical cosine of the angle, g, and F two functions that depend on the radiative heat transfer.

Dombrovsky et al. [78] improved the model presented in [77], basing it on two-dimensional axisymmetric models for both radiative transfer and heat transfer, and proposed a more detailed model for heat transfer in human tissues, especially for the radiative heat transfer part.

For tissue phase:

$$\left(1 - \varepsilon \right) \rho_t c_t \frac{\partial T_t}{\partial t} = \left(1 - \varepsilon \right) k_t \nabla^2 T_t + ha \left(T_b - T_t \right) + \left(1 - \varepsilon \right) Q_{met} + \left(1 - \varepsilon \frac{\alpha_b}{\alpha} \right) Q_{ext,laser} + Q_{ch} \tag{44}$$

For blood phase:

$$\varepsilon \rho_b c_b \left(\frac{\partial T_b}{\partial t} + \mathbf{u}_b \cdot \nabla T_b \right) = \varepsilon k_b \nabla^2 T_b - ha \left(T_b - T_t \right) + \varepsilon \frac{\alpha_b}{\alpha} Q_{ext,laser} \tag{45}$$

where α_b is the spectral absorption coefficient of arterial blood, α is the total absorption coefficient and the

term Q_{ch} considers the heat of endothermic chemical conversions in human tissues and venous blood during a strong hyperthermia, described as:

$$Q_{ch} = \left(1-\varepsilon_a-\varepsilon_v\right)L_t\frac{\partial\rho_t}{\partial t}+\varepsilon_v L_v\frac{\partial\rho_v}{\partial t} \tag{46}$$

In this equation, ε_v and ε_a are the volume fractions of venous and arterial blood respectively and L_v and L_t are the specific thermal effects of chemical conversions in venous blood and tissue, respectively. The authors concluded that the required uniform heating of the tumor can be achieved for some superficial tumors even without gold nanoshells or other invasive procedures.

Keangin and Rattanadecho [79] analysed the temperature distribution model to calculate tissue temperature during microwave ablation in two-layered porous liver by single and double microwave coaxial antenna. They proposed a mathematical model using transient momentum equations and energy equation coupled with electromagnetic wave propagation equation described by Maxwell equations. The governing equation describing the heat transfer is the Local Thermal Equilibrium model written as:

$$\left[\left(1-\varepsilon\right)\rho_t c_t+\varepsilon\rho_b c_b\right]\frac{\partial T}{\partial t}+\varepsilon\rho_b c_b\mathbf{u}_b\cdot\nabla T=\left[\left(1-\varepsilon\right)k_t+\varepsilon k_b\right]\nabla^2 T+Q_{met}+Q_{ext} \tag{47}$$

In this case, the external heat source is equal to the resistive heat generated by the electromagnetic field expressed as in Eqs. (14) and (15). The influences of four blood velocities (0.4 (cm s^{-1}), 2 (cm s^{-1}), 3 (cm s^{-1}) and 3.4 (cm s^{-1})), three porosities (0.025, 0.05 and 0.1), four input microwave powers (5, 10, 15 and 20 W) and three positions within the porous liver (distance from a Microwave Coaxial Antenna (MCA)) on the tissue and blood temperature distributions have been investigated. Comparing the results with previous experimental works, the authors concluded that the LTE assumption can be used when the blood velocities are 0.4 (cm s^{-1}) and 2 (cm s^{-1}) in all porosities, whilst, in case of blood velocities to be 3 (cm s^{-1}) and 3.4 (cm s^{-1}) the LTNE assumption for heat transfer analysis needs to be utilized. Moreover, the LTE model is suitable for predicting a distribution of temperature in the case of high porosity for this model.

In the same year, Keangin and Rattanadecho [80] proposed a LTNE model to calculate blood and tissue

temperatures distributions in a porous liver during microwave ablation by single slot MCA. The energy governing equations have been represented as:

Tissue phase:

$$\left(1-\varepsilon\right)\rho_t c_t \frac{\partial T_t}{\partial t} = \left(1-\varepsilon\right)k_t \nabla^2 T_t + ha\left(T_b - T_t\right) + \rho_t c_t \omega_b \left(T_b - T_t\right) + \left(1-\varepsilon\right)Q_{met} + \left(1-\varepsilon\right)Q_{ext,t} \tag{48}$$

Blood phase:

$$\varepsilon \rho_b c_b \left(\frac{\partial T_b}{\partial t} + \mathbf{u}_b \cdot \nabla T_b \right) = \varepsilon k_b \nabla^2 T_b + ha\left(T_t - T_b\right) \tag{49}$$

The blood perfusion term is added in both tissue and blood phases, accounting for the heat transfer associated with the transcapillary fluid exchange via arterial-venous anastomoses. As before, external heat source is expressed with Eqs. (14) and (15). The study aims to understand the influence of antenna type on the SAR profile, temperature profile and blood velocity profile. It is shown that the highest values of SAR, blood velocity and temperature are achieved through the liver if a single slot MCA is employed instead of a double slot antenna.

Wang et al. [81] used the LTNE model to describe the temperature distribution in annular living tissues subject to radiofrequency ablation. They also considered dispersion thermal conductivity in their model. The governing equations for both tissue and blood phases are expressed in cylindrical coordinates and then solved analytically.

For the tissue phase:

$$\left(1-\varepsilon\right)k_t \frac{1}{r}\frac{\partial}{\partial r}\left(r \frac{\partial T_t}{\partial r} \right) - ha\left(T_t - T_b\right) + \left(1-\varepsilon\right)Q_{met} = 0 \tag{50}$$

For the blood phase:

$$\varepsilon\rho_b c_b w\frac{\partial T_b}{\partial z}=\left(\varepsilon k_b+k_{b,dis}\right)\frac{1}{r}\frac{\partial}{\partial r}\left(r\frac{\partial T_b}{\partial r}\right)+ha\left(T_t-T_b\right) \tag{51}$$

where r is the radial coordinate, w the axial velocity component and $k_{b,dis}$ is the blood dispersion conductivity. The effects of physiological parameters such as metabolic heat generation, volume fraction of the vascular space, ratio of the effective blood to tissue conductivities, on the blood and tissue temperature distributions were analysed. From the results, the authors conclude that an increase in the metabolic heat generation or in the vascular volume fraction enhances the temperatures for the blood and tissue phases.

Vyas et al. [82] modelled the transient variation of temperature distributions inside irradiated biological tissue phantoms, in photo thermal therapy (RTE). The authors coupled the LTNE with the radiative source term, defined by the RTE.

For the solid matrix:

$$\left(1-\varepsilon\right)\rho_t c_t\frac{\partial T_t}{\partial t}=\left(1-\varepsilon\right)k_t\nabla^2 T_t+ha\left(T_b-T_t\right)+\left(1-\varepsilon\right)Q_{ext} \tag{52}$$

For the fluid matrix:

$$\varepsilon\rho_b c_b\left(\frac{\partial T_b}{\partial t}+\mathbf{u}_b\cdot\nabla T_b\right)=\varepsilon k_b\nabla^2 T_b+ha\left(T_t-T_b\right)+\varepsilon Q_{ext} \tag{53}$$

where the volumetric source term Q_{ext} is determined by calculating the divergence of the radiative heat flux:

$$Q_{ext}=\nabla\cdot q_r=\alpha\left(4\sigma_s T^4-G\right) \tag{54}$$

In this equation, α is the absorption coefficient and G the incident intensity. Results of the comparative study between LTNE and LTE models of heat transfer were presented. It was observed that even though LTNE model resulted in lesser values of temperature rise, it predicted the presence of significant thermal

gradients between the solid and fluid matrices of the porous tissue region. Furthermore, the temperature distribution inside tissue phantoms embedded with a single blood vessel and counter current artery vein blood vessels was studied. It was observed that the single blood vessel model resulted in higher temperature rise at the location of the inhomogeneity as compared to the counter current model. In addition, the effect of the blood vessel diameter on the temperature distributions was studied to determine the critical limit of the diameter value below which the blood vessels become thermally insignificant, concluding that blood vessels of diameter lesser than 1 mm have minimal effect on the resultant temperature distributions. In Table 3, LTNE equations modifications depending on the physics are resumed.

Table 3. LTNE equations modifications depending on the physics.

Local Thermal Non-Equilibrium (Xuan and Roetzel [48])		
Tissue $$(1-\varepsilon)\rho_t c_t \frac{\partial\langle T_t\rangle}{\partial t} = (1-\varepsilon)k_t\nabla^2\langle T_t\rangle + ha\left(\langle T_b\rangle - \langle T_t\rangle\right) + (1-\varepsilon)Q_t \quad (37)$$ Blood $$\varepsilon\rho_b c_b\left(\frac{\partial\langle T_b\rangle}{\partial t} + \mathbf{u}_b\cdot\nabla\langle T_b\rangle\right) = \varepsilon k_b\nabla^2\langle T_b\rangle + ha\left(\langle T_t\rangle - \langle T_b\rangle\right) + \varepsilon Q_b \quad (38)$$		
Source	**Term**	**Case**
Yuan [72]	$T_t = T_b = T$, $Q_{ext} = 0$ (39)	Hyperthermia treatment
Mahjoob and Vafai [73]	$Q_t = Q_{met}$, $Q_{ext} = 0$, $Q_b = 0$ (40,41) $\varepsilon k_b = \varepsilon k_b + k_{b,dis}$ (41) (entering boundary heat flux)	Hyperthermia treatment
Dombrovsky et al. [77]	$T_t = T_b = T$, $Q_t = Q_{met}$, $Q_b = 0$ (42) $Q_{ext} = \alpha\frac{(1-\mu_{cr})g + F}{1-\omega_{tr}\mu_{cr}}$ (43)	Laser heating of embedded gold nanoparticles
Dombrovsky et al. [78]	Tissue $Q_{ext} = \left(1-\varepsilon\frac{\alpha_b}{\alpha}\right)Q_{ext,laser} + (1-\varepsilon_a-\varepsilon_v)L_t\frac{\partial\rho_t}{\partial t} + \varepsilon_v L_v\frac{\partial\rho_v}{\partial t}$ (44,46) Blood $Q_b = \varepsilon\frac{\alpha_b}{\alpha}Q_{ext,laser}$ (45)	Laser heating of embedded gold nanoparticles
Keangin and Rattanadecho [80]	$Q_t = Q_{met}$, $Q_b = 0$ $Q_{ext} = (1-\varepsilon)Q_{ext,t} + \rho_t c_t\omega_b(T_b - T_t)$ (48)	MCA ablation
Wang et al. [81]	$Q_t = Q_{met}$, $Q_{ext} = 0$, $Q_b = 0$ (50,51) $\varepsilon k_b = \varepsilon k_b + k_{b,dis}$ (52) (radial coordinates model)	RFA
Vyas et al. [82]	$Q_{ext} = \nabla\cdot q_r = \alpha\left(4\sigma_s T^4 - G\right)$ (54)	Photo thermal therapy

2.1.3. Dual-phase-Lag bioheat model (DPL)

Recently, the Dual-Phase-Lag (DPL) bioheat model has been developed since Fourier's law of heat conduction gives erroneous results with non-homogenous inner structure as in the case of biological tissues. Indeed, there is a lag time between cause and effect in the propagation of a thermal disturbance imposed on the tissue.

Liu and Chen [83] applied this model to study tissue temperature profiles during magnetic hyperthermia treatment of a spherical liver tumor. The heat transport equations in the tumor with radius R and the surrounding healthy tissue are written in spherical coordinates as follows.

For the tumor region ($0 \leq r \leq R$):

$$k_{tm}\frac{1}{r^2}\frac{\partial}{\partial r}\left[r^2\left(\frac{\partial T_{tm}}{\partial r}+\tau_{T,tm}\frac{\partial^2 T_{tm}}{\partial t\partial r}\right)\right]=\left(1+\tau_{q,tm}\frac{\partial}{\partial t}\right)\left[\rho_{tm}c_{tm}\frac{\partial T_{tm}}{\partial r}-\rho_b c_b\omega_{b,tm}\left(T_b-T_t\right)-Q_{met,tm}\right] \tag{55}$$

For the healthy tissue ($R \leq r \leq \infty$):

$$k_t\frac{1}{r^2}\frac{\partial}{\partial r}\left[r^2\left(\frac{\partial T_t}{\partial r}+\tau_{T,t}\frac{\partial^2 T_t}{\partial t\partial r}\right)\right]=\left(1+\tau_{q,t}\frac{\partial}{\partial t}\right)\left[\rho_t c_t\frac{\partial T_t}{\partial r}-\rho_b c_b\omega_{b,t}\left(T_b-T_t\right)-Q_{met,t}-Qu_q\left(t\right)\right] \tag{56}$$

where τ_q is the phase-lag of the heat flux, τ_T is the phase-lag of the temperature gradient, Q is the power density and $u_q(t)$ is a step function that modulates heat transfer. Results show that the behavior of non-Fourier bioheat transfer is concerned with the lag times only at the early stages of heating. The lag time τ_T reflects the micro-structural interaction effect in the media, so the micro-structural interaction effect can significantly affect the transient behavior of bio-heat transfer in living tissues.

Kumar and Rai [84] investigated the thermal behaviour in living tissues during thermal therapy, using time fractional dual-phase-lag bioheat model. A piece of skin tissue of length l is heated by electromagnetic radiation using a 432 MHz antenna. The DPL model is written in this form:

$$\left(1+\frac{\tau_q^\alpha}{\Gamma_f\left(\alpha+1\right)}\frac{\partial^\alpha}{\partial t^\alpha}\right)\left[\rho_t c_t\frac{\partial T_t}{\partial r}-Q_{met}-\rho_b c_b\omega_b\left(T_b-T_t\right)-Q_{ext}\right]=k_t\left(1+\frac{\tau_T^\alpha}{\Gamma_f\left(\alpha+1\right)}\frac{\partial^\alpha}{\partial t^\alpha}\right)\frac{\partial^2 T_t}{\partial r^2} \tag{57}$$

where $\partial^\alpha/\partial t^\alpha$ is the fractional order Caputo derivative of arbitrary order α, Q_{met} is the metabolic heat generation source taken as a function of local tissue temperature in the form:

$$Q_{met}=Q_{met,ref}\times\left[1+\left(\frac{T-T_0}{10}\right)\right] \tag{58}$$

with $Q_{met,ref}$ the reference metabolism and T_0 is the initial temperature. The electromagnetic radiation heat

source is described as:

$$Q_{ext} = \rho S P e^{a_c\left(\bar{r}-r_p\right)} \tag{59}$$

where S and a_c are the antenna constants, P is the transmitted power, $\bar{r}$ is the distance of tissue from outer surface and r_p is the probe position. The bioheat model is then solved by means of finite element Legendre wavelet Galerkin method. Results obtained from proposed numerical scheme are approximately the same of the results obtained from exact solution in a specific case. In addition, temperature distribution in tissue increases as the values of time fractional order derivative increases with respect to space, so, the authors conclude that the success of thermal therapy in the treatment of metastatic cancerous cell depends on time fractional order derivative to precise prediction and control of temperature.

2.1.4. Other bioheat models

Other models have been proposed through the years, and they cannot be classified exactly as in the previous paragraphs since they refer to particular cases.

Khanafer et al. [85] modelled both a single blood vessel and tumor tissue, to investigate the influence of pulsatile laminar flow and hyperthermia heating protocol on temperature profiles. The tumor tissue is modelled using the volume-averaged porous media equations. Thus, the heat transfer equations using cylindrical polar coordinates are:

Artery lumen:

$$\frac{\partial T_b}{\partial t} + u\frac{\partial T_b}{\partial r} + w\frac{\partial T_b}{\partial z} = \alpha_{diff,b}\left[\frac{1}{r}\frac{\partial}{\partial r}\left(\frac{\partial T_b}{\partial r}\right) + \frac{\partial^2 T_b}{\partial z^2}\right] \tag{60}$$

where u and w are the radial and axial velocities and $\alpha_{diff,b}$ the blood thermal diffusivity.

For the artery wall, a volume-averaged form is employed:

$$\frac{\partial T_t}{\partial t} + u\frac{\partial T_t}{\partial r} + w\frac{\partial T_t}{\partial z} = \alpha_{diff,e}\left[\frac{1}{r}\frac{\partial}{\partial r}\left(\frac{\partial T_t}{\partial r}\right) + \frac{\partial^2 T_t}{\partial z^2}\right] \tag{61}$$

where $\alpha_{diff,e}$ is the effective thermal diffusivity, which includes effective thermal properties for thermal conductivity, density, and heat capacity, related to blood and tissue properties:

$$\rho_e c_e = \varepsilon \rho_b c_b + \left(1-\varepsilon\right)\rho_t c_t \tag{62}$$

$$k_e = \varepsilon k_b + \left(1-\varepsilon\right)k_t \tag{63}$$

where ε is the porosity, the subscript t refers to solid matrix properties (i.e. arterial wall) and b refers to blood properties. It is reminded that LTE model is employed for the arterial wall (Eq. (61)). Results show that the presence of large vessels has a significant effect on temperature distributions and must be accounted for when planning hyperthermia treatment.

Nabil et al. [86, 87] analysed time evolution and spatial distribution of particles and temperature in a tumor mass treated with superparamagnetic nanoparticles excited by an alternating magnetic field. The model illustrates a tumor slab of R3230AC mammary carcinoma on a rat model. The temperature distribution in the tumor is modelled by the following equation, which involves heat diffusion and convection by interstitial flow, heat absorption by lymphatic and capillary drainage:

$$\rho_{tm} c_{tm} \left[\frac{\partial T_{tm}}{\partial t} + \nabla \cdot \left(T\mathbf{u} - \alpha_{diff,e} \nabla T \right) + L_p^{LF} \left(p_{tm} - p_b \right) \left(T_{tm} - T_b \right) \right] + 2\pi P h \left(T_{tm} - T_b \right) \delta_{\wedge} = f_T \left(c_v \right) \tag{64}$$

where L_p^{LF} is the lymphatic permeability, P is the arithmetic average of the individual radii of each segment contained into the tumor, δ_{Λ} is a parameter to scale that refers to the microvascular network, and $f_T\left(c_v\right)$ is the source term caused by a low-frequency alternating magnetic field that causes nanoparticle exposure:

$$f_T\left(c_v\right) = \mathrm{SAR}\left(2\pi P\psi + \pi P^2 c_v\right)\delta_{\wedge} \tag{65}$$

where SAR evaluates the heat generated when nanoparticles are heated, ψ is the density of nanoparticles on the vascular walls, and c_v is the nanoparticle concentration in the blood flow. The term in Eq. (64) that describes lymphatic permeability is basically referred to the Starling equation related heat transfer, i.e., the heat transfer related to the transcapillar exchange. The proposed model is particularly adequate for this application, thanks to its capability of incorporating microvasculature configurations based on physiological data combined with coupled capillary flow, interstitial filtration and heat transfer, but the principal limitation is the difficulty of determining the model coefficients.

2.2. Conclusions

In this section, the key role of modeling heat transfer in human tissues in order to accurately predict temperature distribution in the human body has been highlighted, focusing on biomedical applications like hyperthermia treatments for cancer. Thermal ablation is one of the most promising application which cause cancer cells necrosis by means of different forms of electromagnetic energy, in particular in terms of RFA, MWA, HIFU or laser energy. The various bioheat models employed in cancer treatments by means of different hyperthermia techniques has described in depth, for the purpose of giving a clear overview of how the bioheat models have been modified when applied in different applications, in order to characterize specific thermal therapies.

3.

BIOHEAT TRANSFER IN A SPHERICAL BIOLOGICAL TISSUE: A COMPARISON AMONG VARIOUS MODELS

3. BIOHEAT TRANSFER IN A SPHERICAL BIOLOGICAL TISSUE: A COMPARISON AMONG VARIOUS MODELS

As described in previous sections, modelling heat transfer has a key role to predict accurately the temperature distribution in tissues treated with thermo ablative techniques, and various bioheat models have been developed throughout the years. In this section, different bioheat transfer models are compared simulating a thermal ablation treatment applied to a spherical domain of tissue. The biological tissue is modelled as a porous medium and liver tissue properties are used. Four different models, Pennes' model, Local Thermal Equilibrium equation (LTE), Local Thermal Non-Equilibrium equations (LTNE), and a three-energy equations model, are compared to appreciate differences among them in terms of temperature profiles, for two different porosities and three blood velocities. The effects of thermal ablation on the living tissue are included with a source term in the tissue energy equation. Furthermore, an analysis on radiative heat effects is also considered. Governing equations with the appropriate boundary conditions are solved with the finite-element code COMSOL Multiphysics®.

3.1. Geometry and properties

The vascular structures of tissue are supposed to be uniformly distributed in order to consider the physical model as a uniform porous medium.

The entire computational domain is a sphere with a radius of R_2=3.10 cm, and the heating zone within the biological tissue is a centrally located sphere with a radius of R_1=0.62 cm, as shown in Fig. 7. All the blood vessels are assumed to be straight in the blood flow direction (assumed to be the *z* direction of Fig. 7) and to merge in the porous medium, and both the entrance blood and the boundary temperatures are equal to 37 °C. In addition, thermal properties of tissue and blood are considered to be isotropic, and the heat transfer coefficient and blood velocity are supposed to be constant throughout the domain.

Furthermore, metabolic heat generation is neglected because it is much smaller than the power density released during the treatment.

In this study a vessel diameter of 15 μm and an intervessel distance of 140 μm are considered to yield an estimated porosity of 0.01 [72] and two values of porosities (0.005 and 0.05) are selected.

The relationship between volumetric heat transfer areas and diameters of blood vessels is given by Yuan [72], and resumed in Table 4, in which the different blood velocities related to the sizes of the vessels are included, according to the literature [45, 88, 89].

Thermal properties of tissue and blood are chosen according to the work by Kou et al. [90]. Thermal conductivity of tissue and blood is 0.5 W m^{-1} K^{-1}, densities of tissue and blood are 1050 kg m^{-3}, and specific heat capacities of tissue and blood are 3770 J kg^{-1} $K^{-1,}$ respectively.

To notice that the common input parameters are considered the same for the different models, because the focus is on the comparison among the different bioheat equations and not on the sensitivity of the models to the input parameters. Moreover, two heating conditions are assumed: 2 s heating with a power density of 50 x 10^6 W m^{-3} and 50 s heating with a power density of 2 x 10^6 W m^{-3}. The absorbed power density of blood is estimated to be one-tenth of that of tissue [91].

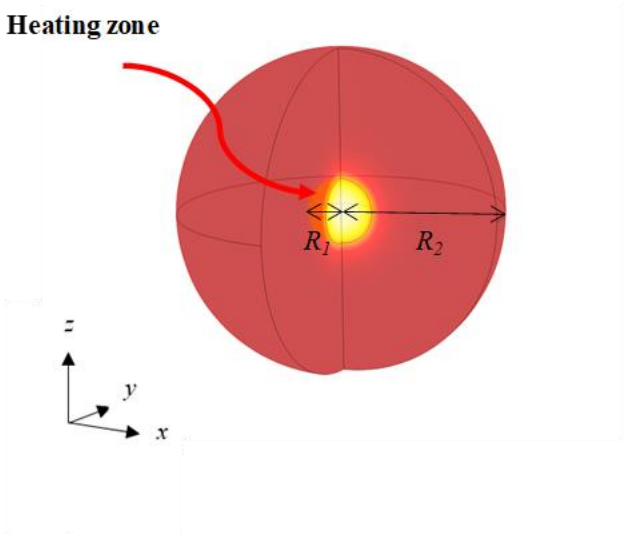

Figure 7. Schematic diagram of the calculation domain.

Table 4. Volumetric transfer areas for different porosities (ε) and vessels diameters (d).

	Volumetric transfer area a (m^2 m^{-3})	
	ε=0.005	ε=0.05
d=8 μm (u=0.07 cm s^{-1})	2500	25000
d=20 μm (u=0.3 cm s^{-1})	1000	10000
d=30 μm (u=0.4 cm s^{-1})	667	6667
d=50 μm (u=2 cm s^{-1})	400	4000
d=100 μm (u=3 cm s^{-1})	200	2000
d=140 μm (u=3.4 cm s^{-1})	143	1429

3.2. Mathematical models

3.2.1. Pennes' bioheat equation

The Pennes' bioheat equation, considering the external heat source and neglecting the metabolic heat source, can be written as:

$$(\rho c)_t \frac{\partial T_t}{\partial t} = \nabla \cdot (k_t \nabla T_t) + (\rho c)_b \, \omega_{Pennes} (T_a - T_t) + Q_{ext} \tag{66}$$

where t is the time and T is the temperature, the subscripts t, b and a stand for tissue, blood, and arterial blood, respectively, ρ is the density, c is the specific heat, k is the thermal conductivity, ω_{Pennes} is mean blood perfusion rate, that is selected to be 0.0036 s^{-1} for all cases [92], and Q_{ext} is the heat generation due to the ablation treatment. The blood temperature is assumed to be uniform throughout the tissue and it is

taken as body temperature equal to 37 °C. The tissue temperature T_t is equal to 37 °C at the boundary of the sphere R_2=3.10 cm and at the starting time t=0 s.

3.2.2. Local Thermal Equilibrium and Local Thermal Non-Equilibrium equations

As described in section 2.1 Xuan and Roetzel [48] introduced a two-equation bioheat model that considers the heat transfer in porous media. They modelled the biological tissue by dividing it into two different regions, namely, the tissue region and the blood region (i.e., solid phase consists of muscle, vascular tissues, and other solid compounds, while the fluid phase is made up by the blood flow that streams), without considering local thermal equilibrium between the two media and introducing an equivalent effective thermal conductivity in the energy equations of blood and tissue. Furthermore, they proposed an interfacial convective heat transfer term instead of perfusion one. So, Eqs. (37) and (38) are here applied to the spherical tissue, using for the heat transfer coefficient h a constant value of 170 W m^{-2} K^{-1} for all cases as in [72]. When the Local Thermal Equilibrium hypothesis is maintained, the temperature of the tissue is the same of the blood temperature, thus the LTNE Eqs. (37) and (38) are combined in the single Eq. (39).

3.2.2.1 The three-energy equation model

In 2008, Nakayama and Kuwahara [51] extended the two-equation model to three-equation model to consider the effect of heat transfer in closely spaced countercurrent artery-vein pair, illustrated in Fig. 8.

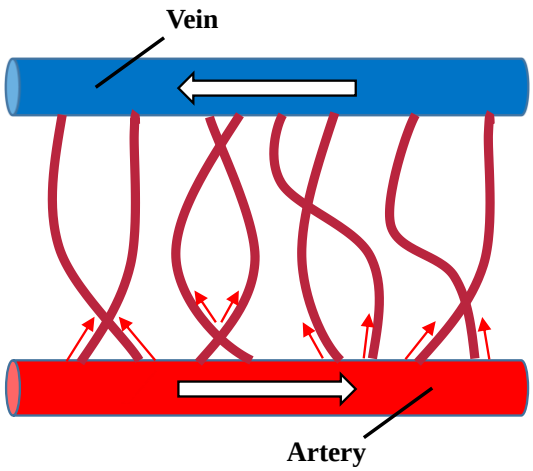

Figure 8. Schematic view of countercurrent heat exchange.

The three equations are derived for arterial blood phase, venous blood phase and tissue phase distinctively with three different temperatures as follows.

For the arterial blood phase:

$$\varepsilon_a (\rho c)_b \frac{\partial T_a}{\partial t} + \varepsilon_a (\rho c)_b \mathbf{u}_a \cdot \nabla T_a = \left[\varepsilon_a k_b + \varepsilon_a k_{dis,a} \right] \nabla^2 T_a - a_a h_a (T_a - T_t) - \omega_a (\rho c)_b T_a + \varepsilon_a Q_b \tag{67}$$

For the venous blood phase:

$$\varepsilon_v \left(\rho c\right)_b \frac{\partial T_v}{\partial t} + \varepsilon_v \left(\rho c\right)_b \mathbf{u}_v \cdot \nabla T_v = \left[\varepsilon_v k_b + \varepsilon_v k_{dis,v}\right] \nabla^2 T_v - a_v h_v \left(T_v - T_t\right) - \omega_v \left(\rho c\right)_b T_v + \varepsilon_v Q_b \tag{68}$$

For the tissue phase:

$$\left(1-\varepsilon\right)\left(\rho c\right)_t \frac{\partial T_t}{\partial t} = \left(1-\varepsilon\right) k_t \nabla^2 T_t + a_a h_a \left(T_a - T_t\right) + a_v h_v \left(T_v - T_t\right) + \left(\rho c\right)_b \left(\omega_v T_v + \omega_a T_a\right) + \left(1 - \varepsilon_a - \varepsilon_v\right) Q_t \tag{69}$$

The subscripts *t*, *a*, *v*, represent tissue, arterial and venous blood, respectively, while k_{dis} is the thermal dispersion conductivity, which can be estimated according to the relationship in [93]:

$$k_{dis} = \frac{3\varepsilon_a \left[\left(\rho c\right)_b\right]^2 \left|\mathbf{u}_b\right|^2}{14 a_a h_a} \tag{70}$$

Following the studies of Nakayama et al [51, 94], some assumptions have to be considered:

- $\varepsilon_a = \varepsilon_v$ and $\varepsilon_a + \varepsilon_v = \varepsilon$;
- $a_a h_a = a_v h_v$;
- $u_a = u_v$;
- $\omega_a = -\omega_v$.

In this model the convective heat transfer coefficients *ah* considered in the LTNE equations, are replaced by the convection-perfusion terms, namely ($a_a h_a \pm (\rho c)_b \omega$) [95]; furthermore, the perfusion rate ω should vary locally, unlike that of Pennes, but it is assumed that its local value is provided everywhere, and its value varies in the range from 2 x 10^{-4} s^{-1} to 5 x 10^{-4} s^{-1} [51], thus, the value of blood perfusion is selected to be 0.0005 s^{-1} for all cases, considering the value that reduces mostly the heat transfer coefficient; specifically, h=156.1 W m^{-2} K^{-1} in the worst case, for porosity ε=0.005 and blood velocity modulus u=3.4 cm/s.

3.3. Numerical approach and validation

The bioheat transient models are implemented by using the finite-element commercial code COMSOL Multiphysics software. A 2D axisymmetric model is used to minimize computational efforts and consequently computing time. The mesh chosen for all the models has 11746 triangular elements; thicker meshes have been tested on temperature profiles, but without improvements. As regards the transient solver, the absolute tolerance used is 0.001, the time stepping method is the intermediate BDF with initial and maximum steps of 0.001 s and 1 s respectively for the 50 s heating case. For the 2 s heating condition, the maximum step considered is 0.1 s. In order to validate the presented different mathematical models, simulation results of tissue temperature distributions at the center of the sphere are then compared against

the results obtained by Yuan [72], in which LTNE and LTE models are implemented for different conditions of porosity, blood velocities and heating conditions for a cubical tissue. The sphere has the same volume of the Yuan's cube, in order to have the same heating power density; moreover, the properties of blood and tissue, the blood velocities and the heating conditions chosen are identical in order to validate the results obtained in COMSOL. The LTNE and LTE models have been simulated in COMSOL for all porosities, blood velocities and heating conditions and they fit the results obtained by Yuan very well in all cases.

In Fig. 9 only the extreme cases of LTNE equations have been presented, considering three blood velocities, i.e., Fig. 9(a) shows the results for ε=0.005, Q_t= 2 x 10^6 W m^{-3} and the blood velocities u=0.07 cm s^{-1}, u=0.4 cm s^{-1}, u=3.4 cm s^{-1}; Fig. 9(b) regards the outcomes for ε=0.05, Q_t= 50 x 10^6 W m^{-3} and the same three blood velocities. An excellent agreement with literature data has been found.

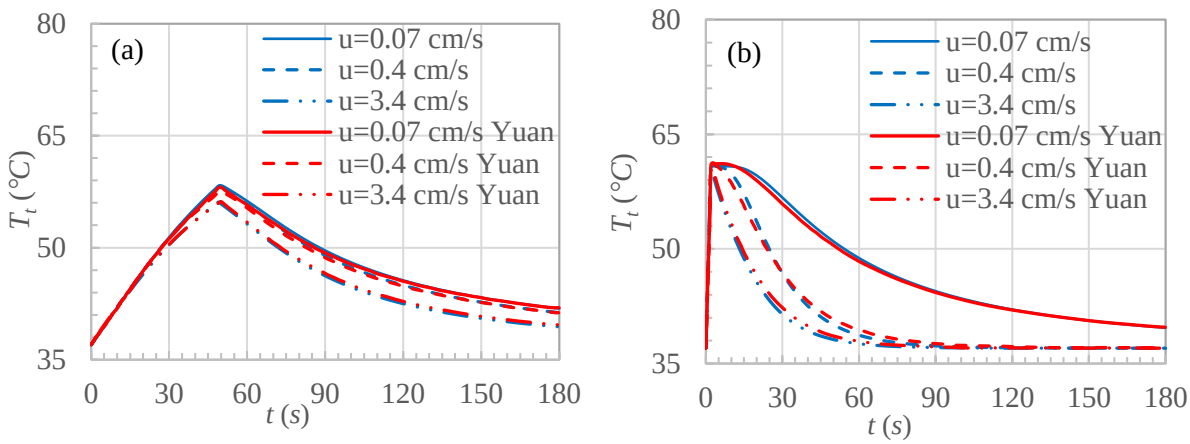

Figure 9. Temperature distributions of LTNE model compared with Yuan's LTNE equations [72]: (a) ε=0.005, Q_t= 2 x 10^6 W m^{-3}; (b) ε=0.05, Q_t= 50 x 10^6 W m^{-3}.

3.4. Results

In this section all the tissue temperatures at the central point of the sphere obtained from the simulations for the different analyzed bioheat models are presented and compared at the same blood velocities, considering four separate cases as described in Figs 10-13.

Comparing Fig. 10 to Fig. 12 and Fig. 11 to Fig. 13, the first result to underline is that for all the models the maximum temperature increases in the case of shorter heating duration, but in this condition of quick heating the temperature drop rate occurs more rapidly than in the longer heating because of the enhanced heat transfer. Another common conclusion for all the models is that the temperature decreases with an increase in porosity because higher porosity means having more blood to carry the heat away from the tissue, see Fig. 10 vs. Fig 11 and Fig. 12 vs. Fig. 13. Moreover, the Peclet number $\varepsilon u \rho_b c_b 2R_2/k_b$ that represents the ratio of heat transfer by motion of a fluid to heat transfer by thermal conduction, increases as the porosity increases too, so the advection term becomes more important than the conductive one, and consequently the temperature decreases more quickly. Obviously, this is not valid for the Pennes' equation, that is not referred to a porous medium.

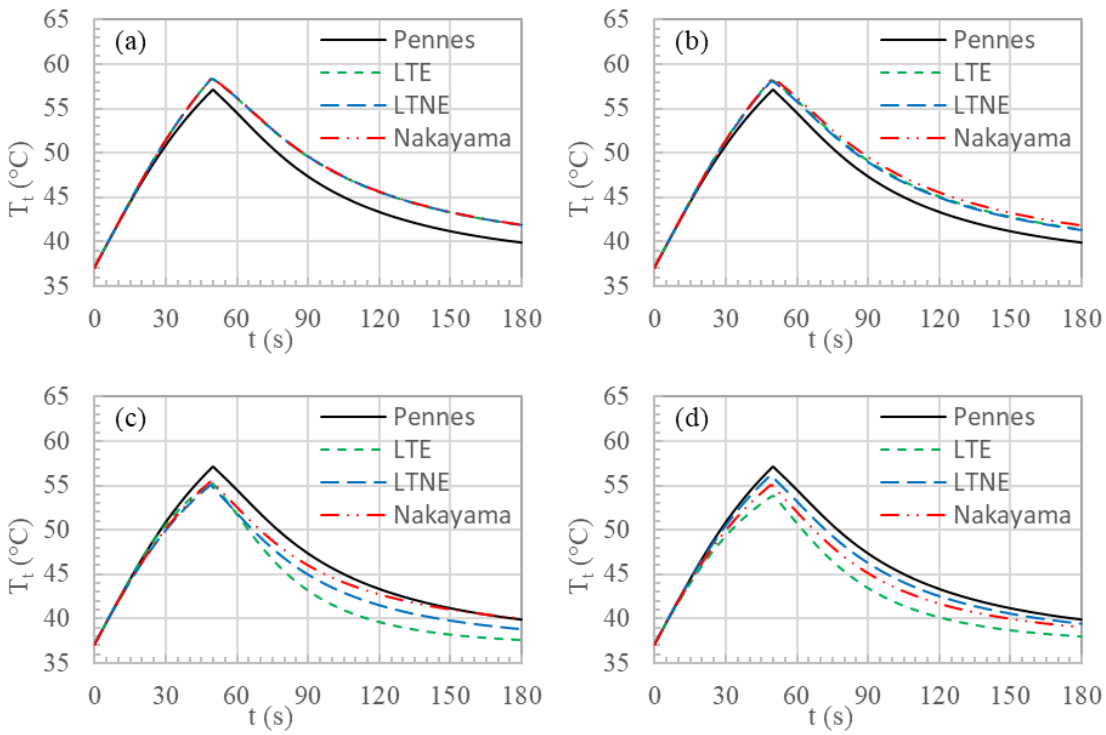

Figure 10. Tissue temperature distributions for ε=0.005, Q_t= 2 x 10^6 W m^{-3} when heating time is 50 s: (a) u =0.07 cm/s, (b) u=0.4 cm/s, (c) u =2 cm/s, (d) u =3.4 cm/s.

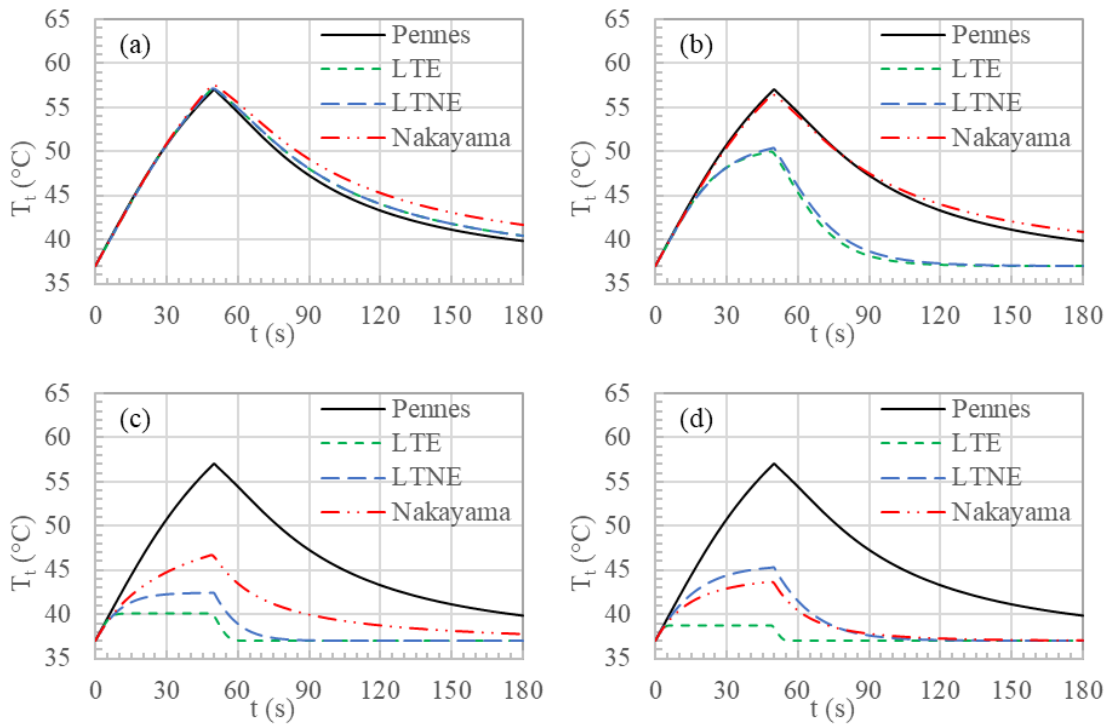

Figure 11. Tissue temperature distributions for ε=0.05, Q_t= 2 x 10^6 W m^{-3} when heating time is 50 s: (a) u =0.07 cm/s, (b) u =0.4 cm/s, (c) u =2 cm/s, (d) u =3.4 cm/s.

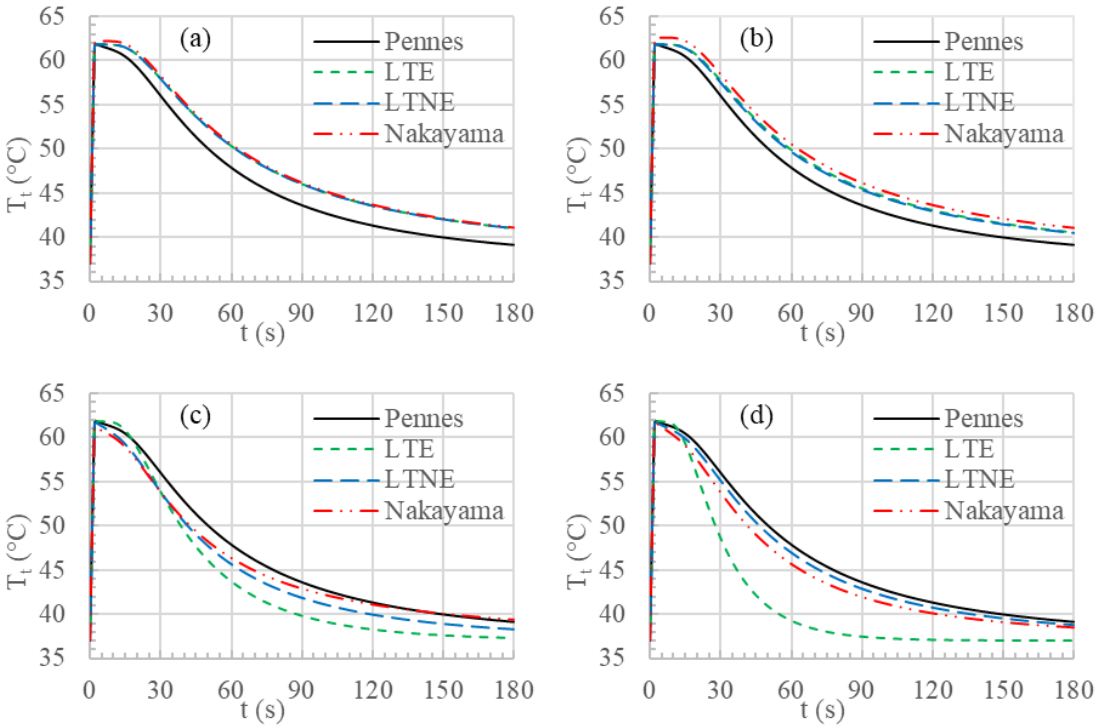

Figure 12. Tissue temperature distributions for ε=0.005, Q_t= 50 x 10^6 W m^{-3} when heating time is 2 s: (a) u=0.07 cm/s, (b) u=0.4 cm/s, (c) u=2 cm/s, (d) u=3.4 cm/s.

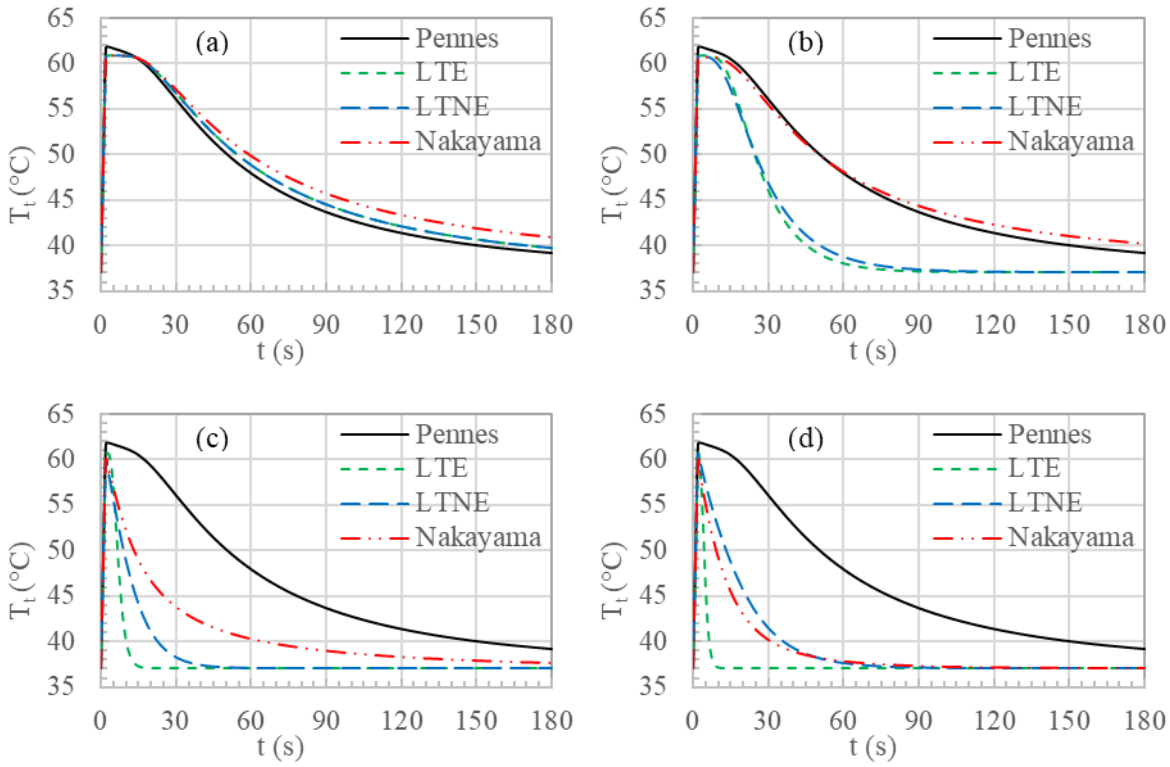

Figure 13. Tissue temperature distributions for ε=0.05, Q_t= 50 x 10^6 W m^{-3} when heating time is 2 s: (a) u=0.07 cm/s, (b) u=0.4 cm/s, (c) u=2 cm/s, (d) u=3.4 cm/s.

Comparing LTNE and LTE models for the two porosities considered, they yield the same results for lower velocities, specifically for u<0.4 cm s^{-1}, which means that the LTE equation is suitable for predicting the temperature during thermal ablation treatment when the blood vessels distributed in the tissue have a diameter less than 30 μm (capillaries, arterioles and terminal arteries); for higher velocities (and consequently vessels diameters), the LTE model overrates the heat carried out by the blood flow; in particular, the increase of velocity corresponds to a decrease of the Stanton number, which relates heat transfer coefficient to heat capacity of the fluid stream per unit cross-sectional area per unit time, namely $h/(u\rho_b c_b)$, so the LTNE equations have to be used. In addition, for the LTNE equations the tissue temperature drops as the blood velocity rises, until u=2 cm/s; for higher velocities, the temperature restarts to increase because the higher velocity is compensated by the growth of the volumetric transfer area a. These considerations on different velocities are not valid for the Pennes' model, which does not consider the blood velocity, but only the blood perfusion.

As regards the Nakayama three-energy equation model, the results are in good agreement with the LTNE model for the lowest porosity and both the heating conditions, while for ε=0.05 it yields higher temperatures than the LTNE ones, except for the highest velocity u=3.4 cm/s, when LTNE equations result in higher temperatures. However, this more complex model requires more detailed anatomical data compared to others, so its application could be useful only in particular case, such as when artery and vein temperatures have necessarily to be considered different.

To notice that typical values of tissue temperatures are higher than 55 °C because the goal of thermo ablation therapy is the necrosis of tumoral tissue, and this can be obtained with different combinations of input power and time of application depending also on the tumor dimension, for example from 32 W to 180 W for a total duration of the corresponding treatment of 15 min and 6 min as described in [96]. On the other hand, the surrounding healthy tissue has to be preserved and the medical probe usually cannot support temperatures higher than 120 °C, so it is preferable to not overcome 100 °C. For these reasons, the differences observed are important especially considering higher input powers and application times.

In addition, it is interesting to show the computational times of the different models' simulations, more in particular, it has been chosen the most onerous case, which is referred to Q_t= 50 x 10^6 W m^{-3} when heating time is 2 s, for ε=0.05, and u=3.4 cm s^{-1}. In this situation, using a 2.50 GHz Intel Core i7-4710MQ CPU and a 16 GB 799 MHz DDR3 RAM, the computational times for Pennes' equation, LTE model, LTNE equations and three-energy equation model are 30'19'', 33'37'', 45'23'', and 59'50'' respectively. These results confirm the simplicity of Pennes' bioheat model, which is also the less onerous computationally, but in this case, it produces not accurate outcomes. In the other cases, the computational times are comparable to the Pennes' ones, so it has not been reported.

3.5. Radiative heat transfer effects

Radiation effects on the biological medium considered in this paper can be analysed with two simplified approaches, the Rosseland diffusive approximation and the Beer-Lambert-Bouguer law; the first assumes

the medium to be optically thick and allows to define a "radiative conductivity" as follows:

$$k_r = \frac{16n^2\sigma_s T^3}{3\beta} \tag{71}$$

where n is the refractive index, assumed to be 1.4 [27], σ_s is the Stefan-Boltzmann constant and β is the extinction coefficient, considered equal to 5550 m^{-1}, according to the study of optical properties of ex vivo human tissues by Simpson et al. [97]. The Beer-Lambert-Bouguer law, instead, is a simplified form for the Radiative Transfer Equation in which the radiation is assumed to be collimated, and consequently the radiative heat flux divergence (heat source term for the governing equations) could be written as:

$$\nabla \cdot q_R = -\beta I_0 e^{-\beta\sqrt{r^2+z^2}} \tag{72}$$

where I_0 is the intensity of radiation measured in W m^{-2}. Since one can assume that the energy irradiates from the internal sphere to the external (the internal sphere acts as a catheter with a spherical tip), the heat exchange area for the radiation contribution is the internal/external spheres contact surface area. This because if one assumes that the radiative source is pointwise, for r = 0 one can have an infinite value of the radiative source term in Eq. (72). For this reason, tissue temperature is evaluated at r=0.62 cm in the model that accounts for the Beer-Lambert-Bouguer law and consequently it is compared with tissue temperature at r=0.62 cm for LTNE. Radiative contribution effects are presented in Fig. 14 for both Rosseland approximation and Beer-Lambert-Bouguer law. It is shown that in both cases the radiative contribution does not affect the tissue temperature in all the models considered and can be neglected, even in the case of the maximum temperature reached (i.e., for ε=0.005, Q_t= 50 x 10^6 W m^{-3}, u=0.07 cm/s and when heating time is 2 s).

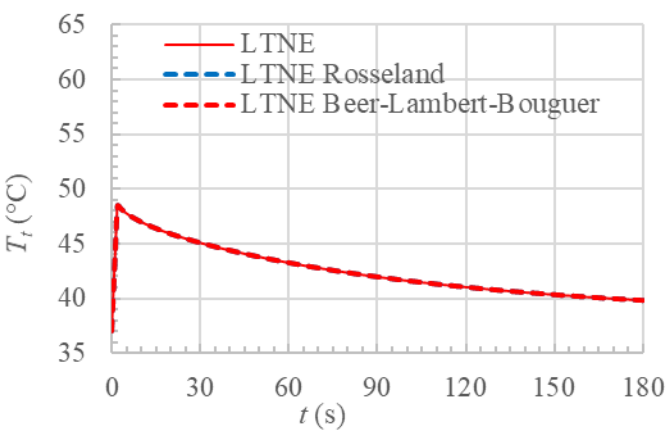

Figure 14. Tissue temperature profiles evaluated at r=0.62 cm for LTNE model compared with tissue temperatures reached taking into account the radiative contributions from the Rosseland approximation and Beer-Lambert-Bouguer law, for ε=0.005, Q_t= 50 x 10^6 W m^{-3}, u=0.07 cm/s and when heating time is 2 s.

3.6. Conclusions

In this section, four models have been compared in modelling heat transfer in a spherical biological tissue: the simplest Pennes' equation, the Local Thermal Equilibrium equation, the Local Thermal Non-Equilibrium equations and the three-equation model. By using the finite-element commercial code COMSOL Multiphysics software, the tissue temperature profiles versus time are presented for each model under different porosities, blood velocity, vessels diameters and heating conditions. According to the results, the Pennes' model shows its inaccuracy due to its simplicity, while the LTE model is suitable to predict temperatures during thermal ablation therapy when the diameter of the blood vessels is less than 30 μm, which corresponds to the low blood velocity of 0.4 cm s^{-1}. For higher velocities, and consequently vessels diameters, the LTE model overrates the heat carried out by the blood flow, so the LTNE equations have to be used to take into account interfacial convective heat transfer. As regards the Nakayama three-energy equation model, the results are in good agreement with the LTNE model for the lowest porosity and both the heating conditions, even if this model requires more detailed anatomical data compared to others, so its application could be useful only in particular case, such as when artery and vein temperatures have necessarily to be considered different. This means that the LTNE model gives the best trad off between accuracy and simplicity. Finally, radiative heat transfer effects have been analyzed by employing either Rosseland approximation or Beer-Lambert-Bouguer law, showing that radiation through biological tissues is negligible for the conditions herein presented.

4.

PULSATING HEAT SOURCES APPLIED IN A TUMOR TISSUE

4. PULSATING HEAT SOURCES APPLIED IN A TUMOR TISSUE

Modulation of heat sources can be employed during different treatments for human beings in many clinical applications. Sluijter [98, 99] showed that for spinal pain a pulsed radiofrequency treatment does not cause any neural damage because of the lower temperature achieved during the treatment. Munglani [100] presented some case reports, in which effects of this technique are presented for patients with neuropathic pain, concluding that results were very promising. Cohen and Foster [101] treated three patients with groin pain and orchialgia with this technique, achieving complete pain relief after their six-months follow-up visit. Other examples of clinical applications are trigeminal neuralgia treatments [102], cervicogenic headache [103], ultrasound hyperthermia drug delivery [104], or tumor ablation.

With references to tumor ablation, various solutions have been proposed in literature through the years. Goldberg et al. [105] analyzed by means of experiments on animals with both ex vivo and in vivo techniques two different methods of pulsating RF ablation, i. e. with constant peak current with variable duration and with variable peak current but with a specified minimum duration. They concluded that variable peak current can be useful to treat larger tumors since coagulation diameter is bigger. The same pulsating algorithm has been used by Ahmed et al. [106] in their study on NaCl injection effects on radiofrequency ablation in animal models. A numerical study on different heating scheme for hyperthermia treatment has been presented by Khanafer et al. [85], with an emphasis on heating propagation on large vessels. By employing a physiological waveform for the inlet velocity profile at the vessel entrance, they assume uniform temperature outside the vessel, and they compared different heating protocols by making this temperature variable through time. They compared uniform heating scheme with a pulsating heating one with an interval of 3 seconds. The authors concluded that temperatures are lower with pulsating heat schemes, that might cause normal tissue damage. López Molina et al. [107] analytically studied pulsed radiofrequency ablation by employing both hyperbolic and Fourier heat transfer equation, that considers thermal wave effects. Their model is based on a spherical electrode placed in a biological tissue. Heat is supplied by means of a waveform, and this is coupled to the heat transfer equation by means of the Joule heat distribution via solving Laplace's equation for the voltage field.

Another reason why pulsating heat protocol might be useful concerns the roll-off phenomenon. The roll-off is the augmentation of electrical impedance due to tissue dehydration and charring, that reduces heat transfer and might cause problems like reduced coagulation zones. Fukushima et al. [108] treated fifteen patients with hepatocellular carcinoma either conventional temperature control or by controlling impedance. They conclude that patients with impedance control have larger ablation zones and reduced ablation times, with almost equal energy requirements. A numerical model for impedance-controlled pulsing protocol has been presented by Trujillo et al. [109]. In their model, a cooled electrode is employed for either pulsating current or pulsating voltage cases, obtaining results that match pretty well experiments. The relationship between the area of target tissue necrosis and target tissue size when a pulsating protocol is applied has been numerically investigated by Zhang et al. [110]. Different waveforms have been compared, and the half square provided a larger ablation area than the half-sine wave, while the maximum applied voltage, that can be applied without any roll-off, has been found to be lower with higher target

tissue diameters in all cases.

Pulsating protocols have been proposed for microwave ablation too. Microwave ablation is useful for larger ablation zones because of the reduction of heat-sink effect. Bedoya et al. [111] experimentally examined both ex vivo bovine liver and in vivo porcine livers by employing different heating protocols at equal delivered energy, i. e. 15 kJ for the ex vivo and 30 kJ for the in vivo case. The authors concluded that for the in vivo case the pulsed protocol can make larger ablation zones with lower average power, and that an optimization of this protocol is required. Switched-mode ablation and synchronous ablation have been numerically and experimentally analyzed by Biffi Gentili and Ignesti [112], showing that these two techniques provide the same ablative performance.

4.1. Numerical analysis of the pulsating heat source effects in a tumor tissue

4.1.1. Mathematical model

The geometry representing the biological tissue is here made up of two spheres having the same center but different radius, as shown previously in section 3.1. So, the radius of the internal and external spheres are $R_1 = 0.62$ cm and $R_2 = 3.10$ cm respectively, and the heating source is in the internal sphere as it is displayed in Fig. 7.

The biological structure is treated by means of the porous media theory [17], which recognizes two different phases: the cells and interstitial space represent the tissue phase, that is the solid phase; on the other hand, the blood vessels, that infiltrate through the solid phase, are the fluid phase. With regard to the bioheat model, a two-equation Local Thermal Non-Equilibrium (LTNE) model is employed. Considering the conservation of energy to the tissue and blood, the two differential equations are formulated as follows.

For the blood phase:

$$\varepsilon(\rho c)_b\left(\frac{\partial\langle T_b\rangle}{\partial t}+\langle\mathbf{u}\rangle\cdot\nabla\langle T_b\rangle\right)=\varepsilon k_b\nabla^2\langle T_b\rangle+ha\left(\langle T_t\rangle-\langle T_b\rangle\right)+\varepsilon Q_{ext} \tag{73}$$

For the tissue phase:

$$(1-\varepsilon)(\rho c)_t\frac{\partial\langle T_t\rangle}{\partial t}=(1-\varepsilon)k_t\nabla^2\langle T_t\rangle-ha\left(\langle T_t\rangle-\langle T_b\rangle\right)+(1-\varepsilon)Q_{ext} \tag{74}$$

with ε the porosity, ρ the density, c the specific heat, T the temperature, t the time, $\mathbf{u}$ the velocity vector, h the interfacial heat transfer coefficient, a the volumetric heat transfer area between tissue and blood, Q_{ext} the external power density imposed during the treatment.

As regards the fluid phase, all the blood vessels are assumed to be aligned in the blood flow z direction, the initial blood and the boundary temperatures are equal to 37 °C, as for the solid phase. In addition, the entire geometry is implemented with 2D axisymmetric model, so the adiabatic condition is employed on the symmetry axis. The thermal properties of the two phases are considered isotropic and constant with

temperature, while both interfacial heat transfer coefficient and blood velocity are supposed to be uniform across the computational domain.

Thermal properties of tissue and blood are chosen according to B. Zhang et al. [110] as it is shown in Table 5.

Table 5. Thermal properties of tumoral tissue and blood used in this study.

	ρ (kg m^{-3})	c (J kg^{-1} K^{-1})	k (W m^{-1} K^{-1})
Tumoral tissue	1045	3760	0.600
Blood	1000	4180	0.490

In addition, the interfacial heat transfer coefficient h is here chosen 170 W m^{-2} K^{-1}, as in Yuan [72]. The specific surface area, a, is obtained from the definition of hydraulic diameter in a porous media [113, 114].

$$a = \frac{4\varepsilon}{d} \tag{75}$$

where d is the blood vessel diameter. In this study, three different blood vessel diameters are considered, which correspond at three different blood velocities u, following the work of Crezee and Lagendijk [88]. More in detail, diameters and velocities of capillaries, secondary veins and main veins are selected, as in Table 6. Moreover, three different porosities i.e., ε_1 = 0.05, ε_2 = 0.2 and ε_3= 0.6 for the biological tissue are investigated, so both the consequent specific surface areas a and volumetric convective coefficients h_v=ha are displayed.

Table 6. Values of diameters and blood velocities in the present work.

	d (mm)	$\lvert\mathbf{u}\rvert$ (cm s^{-1})	a (m^{-1})			h_v=ha (W m^{-3} K^{-1})		
			ε_1 = 0.05	ε_2 =0.2	ε_3 = 0.6	ε_1 = 0.05	ε_2 =0.2	ε_3 = 0.6
Capillaries	8.00E-3	7.00E-2	2.50E4	1.00E5	3.00E5	4.25E6	1.70E7	5.10E7
Secondary veins	1.50	1.30	1.33E2	5.33E2	1.60E3	2.26E4	9.06E4	2.72E5
Main veins	2.40	1.50	8.33E1	3.33E2	1.00E3	1.42E4	5.66E4	1.70E5

Regarding the external heating, that is the power density given to the tissue, Q_{ext} (1 - ε) = 5.6 x 10^6 W m^{-3}, it is assumed to be the same among the different cases considered and such that the tissue temperature is as low as to neglect phenomena like evaporation. Furthermore, to take into consideration pulsating heating effects, a modular power density is employed, considering the following cosine function:

$$f\left(\omega_p, t\right) = \left[\frac{1}{2} + \frac{1}{2}\cos\left(\omega_p t\right)\right] \tag{76}$$

where ω_p is the pulsation and t the time. To determine a reference pulsation to define a scaled pulsation/period, a steady state reference case needs to be defined. It is assumed that for the ablation time considered in this work, t = 50 s, the sinusoidal function has to be 0.95. In this case a reference pulsation is determined equal to ω_{p0} = 0.00902 s^{-1}. A dimensionless period T^* is defined as $T^* = \omega_p^*/2\pi$, while $\omega_p^* = \omega_{p0}/\omega_p$ is the dimensionless pulsation. The dimensionless pulsation becomes 1 for the mentioned above steady state reference case. It is shown that the lower is the dimensionless period, the higher is the pulsation. The following Fig. 15 displays different pulsating functions vs time, for different values of dimensionless period T^*.

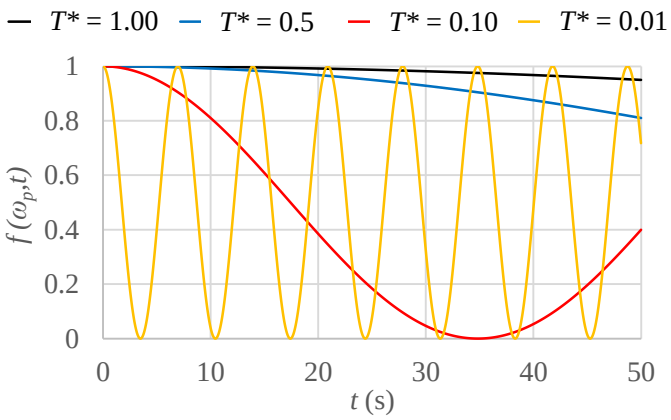

Figure 15. Cosine functions for different dimensionless period.

Moreover, it is important to compare pulsating and non-pulsating cases at equal energy density. This because, if the heating time is the same, the pulsating heat will yield lower temperatures since less energy is delivered to the tissue and the ablated zones will not be comparable. In order to obtain the same energy, the total heating time t_{pul} for pulsating heating case needed to obtain the same power density of non-pulsating case is calculated solving the equation below:

$$Q_{ext} t_{st} = \int_0^{t_{pul}} Q_0 \left[\frac{1}{2} + \frac{1}{2} \cos(\omega t) \right] dt \tag{77}$$

where t_{st} is the steady state heating time that is 50 seconds. Solving the integral, the following equation is found:

$$Q_{ext} t_{st} = \frac{Q_{ext}}{2} t_{pul} + \frac{Q_{ext}}{2\omega_p} \sin(\omega_p t_{pul}) = \frac{Q_{ext}}{2} \left[t_{pul} + \frac{\sin(\omega_p t_{pul})}{\omega_p} \right] \tag{78}$$

This equation is solved by employing an in-house MATLAB code. Roots of the equations obtained for different ω_p, and then ω_p * and T^* obtained from Eq. (78) are represented in Fig. 16 for different T^*. It is shown that the total time approaches to an asymptotic value that is equal to $2t_{st}$. This because the sinusoidal

component of Eq. (78) becomes negligible for low T^* (and high ω_p). In particular, from values of $T^* < 1.00 \times 10^{-2}$ this is true with an error of ± 1%, as observed in Fig. 16.

In this work, three different dimensionless periods are examined, *i.e.*, $T^* = 1.00 \times 10^{-4}$, $T^* = 1.03 \times 10^{-2}$ and $T^* = 2.87 \times 10^{-2}$, which correspond to periods equal to $T_p = 6.96 \times 10^{-2}$ s, $T_p = 7$ s, and $T_p = 20$ s respectively, as it is shown in Fig. 16, where the vertical lines point at the three dimensionless periods chosen.

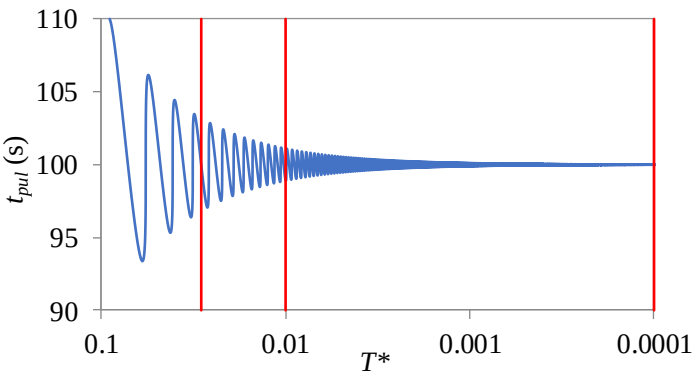

Figure 16. Total time of pulsating heating vs dimensionless period.

The choice of these values is related to both the purposes of considering three different sizes of periods and at the same time avoiding too high widths in temperature oscillations.

4.1.2. Numerical approach and validation

Governing equations are numerically solved with the finite element commercial code COMSOL Multiphysics and a 2D axisymmetric model is employed in order to minimize computational time. A triangular mesh of 8768 elements is here used and the grid convergence is verified on the maximum temperature as in Table 7 below, where negligible temperature differences for the most significative case are displayed. The 2D computational domain and the mesh are shown in Fig 17.

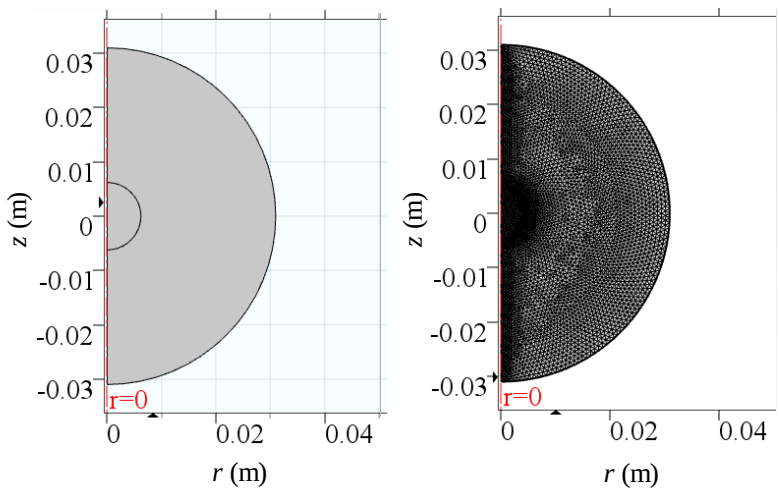

Figure 17. 2D computational domain and mesh.

PARDISO direct solver is employed to solve governing equations, and second order Lagrangian elements are used to discretize equations. Moreover, the absolute tolerance used for the transient solver is 0.0001, the time stepping method is the intermediate BDF with initial and maximum steps of 0.001 s and 0.1 s, respectively.

Comparisons between the disclosed mathematical model and numerical results from Yuan [72] are here presented as in section 3.3, showing the tissue temperature profiles at the center of the sphere. It has to be highlighted that the geometry chosen by Yuan [72] is a cube with the same volume of the sphere employed in the present work, so, the applied external power density is the same. The LTNE equations are simulated in COMSOL Multiphysics and the results agree very well in all cases, as it is shown in Fig. 9 of the previous section 3.3 for different blood velocities, porosities, and heating conditions.

Table 7. Maximum value of tissue temperature for different numbers of triangular elements.

Number of triangular elements	Maximum tissue temperature
2192	96.77 °C
4384	96.82 °C
8768	96.85 °C
17536	96.86 °C

4.1.3. Results

In this paragraph results obtained with pulsating and non-pulsating heating conditions are presented. The maximum tissue temperatures reached for different blood vessels diameters, porosities and dimensionless period are presented. It is shown that pulsating effect always reduces maximum temperatures, even reaching about 30% lower maximum temperatures compared to the non-pulsating case. By comparing the three different dimensionless periods T^*, it seems that maximum temperature achieved is independent of T^* in these cases. This because when pulsating heat occurs there is no relaxation time for heat to appreciate temperature differences. The maximum temperature reduction (that is between about 10 °C and 25 °C) is a very important result since it allows to reduce the steam popping phenomenon that occurs in thermoablation [115]. By comparing different diameters, in Fig. 18 it is shown that the lowest temperatures are reached for d = 1.5 mm in all cases. This because this diameter corresponds to the highest volumetric heat exchange between the two phases (see the second term on the right side of Eqs. (73) and (74), that depends on a compromise between volumetric heat transfer coefficient (see Table 6) and blood flow velocity.

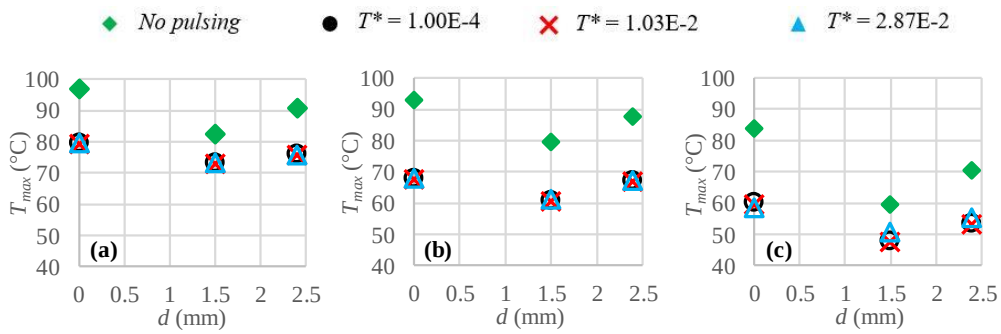

Figure 18. Maximum tissue temperatures at the center of the sphere for pulsating and non-pulsating heating, when d=0.008 mm (capillaries), d=1.5 mm (secondary veins), and d=2.4 mm (main veins), for (a) ε=0.05, (b) ε=0.2 and (c) ε=0.6.

Indeed, heat goes to the solid phase and it is removed by the fluid phase and its velocity. The quality of this heat exchange depends on the volumetric heat transfer coefficient and on blood flow velocity. However, this point will be clarified later.

In Fig. 19, maximum tissue temperatures for the different porosities are compared at equal diameters. Again, maximum temperatures are reduced with pulsating heat of about 30% for the best case. By comparing different porosities, it is shown that maximum temperatures are always inversely proportional to porosity. This because the higher is the porosity the higher are the blood volume fraction and the volumetric heat exchange between the two phases, so the heat is removed mainly from tissue.

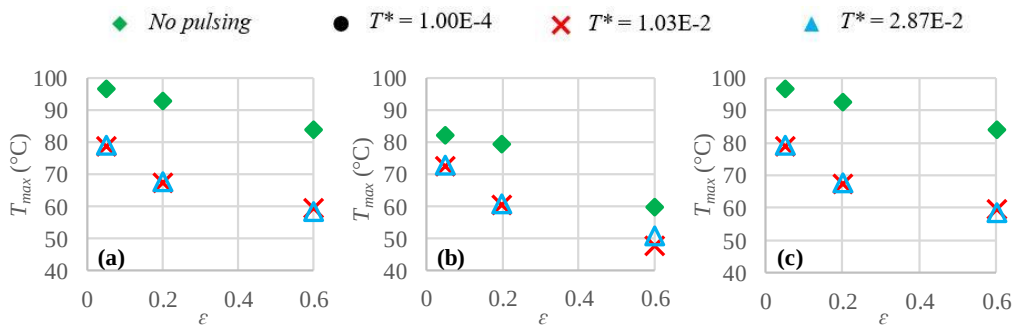

Figure 19. Maximum tissue temperatures at the center of the sphere for pulsating and non-pulsating heating, when ε=0.05, ε=0.2 and ε=0.6. for (a) d=0.008 mm (capillaries), (b) d=1.5 mm (secondary veins), and (c) d=2.4 mm (main veins).

Tissue temperature profiles at the center of the sphere as a function of time are displayed in Fig. 20 for different blood vessels diameters, porosities, and dimensionless pulsating heating periods.

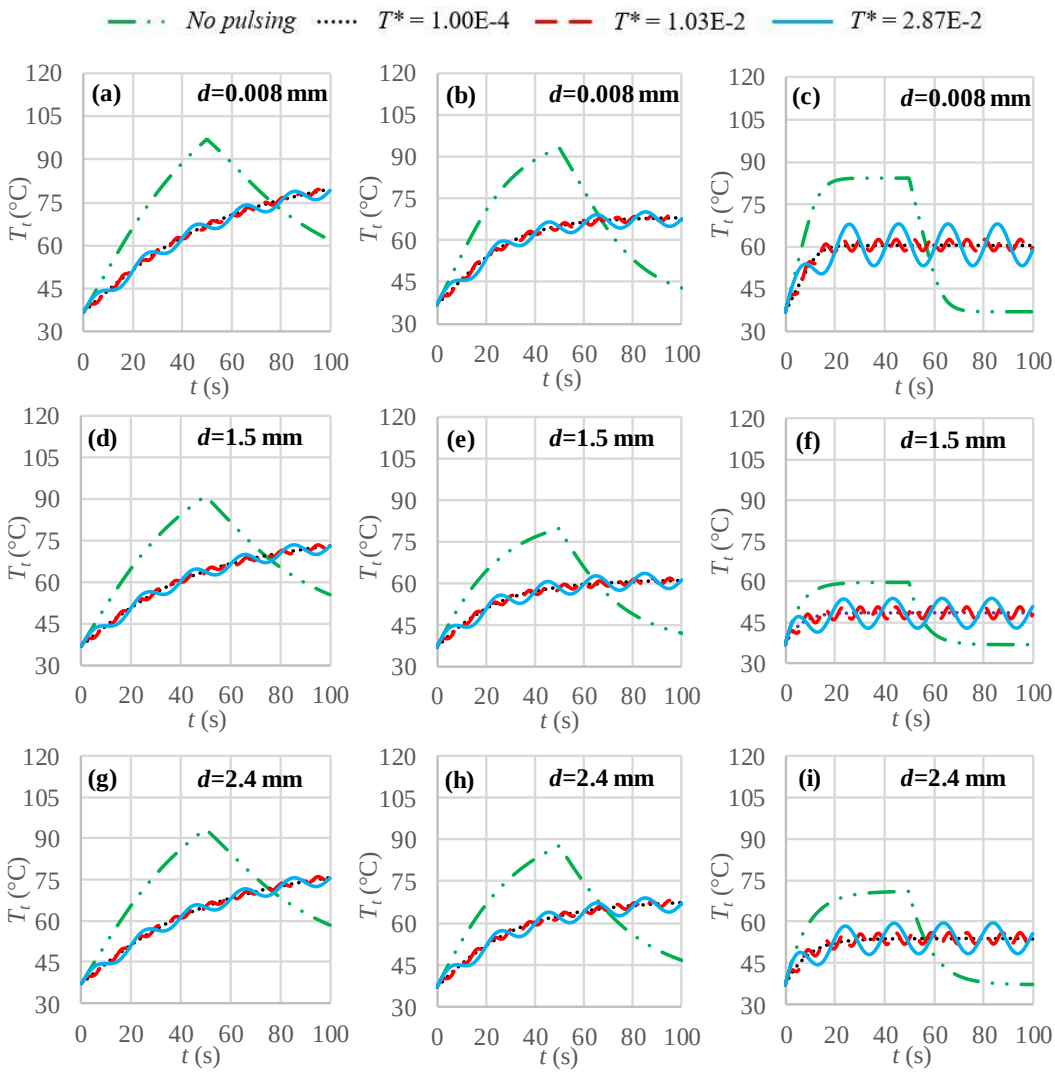

Figure 20. Tissue temperature distributions at the center of the sphere for pulsating and non-pulsating heating, when d=0.008 mm (capillaries), d=1.5 mm (secondary veins), and d=2.4 mm (main veins), for (a, d, g) ε=0.05, (b, e, h) ε=0.2 and (c, f, i) ε=0.6.

For the non-pulsating condition, it is shown in all cases that temperature tends to increase since a certain time, that corresponds to the heating time. After this time, there is a slow decay because the tissue tends to reach external applied temperature, that is 37 °C.

In some cases, especially for high porosity, this temperature is achieved in reasonable time (say, about 100 seconds). With references to different dimensionless periods, temperatures achieved are generally lower when pulsating heat is applied, as previously shown in Figs. 18 and 19 for maximum temperatures. In particular, temperature outlines related to the three different periods are very similar for the lowest porosity, while for ε=0.6 the dimensionless periods $T^* = 2.87 \times 10^{-2}$ causes wider oscillations that result in higher temperature differences. To notice that the tissue temperature decreases with the increase of porosity when the blood vessels diameters and the dimensionless periods are the same, because higher the porosity more the blood and more the heat removed from the tissue, as previously shown in Fig. 19 for maximum temperatures for different porosities.

In Fig. 21 convective heat rate per unit volume *vs* time is shown for all the different conditions of porosity, diameter, and dimensionless periods. The convective power density is referred to the second term on the right side of Eqs. (73) and (74). It represents the heat rate between the two phases of the porous medium per unit volume and depends on a compromise between volumetric heat transfer coefficient (see Table 6) and blood flow velocity. Indeed, the heat applied in the tissue goes to the blood flow phase depending on this. It is shown that convective heat rate per unit volume depending on blood vessels diameters at equal porosity has maximum values for d = 1.5 mm. On the other hand, it increases with porosity at equal diameter. These trends are consistent to what has been previously shown in Figs. 18 and 19 for maximum temperature achieved in the tissue.

As shown above, the most powerful result achieved using a pulsating heat source instead of a constant one is the decreasing of maximum temperature in any considered case to avoid steam pops [115] and the roll off phenomenon [116] during radiofrequency ablation. However, it has to be guarantee that the tumoral tissue destroyed is enhanced when pulsating heat is applied, or at least equal to the non-pulsating heat case. This means that it is important to reach the temperature threshold of necrosis of about 55 °C [117]. Moreover, there are other different methods to evaluate the target tissue necrosis, such as the cumulative equivalent minutes at 43 °C and the Arrhenius model [110]. In this work, the Arrhenius equation is implemented, and the degree of tissue necrosis is defined as previously described in Eq. (4a). In this work, $A = 3.247 \times 10^{43}$ (s^{-1}) and $\Delta H = 2.814 \times 10^{5}$ (J mol^{-1}) are taken from literature [118]. In Fig. 22 the percentage of necrotic tissue vs the radius of the spherical tissue is shown for all cases here investigated at t_{st} = 50 s for the non-pulsating condition and at t_{pul} = 100 s for the pulsating one, that correspond to the end of thermal ablation for both cases, in order to have a comparison at the same power density. The tissue is considered 100 % necrotic when $\Omega(t) = 1$. From this figure it is evident that in most cases the values are very close. This means that pulsating heat allows to necrotize the same tumoral tissue of the non-pulsating heat source, but with lower maximum temperature, as shown before in Figs. 18 and 19.

Temperature differences between tissue and blood are displayed in Fig. 23, for pulsating and non-pulsating heating in all cases investigated. It can be noticed that for all the porosities and with reference to the smallest diameter here investigated d = 0.008 mm (Fig. 23 (a), (b) and (c)), differences between the two phases temperatures are negligible, so $T_t = T_b$. This because volumetric heat transfer coefficient becomes very high (see Table 6) due to the very small blood vessel diameter. In this case, local thermal equilibrium (LTE) hypothesis is verified.

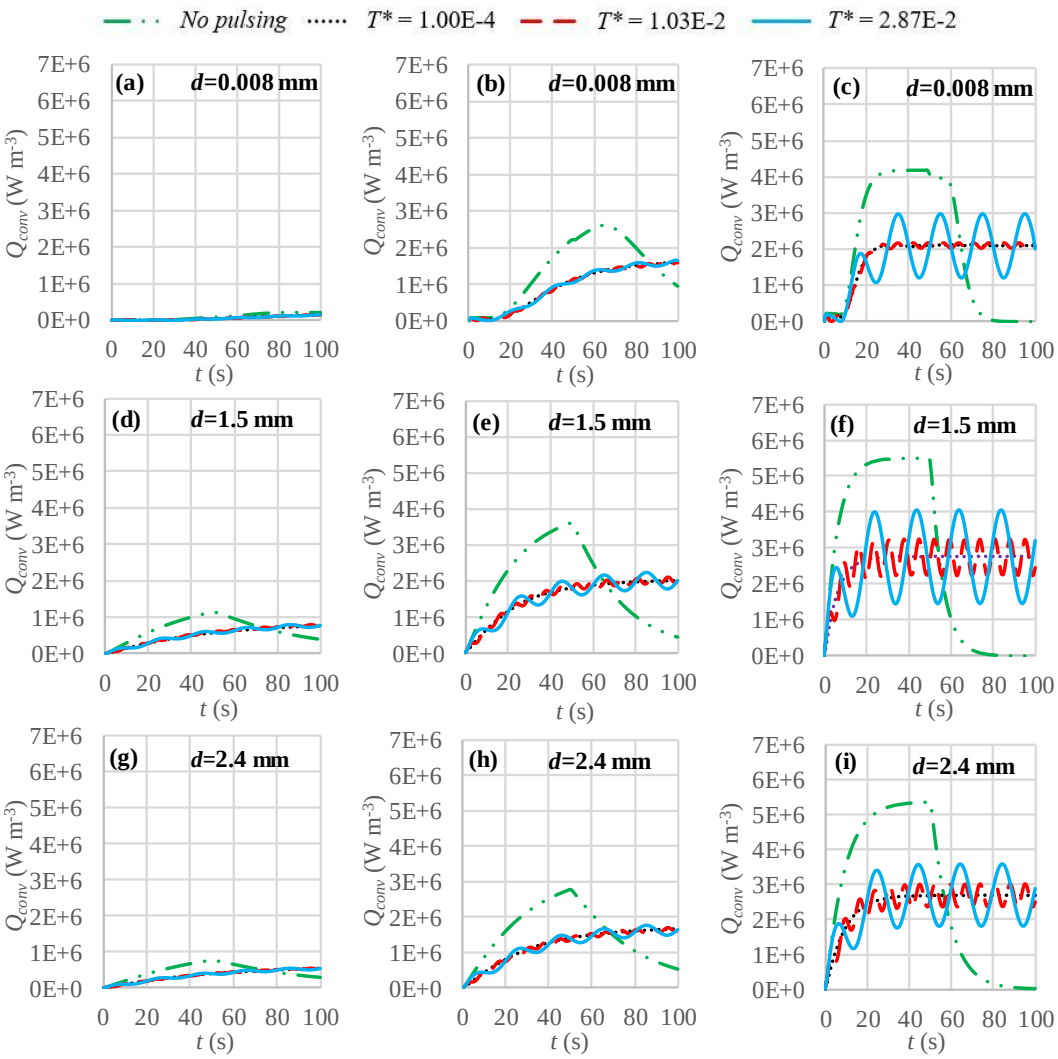

Figure 21. Convective power density distributions at the center of the sphere for pulsating and non-pulsating heating, when d=0.008 mm (capillaries), d=1.5 mm (secondary veins), and d=2.4 mm (main veins), for (a, d, g) ε=0.05, (b, e, h) ε=0.2 and (c, f, i) ε=0.6.

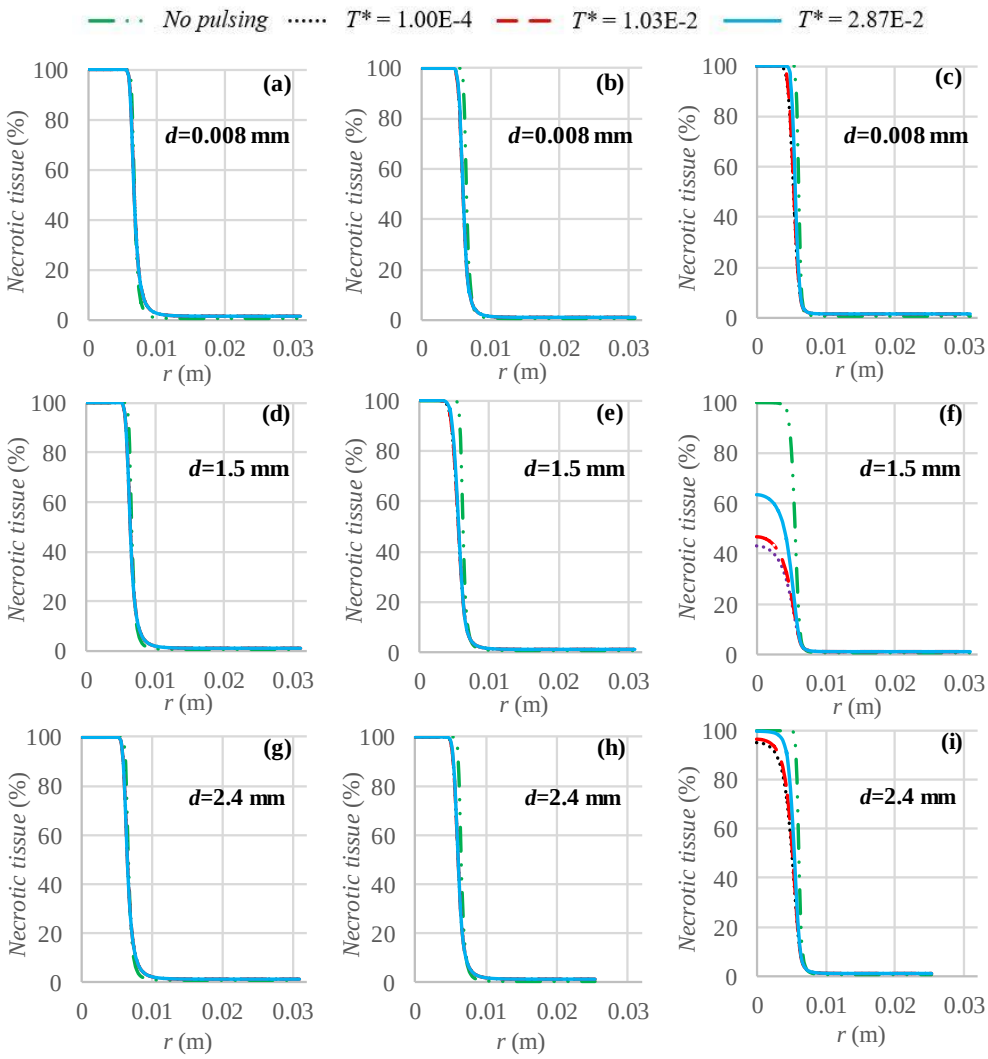

Figure 22. Percentage of necrotic tissue for pulsating and non-pulsating heating, when *d*=0.008 mm (capillaries), *d*=1.5 mm (secondary veins), and *d*=2.4 mm (main veins), for (a, d, g) ε=0.05, (b, e, h) ε=0.2 and (c, f, i) ε=0.6.

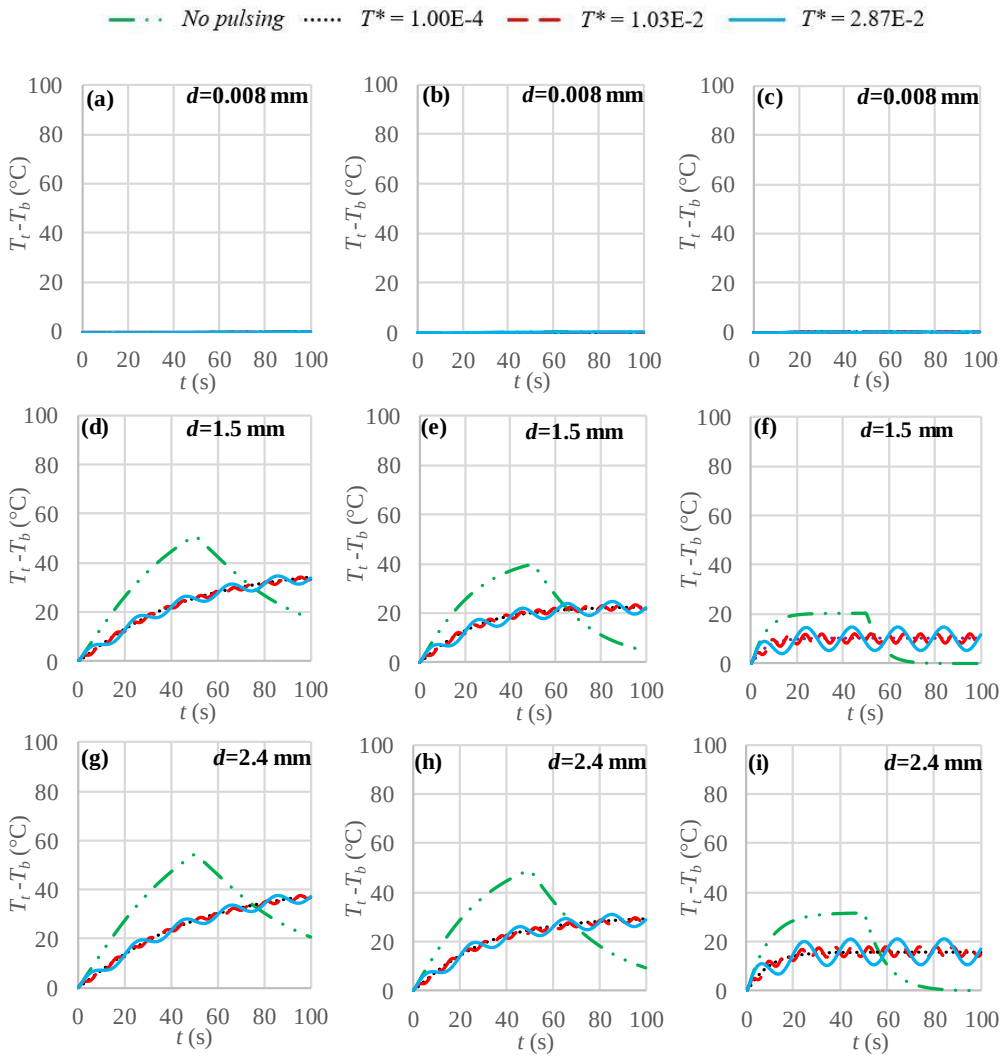

Figure 23. Differences between tissue and blood temperatures at the center of the sphere for pulsating and non-pulsating heating, when *d*=0.008 mm (capillaries), *d*=1.5 mm (secondary veins), and *d*=2.4 mm (main veins), for (a, d, g) ε=0.05, (b, e, h) ε=0.2 and (c, f, i) ε=0.6.

4.2. Pennes' bioheat equation vs. porous media approach in computer modeling of radiofrequency tumor ablation

4.2.1. Geometry and properties

The geometry of the model is shown Fig. 24, which includes an RF applicator (comprised of metal electrode and plastic handle) completely inserted in the hepatic tissue. The needle-like electrode has a conical tip, 30 mm long and 1.5 mm outer diameter, and an internal cooling circuit with cold saline. The axial symmetry means that a two-dimensional model could be implemented.

RFA is a monopolar procedure in which electrical current flows between the ablation electrode (see Fig. 24) and a large size dispersive electrode (in contact with the patient's skin). The RF generator frequency is 500 kHz, and the electric and thermal properties of the materials used in the models are shown in Table 8. Since the temperature dependence of thermal conductivity is very small this is considered constant.

Electrical conductivity in tissue and blood is defined as a temperature-dependent piecewise function to

consider the drastically reduced water content loss as temperature increases and vaporization occurs [119].

$$\sigma(T)=\begin{cases}0.19\cdot e^{0.015(T-37)} & 0\ °\mathrm{C}<T<99\ °\mathrm{C}\\ 0.19\cdot 2.5345 & 99\ °\mathrm{C}\le T\le 100\ °\mathrm{C}\\ 0.19\cdot(2.5345-0.50183(T-100)) & 100\ °\mathrm{C}<T\le 105\ °\mathrm{C}\\ 0.19\cdot 2.5345\cdot 10^{-2} & T>105\ °\mathrm{C}\end{cases} \tag{79}$$

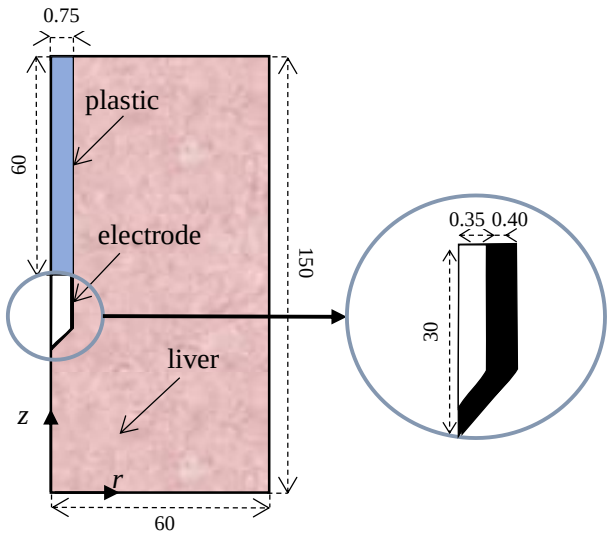

Figure 24. Two-dimensional axisymmetric model consisting of a fragment of liver tissue and an internally cooled electrode (out of scale, dimensions in mm).

Table 8. Properties of the materials modeled [120, 121, 122].

	ρ (kg·m^{-3})	c (J·kg^{-1}·K^{-1})	k (W·m^{-2}·K^{-1})	σ (S·m^{-1})
Liver	1080[a]	3455[a]	0.502	
	370[b]	2156[b]		See Eq. (1)
Blood	1000[a]	3639[a]		
	370[b]	2156[b]	0.502	
Electrode	8000	480	15	7.4×10^{6}
Plastic	70	1045	0.026	10^{-5}

[a]At temperatures below 100°C, and [b] above 100°C

4.2.2. Electrical problem equations

The heat source from RF power Q_{ext} (Joule losses) is given by:

$$Q_{ext}=\sigma|\mathbf{E}|^2 \tag{80}$$

where **E** is the electric field. $\mathbf{E}=-\nabla V$ is obtained from the governing equation of the electrical problem

$\nabla\cdot(\sigma(T)\nabla V=0)$, σ being the electrical conductivity and V the voltage.

A constant voltage is set on the ablation electrode during the entire protocol duration of 720 s except during roll-offs, when impedance rises by 30 Ω, in which case the standard roll-off protocol of switching off the applied voltage for 15 s is followed.

The three voltage values employed are 45 V, 65 V and 90 V. This choice covers the range from the highest roll-off avoidance value (45 V) to the highest standard protocol value used in clinical practice (90 V) [109].

For the electrical boundary conditions, an insulation electrical condition is applied to the contours of the tissue, except for top and bottom, which represent the dispersive electrode, where a condition $V = 0$ V is set.

4.2.3. Thermal problem equations

Three different bioheat models are implemented: the Pennes', LTNE and LTE. First, the issues common to all three models will be presented. Initial and boundary tissue temperature are 37°C. The thermal cooling effect inside the electrode is modeled by applying a convective heat flux (q_c) to the internal boundary of the electrode as follows:

$$q_c = h_r(T_r - T_t) \tag{81}$$

where h_r is the thermal convective coefficient (3127 W m^{-2} K^{-1}), Tt the tissue temperature and T_r the coolant temperature (5°C) as described in [109]. Thermal damage is computed using the Arrhenius model, in which tissue damage is increased with time of exposure, and it is obtained as follows from an exponential relationship between tissue exposure temperature, time and the kinetic parameters that account for morphologic changes in tissue relating to the thermal degradation of proteins [33]:

$$\Omega(t_{tot}) = \int_0^{t_{tot}} A e^{-\frac{\Delta H}{R_g T_t(t)}} dt \tag{82}$$

where A is the frequency factor (7.39×10^{39} s^{-1}), ΔH is the activation energy for the irreversible damage reaction (2.577×10^5 J mol^{-1}) [123], and R_g is the universal gas constant. The thermal damage contour is estimated using the isoline $\Omega = 4.6$, which encompasses the zone with 99% cell death probability.

<u>4.2.3.1 Modified Pennes' equation</u>

Pennes' bioheat model is starting point for the comparison of the models, based on the following equation:

$$(\rho c)_t \frac{\partial T_t}{\partial t} = \nabla\cdot(k_t \nabla T_t) + Q_{perf} + Q_{met} + Q_{ext} \tag{83}$$

where subscript t refers to the tissue, ρ_t is density, c_t the specific heat, k_t the thermal conductivity, T_t the temperature, t the time, Q_{perf} the blood perfusion term, Q_{met} metabolic heat source (which is neglected in RFA applications [109]) and Q_{ext} is the external RF power density imposed to the tissue during RF power application (see Eq. (80)). To introduce vaporization into the Pennes' equation, one alternative is to follow the enthalpy method as described in [120], so that the term ($\rho_t c_t$) in Eq. (83) becomes:

$$(\rho c)_t = \begin{cases} (\rho_l c_l)_t & 0\ °\text{C} < T_t \leq 99\ °\text{C} \\ \dfrac{h_{fg} C_{w,t}}{100\ °\text{C} - 99\ °\text{C}} & 99\ °\text{C} < T_t \leq 100\ °\text{C} \\ \rho_g c_g & T_t > 100\ °\text{C} \end{cases} \tag{84}$$

where ρ_l and c_l are density and specific heat of tissue at temperature below 100°C (liquid phase), ρ_g and c_g are density and specific heat of tissue at temperature above 100°C (gas phase), h_{fg} is the product of water latent heat of vaporization and water density at 100°C ($2.17 \cdot 10^9$ J m^{-3}), and $C_{w,t}$ is the water content inside the liver tissue (68%) [121]. Furthermore, Q_{perf} in Eq. (83) is defined as follows:

$$Q_{perf} = \beta_d \rho_b c_b \omega_b (T_b - T_t) \tag{85}$$

where ρ_b and c_b are the density and specific heat of blood respectively, ω_b is blood perfusion coefficient (0.019 s^{-1}) [124], T_b is blood temperature (which is assumed to be constant throughout the tissue and taken as body temperature of 37°C in Pennes' model), and β_d is a coefficient that is 0 or 1 depending on the value of thermal damage function Ω (see Eq. (82)), so, $\beta_d = 0$ for $\Omega \geq 4.6$ and $\beta_d = 1$ for $\Omega < 4.6$.

4.2.3.2 Modified LTNE model

The second model is based on a modified form of the Local Thermal Non-Equilibrium equations, first developed in 1997 by Xuan and Roetzel[48] to model heat transfer in a porous medium. As previously described, the entire biological medium is divided into two distinct phases: the tissue phase, which is the solid part, made up of cells and interstitial spaces, and the blood phase, which is the fluid part, represented by the blood flowing through the solid phase. We thus have two energy equations for this model, slightly different from Eqs. (37) and (38), one for the tissue temperature (T_t):

$$(1-\varepsilon)(\rho c)_t \frac{\partial \langle T_t \rangle}{\partial t} = (1-\varepsilon) k_t \nabla^2 \langle T_t \rangle - ha\left(\langle T_t \rangle - \langle T_b \rangle\right) + \beta_d \rho_b c_b \omega(\langle T_b \rangle - \langle T_t \rangle) + (1-\varepsilon) Q_{ext} \tag{86}$$

and one for the blood temperature (T_b):

$$\varepsilon(\rho c)_b\left(\frac{\partial\langle T_b\rangle}{\partial t}+\beta\langle\mathbf{u}\rangle\cdot\nabla\langle T_b\rangle\right)=\varepsilon k_b\nabla^2\langle T_b\rangle+ha\left(\langle T_t\rangle-\langle T_b\rangle\right)+\beta_d\rho_b c_b\omega(\langle T_t\rangle-\langle T_b\rangle)+\varepsilon Q_{ext} \tag{87}$$

The second terms on the right side of Eqs. (86) and (87) describe the interfacial convective heat transfer between blood and tissue phases across the vascular wall as defined by Newton's cooling law. Note that the Pennes' model does not consider any advective term such as the second term on the left side of Eq. (87), but an overall blood perfusion term as a heat sink for tissue. The LTE and LTNE models split the Pennes' equation perfusion term into a modified perfusion term and a convective term [51]. The modified perfusion term in the porous media-based models (third term on the right side of Eqs. (86) and (87)) differs from Eq. (85) for the value of the perfusion coefficient ω, which is ω = 0.0005 s^{-1}, instead of ω_b = 0.019 s^{-1}, to consider the modification described above. In fact, Pennes obtained this coefficient for the volume flow of blood through tissue by fitting his model with experiments. He specified that 0.0005 s^{-1} is the most suitable value when the balance between blood and tissue is incomplete. Nakayama *et al.* also used this value in their work on LTNE equations [51].

The volume averaging technique is employed to consider the volume average quantities of the variables [71], so that the symbol <> refers to the average volume of a generic variable and is neglected from this point onwards. In the LTNE model, the most important modifications regard the phase change and blood velocity. In fact, the phase change is considered separately in both phases, while vaporization only refers to water in the tissue in the Pennes' model (see Eq. (84)). Vaporization is thus included as in Eq. (84) for the tissue phase, while for the blood phase we have:

$$(\rho c)_b=\begin{cases}(\rho_l c_l)_b & 0\ °\mathrm{C}<T_b\le 99\ °\mathrm{C}\\ \dfrac{h_{fg}C_{w,b}}{(100\ °\mathrm{C}-99\ °\mathrm{C})} & 99\ °\mathrm{C}<T_b\le 100\ °\mathrm{C}\\ \rho_g c_g & T_b>100\ °\mathrm{C}\end{cases} \tag{88}$$

In this way the evaporation of water in blood is included, choosing the value of water content in blood $C_{w,b}$ = 79% as in [125]. Four different blood velocity directions were considered to simulate a more realistic vascular network and the initial values were the same in all four directions $u_z = u_{-z} = u_r = u_{-r}$, where directions z and r are specified in Fig. 24. As for blood perfusion, blood velocity is considered zero when cell death probability was 99% according to the β_d coefficient. Terminal artery blood velocity was chosen following the experimental values reported in Crezee and Lagendijk [88], a reasonable choice according to Chen and Holmes' LTNE model [42], in which blood heat exchange is assumed to occur only downstream of the terminal arteries before the arterioles. Blood velocity value is thus assumed reasonably to be 0.4 cm·s^{-1}, with a blood vessel diameter d = 0.03 mm. Furthermore, four different porosity values are considered, ε: 0.2, 0.3, 0.4 and 0.6 to employ the liver values given in clinical and numerical studies in the literature [80, 126-129]. These, in fact, show wide dispersity because of the different assessment methods considered

[126, 128]. The interfacial heat transfer coefficient h is 170 $W \cdot m^{-2} \cdot K^{-1}$, as in Yuan [72], based on experimental measurements. Table 9 summarizes the specific surface areas a and volumetric convective coefficients $h_v = ha$ for all the cases considered.

Table 9. Volumetric transfer areas and volumetric heat transfer coefficients considered in LTNE.

a (m^{-1})				h_v ($W \cdot m^{-3} \cdot K^{-1}$)			
$\varepsilon = 0.2$	$\varepsilon = 0.3$	$\varepsilon = 0.4$	$\varepsilon = 0.6$	$\varepsilon = 0.2$	$\varepsilon = 0.3$	$\varepsilon = 0.4$	$\varepsilon = 0.6$
26667	40000	53333	80000	4.53E6	6.80E6	9.07E6	1.36E7

a: volumetric transfer area; hv: volumetric heat transfer coefficient

4.2.3.3 Modified LTE model

The LTNE model described above considers the blood phase and the tissue phase at two distinct temperatures (i.e., $T_t \neq T_b$). However, when the local thermal equilibrium hypothesis is maintained, tissue and blood are really at the same temperature, so that $T_t = T_b = T$ and Eqs. (86) and (87) can be combined in a single equation as follows:

$$\left[(1-\varepsilon)(\rho c)_t + \varepsilon(\rho c)_b\right]\frac{\partial T}{\partial t} + \varepsilon(\rho c)_b \beta \cdot \mathbf{u} \cdot \nabla T = \left[(1-\varepsilon)k_t + \varepsilon k_b\right]\nabla^2 T + Q_{ext} \tag{89}$$

In this model the heat sink effect for tissue is only represented by the advective term related to the blood velocity. In fact, when Eqs. (86) and (87) are combined the perfusion term disappeared. Note that in this case local thermal equilibrium should be a good approximation for temperature distributions because of the small size of the vessels considered (as described in [50, 121, 130]), while this assumption would not be valid in the presence of larger vessels. Even if the two phases are at the same temperature, they have different water contents, as in the LTNE model, so that vaporization was included as in Eqs. (84) and (88) by considering $T_t = T_b = T$. The assumptions on blood velocity for LTNE are also valid for this model.

4.2.4. Numerical approach and validation

The three models are numerically solved with the software Comsol Multiphysics (Burlington, MA, USA). A triangular mesh is employed with a finer size on the boundary between electrode and tissue domains as in [109], where the highest temperature gradients take place. The grid convergence is verified on the maximum tissue temperature ($T_{t,max}$) obtained at first roll-off time. When the difference between simulations is less than 0.5% in $T_{t,max}$ former mesh size is considered as appropriate. A similar convergence test is employed to estimate the optimal outer dimensions. The PARDISO direct solver is used with the implicit intermediate Backward Differentiation Formulas (BDF) time stepping method, where the intermediate configuration is chosen to fix the initial and maximum steps of the solver, in this case 0.01 s and 1 s, respectively.

As regards the comparison of our computer results with *in vivo* experimental studies in the literature,

Goldberg *et al* [105] reported a coagulation diameter of 3.7 ± 0.6 cm for a pulsed protocol similar to the 90 V case. This value agrees with the results from the LTE and LTNE models with ε = 0.3 (which is the most realistic published values [126-128, 131]), i.e., 3.42 cm and 3.47 cm, respectively. Note that the exact protocol is unknown for the specific case, but the predominant current peak of about 1600 mA is comparable with the 1500 mA predominant peak obtained in our case. Although these differences could slightly affect the results, they did not affect the overall comparison of all the models.

Figure 25 compared tissue temperature evolution at 10 and 20 mm from the electrode between the experimental results in [105] and the three bioheat models: Pennes' equation, LTE model with ε= 0.3, and LTNE model with ε= 0.3, respectively.

It can be seen that the temperature difference between the porous media-based models and the experimental data are ~4°C and 2°C at 10 mm and 20 mm, respectively. However, the slightly higher predominant current peak could partially justify this difference. At 10 mm the temperature differences between the two porous media-based models and Pennes' equation are only about 2°C, mostly in the last 200 s, so the three bioheat models come reasonably close to the experimental data. However, at 20 mm, the differences between both the LTE and LTNE models and Pennes' equation are ~8 °C, which justifies the difference of about 1 cm in the final coagulation diameters obtained and suggests that the porous media-based models could be more accurate than Pennes' in this case of very similar protocol. The LTE and LTNE model results confirmed that the thermal local equilibrium is maintained in this case, as explained previously, so that they also give very similar outcomes in terms of tissue temperature.

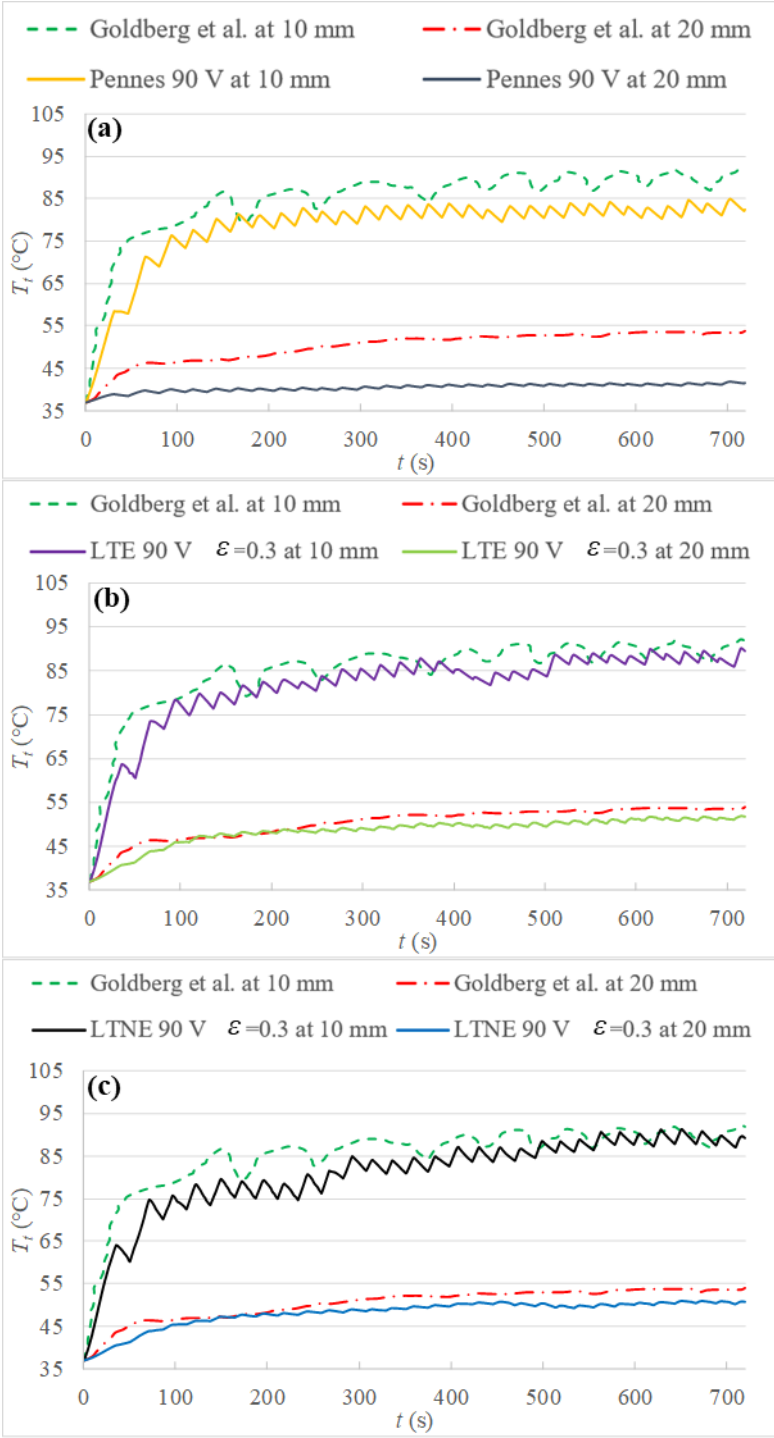

Figure 25. Temperature profiles for (a) Pennes' equation, (b) LTE equation with ε = 0.3, (c) LTNE equations with ε = 0.3, and in vivo experimental results obtained by Goldberg et al. [105]

4.2.5. Results

The results are given in terms of the minor diameter of coagulation zones d_c (transverse diameter to the applicator shaft in r direction in Figs. 26 and 27), total energy delivered during the application E_{RF}, maximum tissue temperature reached $T_{t,\max}$, total time in which the generator is "on" (t_{on}), time of first roll-off ($t_{roll\text{-}off}$) and number of roll-offs $N_{roll\text{-}off}$, distinguishing between the Pennes', LTNE and LTE results with

four different porosity values.

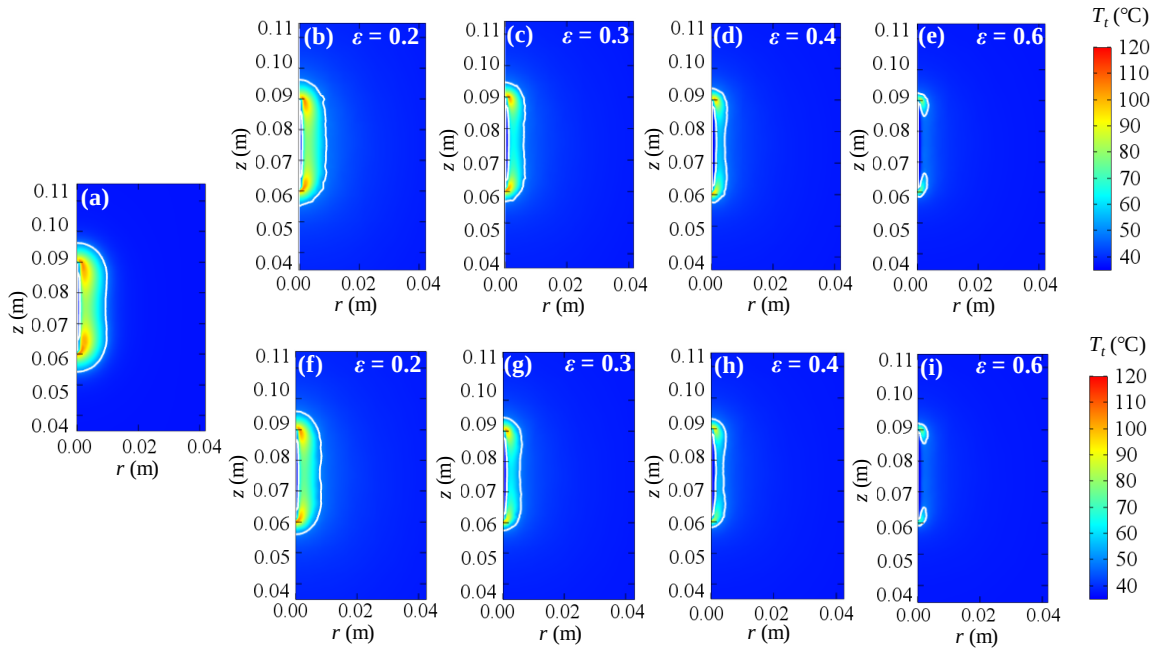

Figure 26. Tissue temperature distributions after 720 s of applying 45 V computed from Pennes' bioheat model (a), LTE model (b-e), and LTNE model (f-i) for different porosity values (ε). White line represents coagulation zone contour.

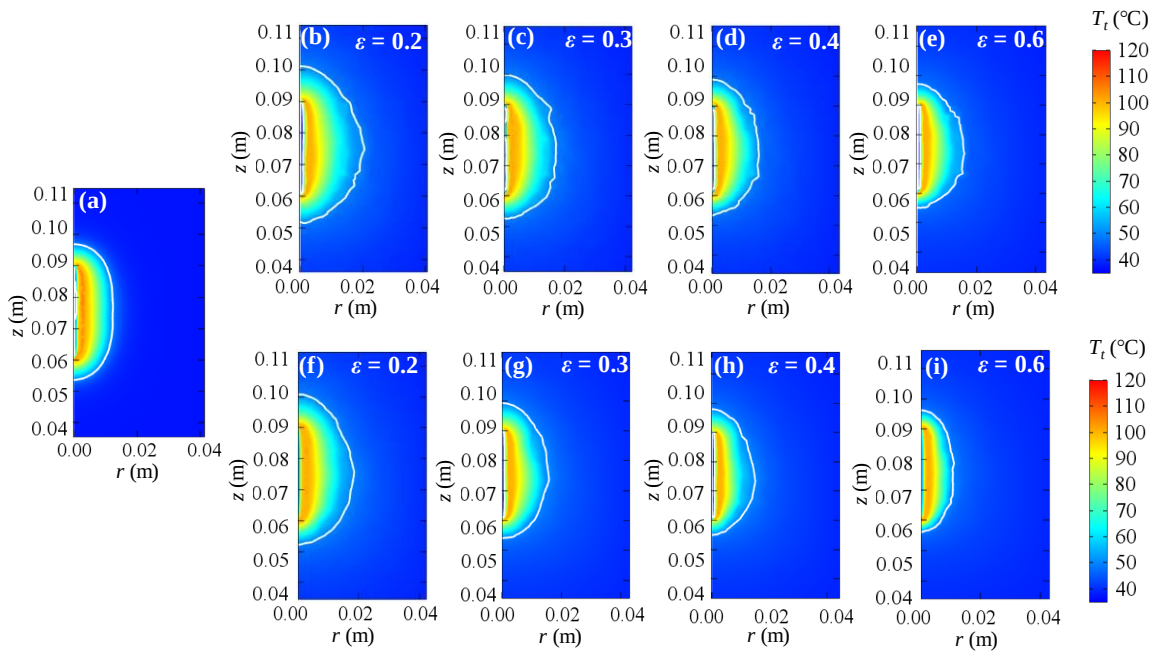

Figure 27. Tissue temperature distributions after 720 s of applying 65 V computed from Pennes' bioheat model (a), LTE model (b-e), and LTNE model (f-i) for different porosities (ε). White line represents coagulation zone contour.

All the models employed are compared at voltage values of 45, 65 and 90 V for 720 s. As expected, only

in the 45 V case the absence of roll-offs allows RF power to be applied continuously for the entire 720 s. When roll-offs occur at 65 and 90 V the pulsing protocol is activated [109].

Table 10 shows the results of the 45 V simulations. The first finding is that the coagulation diameters computed from the LTE and LTNE models are smaller than those from the Pennes' model for all porosity values.

Table 10. 45 V RFA results computed for different bioheat models (Pennes', Local Thermal Equilibrium, Local Thermal Non-Equilibrium) and porosity values.

Model	ε	d_c(cm)	E_{RF}(kJ)	t_{on} (s)	$t_{roll\text{-}off}$(s)	$N_{roll\text{-}off}$	$T_{t,\max}$ (°C)
Pennes	-	1.94	19.7	720	-	-	106
LTE	0.2	1.81	19.5	720	-	-	106
	0.3	1.30	18.6	720	-	-	105
	0.4	1.01	17.7	720	-	-	101
	0.6	0.70	16.7	720	-	-	87
LTNE	0.2	1.69	19.4	720	-	-	105
	0.3	1.23	18.2	720	-	-	103
	0.4	0.94	17.4	720	-	-	94
	0.6	0.65	16.5	720	-	-	81

d_c: coagulation diameter; E_{RF}: applied RF energy; t_{on}: total time generator is "on"; $t_{roll\text{-}off}$: time of first roll-off; $N_{roll\text{-}off}$: number of roll-offs.

For instance, the difference between Pennes' and LTE ranges from only 1.3 mm for ε = 0.2 to 12.4 mm for ε = 0.6. The coagulation diameter reduces dramatically as porosity increases (from 0.2 to 0.6) and the value of the maximum temperature in tissue also drops. In fact, the higher the porosity, the larger the convective contribution of the mass blood flux.

At lower temperatures electrical conductivity increases less, so impedance (Z) decreases less, and RF applied power decreases too ($P = V^2/Z$). This is confirmed by the reduced energy (~19.5 kJ to 16.5 kJ when porosity rises from 0.2 to 0.6). This highlights the importance of considering the blood volume fraction, (i.e., porosity) in bioheat thermal ablation models. The porosity of different organs ranges from negligible values such as the brain (0.03 to 0.05) to very high as in liver (about 0.3) and kidney (about 0.35) [79, 129, 132-136].

The same organ can have different porosities in different physiological conditions, as happens for example in chronic liver hepatitis and cirrhosis, when porosity can be less than 0.2 [126].

Figure 26 shows temperature distributions and coagulation contours at 45 V and 720 s computed from the Pennes', LTE and LTNE models, respectively. The mean temperature dropped in the domain as porosity increased.

The results of the LTE and LTNE models at the same porosity value are almost identical. As all the cases referred to a tissue with infiltrating terminal arteries, as described in Section 4.2.3.2, the values of blood vessel diameter and blood velocity in the LTNE model were small enough to validate the local thermal

equilibrium assumption, in agreement with the results reported in [50, 72, 137], which all confirmed that the LTE temperature distributions agree with those of LTNE only when small blood vessels are considered (up to 0.03 mm) and blood velocity is less than 0.4 cm s^{-1}, showing that blood does not act as a heat sink in these cases. Note that the LTNE and LTE equations are not limited to model vessels smaller than 1 mm, but can also model larger vessels, which were not considered in this work.

Tables 11 and 12 show the results for 65 and 90 V, respectively. Unlike 45 V, the coagulation diameters computed from the LTE and LTNE models with 65 and 90 V at all porosity values are greater than those from the Pennes' model, except for LTNE $\varepsilon = 0.6$. This can be explained by their different ways of applying power: at 45 V it is continuous for 720 s, so that the only physical phenomenon that affects coagulation zone size is the larger heat loss through blood as porosity increased, which also mean less energy delivered in the LTNE and LTE models. Instead, the higher voltage values involving alternating periods of rising (power on) and falling (power off) temperatures weigh on the different thermal inertia of the models. In fact, unlike Pennes' equation, they consider solid and fluid phases separately at different temperatures and water contents. This results in a better heat storage capability in the "off" periods, which becomes determinant in achieving necrosis, especially away from the electrode, and so it produces greater final coagulation diameters. This can also be seen in Figure 25 concerning the comparison with experimental results.

As for 45 V, at these voltages the larger the porosity (from 0.2 to 0.6), the smaller the coagulation diameter (from 4.09 to 3.17 cm for LTE and 3.72 to 2.23 cm for LTNE at 65 V, from 4.13 to 3.16 cm for LTE and 3.94 to 2.62 cm for LTNE at 90 V).

Interestingly, the smaller diameter is associated with a slight increase in delivered energy: from 28.6 to 32.1 kJ for LTE and from 31.2 to 34.2 kJ for LTNE at 65 V, and 33.8 to 36.2 kJ for LTE and 38.1 to 39.8 kJ for LTNE at 90 V. This is probably due to roll-offs again, involving different thermal inertia in the LTE and LTNE models.

Table 11. Results for different bioheat models at 65 V.

Model	ε	d_c(cm)	E_{RF} (kJ)	t_{on} (s)	$t_{roll\text{-}off}$(s)	$N_{roll\text{-}off}$	$T_{t,\max}$ (°C)
Pennes	-	2.47	30.7	494	126	16	114
LTE	0.2	4.09	28.6	437	127	19	113
	0.3	3.46	30.2	464	135	18	112
	0.4	3.21	30.3	475	151	17	112
	0.6	3.17	32.1	514	178	14	112
LTNE	0.2	3.72	31.2	480	131	16	113
	0.3	3.17	31.8	495	145	15	112
	0.4	3.02	32.2	511	164	14	113
	0.6	2.23	34.2	555	209	11	113

d_c: coagulation diameter; E_{RF}: applied RF energy; t_{on}: total time generator is "on"; $t_{roll\text{-}off}$: time at first roll-off; $N_{roll\text{-}off}$: number of roll-offs.

Table 12. Results for different bioheat models at 90 V.

Model	ε	d_c(cm)	E_{RF} (kJ)	t_{on} (s)	$t_{roll\text{-}off}$(s)	$N_{roll\text{-}off}$	$T_{t,\max}$ (°C)
Pennes	-	2.50	36.5	270	31	30	119
LTE	0.2	4.13	33.8	239	31	32	118
	0.3	3.42	34.9	251	35	32	119
	0.4	3.28	35.3	254	36	31	118
	0.6	3.16	36.2	270	38	30	119
LTNE	0.2	3.94	38.1	270	34	30	118
	0.3	3.47	38.8	281	35	30	120
	0.4	2.99	38.6	286	36	29	117
	0.6	2.62	39.8	300	40	28	118

d_c: coagulation diameter; E_{RF}: applied RF energy; t_{on}: total time generator is "on"; $t_{roll\text{-}off}$: time at first roll-off; $N_{roll\text{-}off}$: number of roll-offs.

When porosity is increased, the larger blood volume removes heat from the tissue more effectively, which simultaneously delays roll-off, i.e., power can be applied longer (higher values of t_{on}), requiring slightly higher power in LTE and LTNE. The maximum tissue temperature is quite similar in all cases at the same voltage level (~114 ºC for 65 V and ~120 ºC for 90 V) because in all cases the on-off periods avoid the temperature rising above the limit value. When the LTE and LTNE models are compared at the same porosity value, the LTNE coagulation diameters are similar to or even smaller, with longer t_{on} and higher energy, possibly because of the effect of vaporization at different temperatures for tissue and blood, which is more significant for these applications than at 45 V. For the same bioheat model, the results obtained at the two different voltage levels are almost identical, (differences in coagulation diameter from 0.01 cm to 0.07 cm in LTE and from 0.03 to 0.39 cm for LTNE), which suggests that 65 V is enough to obtain maximum coagulation diameter after 12 min.

Figure 27 shows temperature distributions and coagulation contours at 65 V and 720 s computed from the Pennes', LTE and LTNE models, respectively. Comparing Figures 27 and 28 shows the different coagulation shapes at voltages higher than 45 V. In fact, at 65 V the zones are more spherical for both the LTE and LTNE models than Pennes', especially at low porosities.

Figure 28 summarizes the coagulation zone diameters computed from the three bioheat models at different porosities (models based on porous media approach).

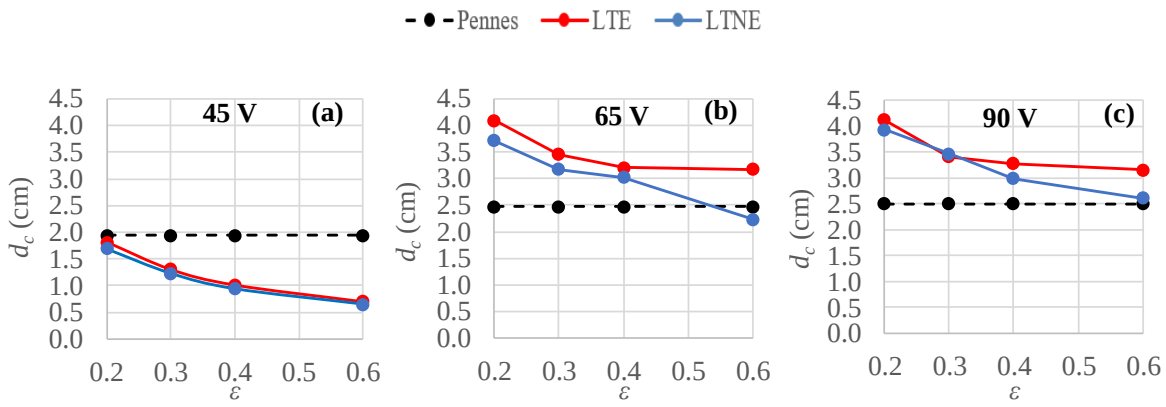

Figure 28. Transverse diameters of coagulation zone (d_c) computed after 720 s of RFA for the three considered bioheat models (Pennes', LTE and LTNE) at different porosity values (ε) and applied voltages: 45 V (a), 65 V (b) and 90 V (c).

As highlighted in Figs. 26–28, the differences in terms of coagulation diameters and temperature distributions could differ significantly or not at all between the porous media-based and Pennes' models, according to applied voltage and porosity. For instance, at 45 V, Pennes' provides the same result as LTE and LTNE for $\varepsilon = 0.2$. In fact, the range of differences in coagulation diameters obtained is from only 1 mm at 45 V and LTE $\varepsilon = 0.2$ to about 1.60 cm for the highest voltage applied and LTE $\varepsilon = 0.2$. These differences could play a relevant role in predicting coagulation zones, since the risk could be either incomplete ablation and tumor recurrence or overestimating the ablated area and healthy tissue necrosis.

4.3. Numerical analysis of radiofrequency ablation in a tumor tissue bounded by healthy tissue

In radiofrequency ablation (RFA) modelling, geometry and thermophysical properties play a key role. Thermal and electrical properties vary with temperature, and they depend on the organ considered [137], and on its condition (tumoral or healthy) [138]. A review about functions proposed to consider temperature dependence of such properties has been presented by Trujillo and Berjano [139], showing that results are not significantly affected by the kind of function employed. Haemmerich et al. [140] found that electrical conductivity of tumour tissue can be about two times than that of healthy tissue. Similar differences can be found in Zhang et al. [110], where also thermal conductivity at 21 °C for liver tumour is about 20% higher than that of a healthy liver. A study that considers two different layers of tissue, i.e., tumour tissue and healthy, has been already proposed by Rattanadecho and Keangin [80] with references to *ex vivo* microwave ablation. They modelled tissues as porous layers under the assumption of local thermal non equilibrium with different properties depending on if tissue is healthy or not, without including vaporization of water in the two phases. In this paragraph, a porous media model for heat transfer predictions in RFA for in vivo liver tissue is presented. The objective is to assess how important is to consider separately tumour and healthy tissue in such problems. Governing equations are developed with references to the porous media theory under the assumption of local thermal non-equilibrium, while vaporization is considered with the effective heat capacity method. Two geometries are compared: a

healthy liver tissue and a tumoral tissue bounded by a healthy tissue. Results are developed by considering different electrical and thermal properties for tumoral and healthy tissue, and properties variation with temperature is also considered.

4.3.1. Mathematical model

RFA of liver tissue is numerically simulated considering two scenarios: a homogeneous healthy tissue and a spherical tumour bounded by healthy tissue. The geometry of the problem is shown in Figure 29, in which it can be recognized the RF applicator with a 1.5 mm diameter active electrode and a plastic handle.

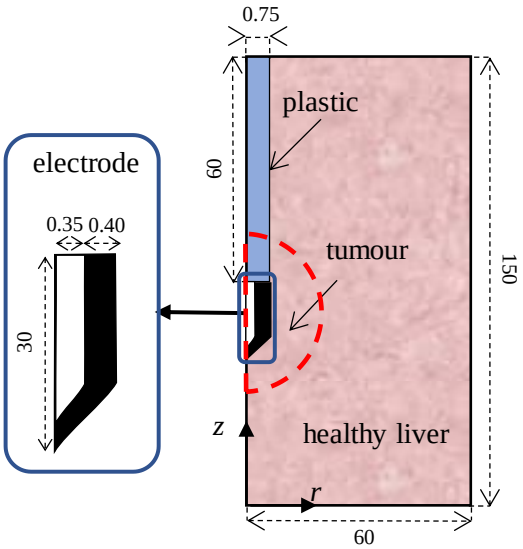

Figure 29. Geometry of the model, which consists of a cooled electrode applied on healthy liver tissue and tumoral tissue bounded by healthy tissue. (out of scale, dimensions in mm).

An internally cooled 3-cm electrode is completely inserted in the hepatic tissue. As regards the tumoral tissue, a 2 cm radius spherical tumour is considered. The problem has axial-symmetry, so it is possible to implement a 2D axisymmetric model in order to minimize computing time. The heating in tissue domain is modelled with the porous media theory, and a modified Local Thermal Non-Equilibrium bioheat model is used for the energy equations, thus two different equations are implemented for the extra-vascular and vascular regions as described in paragraph 4.2.3.2, by Eqs. (86) and (87). Moreover, the assumptions done for the model described previously in paragraph 4.2 are the same, except the properties used in the different domains, as shown in Table 13. To notice that the LTNE equations are modified to include the water content vaporization in both liver tumoral tissue and blood separately, by following the enthalpy method described by Abraham and Sparrow [120], as previously reported in Eqs. (84) and (88) for tissue phase and blood phase respectively, where C_w is the water content inside the tumoral liver tissue (81%) or in the blood (79%) as found in literature [125, 141].

Table 13. Characteristics of the materials employed in the model [109, 110, 140].

	ρ (kg·m^{-3})	c (J·kg^{-1}·K^{-1})	k (W·m^{-2}·K^{-1})	σ(37°C) (S·m^{-1})
Healthy liver	1080[a]	3455[a]	0.502	0.19
	370[b]	2156[b]		
Tumour	1045[a]	3760[a]	0.600	0.45
	370[b]	2156[b]		
Blood	1000[a]	3639[a]	0.502	
	370[b]	2156[b]		
Electrode	8000	480	15	7.4 x 10^{6}
Plastic	70	1045	0.026	10^{-5}

[a] at temperature below 100°C, [b] at temperature above 100°C

In this work, the values of the electrical conductivity of both healthy and tumoral liver tissue evaluated at 37°C are taken from literature [109, 140], and their values are 0.19 (S m^{-1}) and 0.45 (S m^{-1}) respectively. So, according to Eq. (90), in Figure 30 the different electrical conductivity profiles of both healthy and tumoral tissue are shown.

$$\sigma(T)=\begin{cases}\sigma(37°\mathrm{C})\cdot e^{0.015(T-37)} & 0°\mathrm{C}<T<99°\mathrm{C}\\ \sigma(37°\mathrm{C})\cdot 2.5345 & 99°\mathrm{C}\le T\le 100°\mathrm{C}\\ \sigma(37°\mathrm{C})\cdot(2.5345-0.50183(T-100)) & 100°\mathrm{C}<T\le 105°\mathrm{C}\\ \sigma(37°\mathrm{C})\cdot 2.5345\cdot 10^{-2} & T>105°\mathrm{C}\end{cases} \tag{90}$$

In addition, two different voltages (45 and 65 V) are here employed. This choice is due to consider the highest value which avoids the roll-off phenomenon (45 V), and the value which causes the highest coagulation diameter. Roll-off happens when impedance increases significantly since the tissue around the electrodes becomes completely dehydrated [109]. In this case it is set that the roll-off happens when impedance becomes 30 Ω higher than the initial one. Furthermore, the experimental protocol in which the applied voltage is switched off for 15 s when the roll-off happens is applied.

As regards the initial and boundary conditions of the problem, tissue and blood temperatures considered are 37°C. The thermal cooling effect inside the electrode is modelled by applying a convective heat flux (q_c) to the internal boundary of the electrode as previously seen in paragraph 4.3.2. in Eq. (81).

Furthermore, an insulation electrical condition is set to the contours of tissue, except at the bottom and top contours, which represent the dispersive electrode, where a condition V = 0 V is employed. Governing equations are numerically solved with the finite element commercial code COMSOL Multiphysics (Burlington, MA, USA). A triangular mesh made up by 2509 elements is used with a finer size on the boundary between electrode and tissue domains as in [109], where the higher temperature gradients take place. PARDISO direct solver is employed to solve the equations, the time stepping method is the intermediate backward differentiation formulas (BDF) with initial and maximum steps of 0.01 s and 1 s, respectively. Furthermore, for each time step the absolute tolerance is set equal to 10^{-3}.

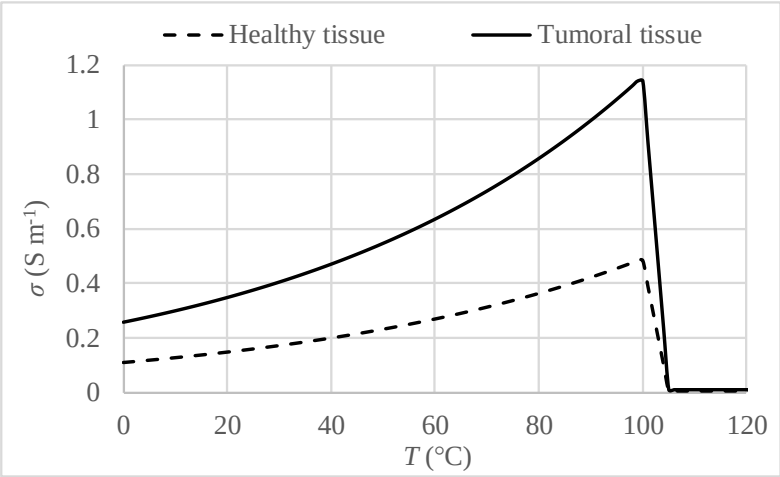

Figure 30. Temperature-dependent electrical conductivity of both healthy and tumoral tissue.

4.3.2. Results

The results are shown in Table 14 in terms of the coagulation zones transverse diameters d_c (in r direction of the following Figure 32), total energy delivered during the application (E_{RF}), maximum tissue temperature reached ($T_{t,max}$), total time in which the generator is "on" ($t_{tot,on}$), time of first roll-off ($t_{roll\text{-}off}$) and number of roll-off ($N_{roll\text{-}off}$).

Table 14. Results with and without tumoral tissue for 45 V and 65 V.

45 V	d_c (cm)	E_{RF} (kJ)	t_{on} (s)	$t_{roll\text{-}off}$ (s)	$N_{roll\text{-}off}$	$T_{t,max}$ (°C)
Healthy liver	1.23	18.2	720	-	-	103
Healthy liver and tumour	3.40	34.8	720	-	-	105
65 V	d_c (cm)	E_{RF} (kJ)	t_{on} (s)	$t_{roll\text{-}off}$ (s)	$N_{roll\text{-}off}$	$T_{t,max}$ (°C)
Healthy liver	3.17	31.8	495	145	15	112
Healthy liver and tumour	4.26	50.2	460	117	18	117

The first outcome for both the cases is the prominent increase of the coagulation diameter when the spherical tumour is included in the model. In fact, the higher electrical conductivity of tumour gives higher energy Q_{ext} from Eq. (80). Distinguishing the 45 V and 65 V cases, the coagulation diameter increases of 2.17 cm and 1.09 cm respectively, so the effect is most evident with lower voltage. Focusing on the 65 V application, when the tumour is considered, the appearance of the first roll-off is advanced 28 s, so the total time during which the generator is applying power is 35 s smaller, nevertheless, the resulting energy delivered is 58% higher. All the results obtained from Table 14 are highlighted in Figure 31. As regards the tissue temperature, while the peak is similar comparing the models (with healthy tissue and the tumoral one), the temperature distribution changes drastically when 45 V is applied, as shown in Figure 32. In fact, the tumoral tissue entails higher mean temperatures inside the coagulation zone. Consequently, the higher mean temperatures reached

in the tumoral tissue cause larger coagulation zones and this is the key point of our results.

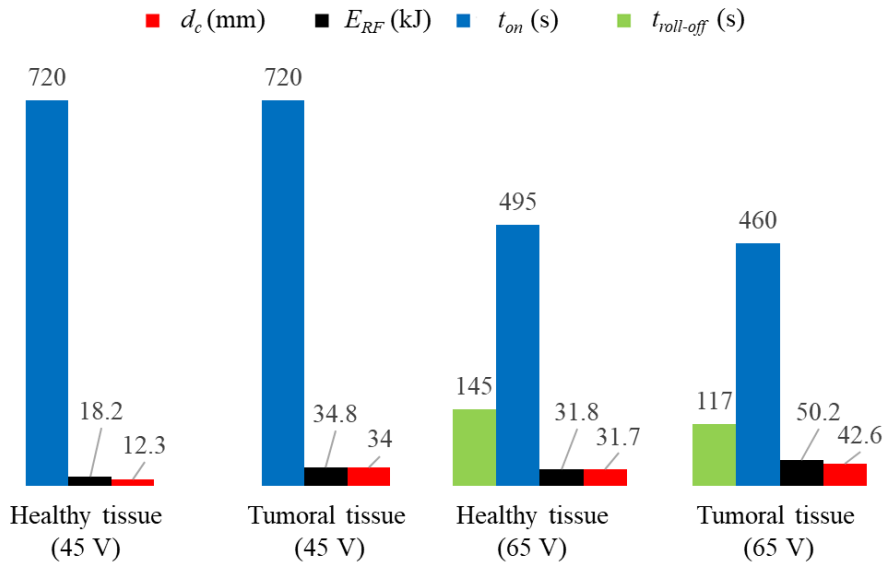

Figure 31. Coagulation diameters, total energy, total time of applied power and time of first roll-off after 45 V and 65 V applied for healthy liver and tumoral hepatic tissue bounded by healthy liver.

Figure 32 also shows that the spherical 2 cm tumour cannot be completely ablated performing 45 V RFA, so the risk of incomplete ablation and tumour recurrence is very high. Moreover, as regards the 65 V case, while the mean temperature distribution is higher when the tumoral tissue is included, the differences are not so relevant as in 45 V case. However, the spherical 2 cm tumour can be completely ablated in this case, avoiding the risk of tumour recurrence.

Furthermore, it is interesting to display the tissue temperature evolution during the heating time in three different points along the *r* direction, in correspondence with the center of the electrode (z = 0.075 m). In Figure 33 tissue temperature profiles for 45 V is shown at 0.25 cm, 1 cm, and 2 cm far from the electrode. From Figure 33 it is highlighted the drastic temperature increase when the tumoral tissue is included in the domain. At the end of the application at 2 cm far from the electrode the temperature is lower than 50 °C and the complete ablation is not reached.

Moreover, in Figure 34 the tissue temperature evolution is displayed for 65 V and it is confirmed that the differences in terms of temperatures are not so relevant as in 45 V application. However, the complete ablation of the tumoral tissue is obtained at the end of treatment; in fact, at 2 cm far from the electrode, in correspondence with the tumour contour, tissue temperature is about 50 °C.

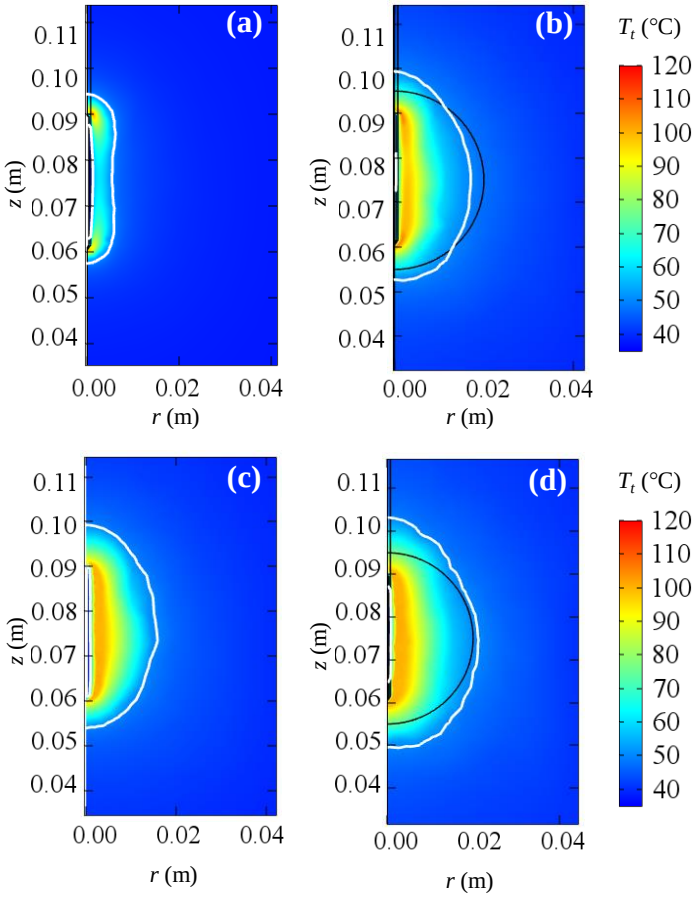

Figure 32. Tissue temperature distributions after 720 s of applied 45 V (a, b) and 65 V (c, d) computed for: healthy hepatic tissue (a, c) and tumoral hepatic tissue bounded by healthy liver (b, d). White and black lines represent the coagulation zone and tumour contours, respectively.

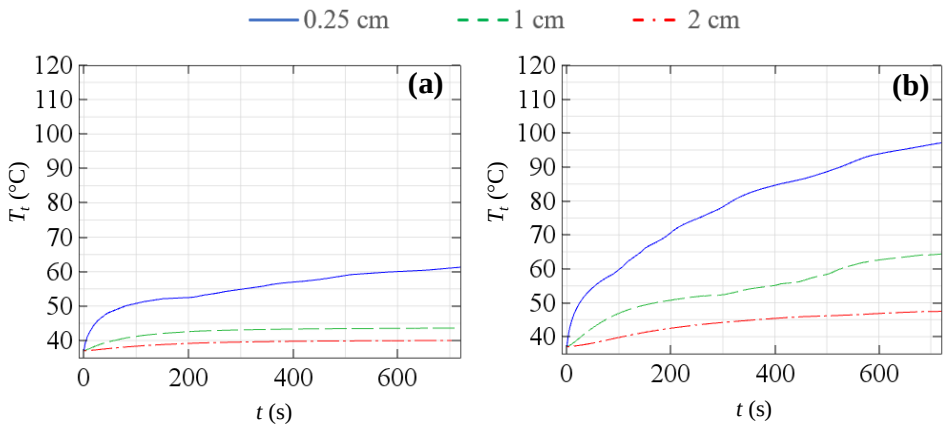

Figure 33. Tissue temperature evolution during 45 V RFA computed for: healthy hepatic tissue (a) and tumoral hepatic tissue bounded by healthy liver (b).

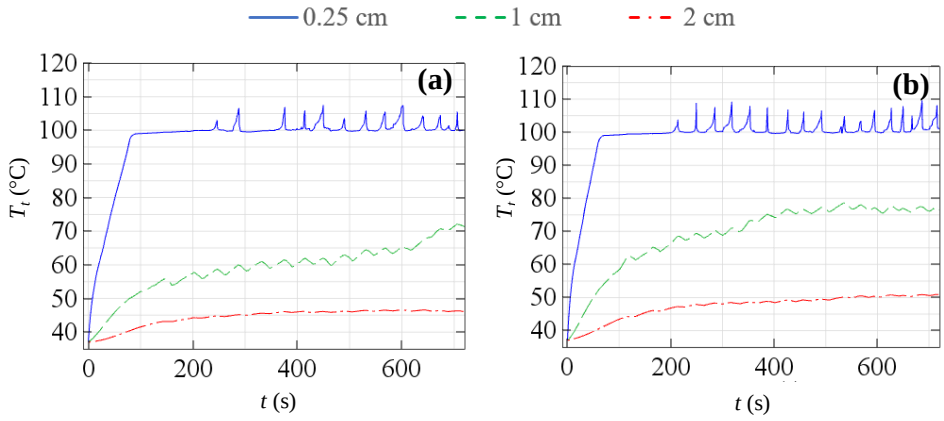

Figure 34. Tissue temperature evolution during 65 V RFA computed for: healthy hepatic tissue (a) and tumoral hepatic tissue bounded by healthy liver (b).

4.4. Conclusions

The aim of the present section is to investigate the behavior of pulsating heat protocols in modelling heat transfer for thermal ablation treatment of tumors. First of all, in paragraph 4.1., different periodical heating schemes and tissues morphologies in a spherical tumor tissue are analyzed. The tumor tissue is modelled as a porous sphere and a LTNE model is employed. The pulsating effect is modelled with references to a cosine function with different frequencies, and such different heating protocols are compared at equal delivered energy. The results show that pulsating effect always reduces maximum temperatures compared to the non-pulsating case; this is a very important result since it allows to reduce the steam popping phenomenon that occurs in thermoablation. Moreover, by means of the analysis of the percentage necrotic tissue in the domain, it is shown that that pulsating heat allows to necrotize the same tumoral tissue of the non-pulsating heat source, but with lower maximum temperature. In paragraph 4.2., the thermal problem is coupled with the electric problem to compare three different heat transfer models for radiofrequency ablation (RFA) of in vivo liver tissue using a cooled electrode. The study is conducted implementing a low voltage and two high voltage levels in order to consider cases with and without roll-off. The results show that using a similar protocol than Goldberg et al. [105] (e.g. 90 V pulsed protocol with a predominant current peak of about 1500 mA and 15 s off periods), for an in vivo experimental case, the porous media model achieved a better agreement with the experimental results, since Pennes' bioheat model tended to underestimate temperature fields for the cases here investigated. Finally, in paragraph 4.3., the same model is used to compare two distinct cases: a healthy liver tissue and a tumoral tissue bounded by the surrounding healthy liver. The considered different electrical and thermal properties for tumoral and healthy tissue play a fundamental role in the coagulation zones prediction. The outcomes show the relevant increase of the coagulation diameter, especially at low voltage, due to the higher electrical conductivity in tumoral tissue that entails higher total energy delivered at the end of the application. Even if the temperature peaks are about the same, the higher energy obtained gives higher mean temperatures in the domain. Furthermore, the temperature evolution in three different points of the tumour confirms the results above and highlights

the importance of distinguishing tumoral and healthy tissue in this kind of problem, in order to predict accurately the coagulation zones achieved during a thermal ablation. In fact, the results show that 2 cm far from the electrode, in correspondence with the tumor contour, tissue temperature is 50 °C only for 65 V application, so in this case the complete ablation of the tumoral tissue is reached. This is fundamental to avoid on the one hand an incomplete ablation and the consequent tumor recurrence, and on the other hand the coagulation of the surrounding healthy tissue. All the presented results highlight the importance of modelling accurately bioheat transfer in tissues, in order to improve medical protocols and devices in thermal ablation.

5.

MULTIPLE HEAT SOURCES APPLIED IN THERMAL ABLATION OF TISSUES

5.1. A novel Local Thermal non-equilibrium model for biological tissue applied to multiple-antennas configuration for thermal ablation

Thermal ablation can be induced by using different insertions, or by using various applicators to obtain a more diffuse ablation zone at the same time. Harari et al. [142], indeed, performed experiments on both ex vivo and in vivo liver models, for two and three-antennas arrays and with sequential and simultaneous ablations. They showed that multiple antennas for microwave ablation provide more confluent ablations with higher temperatures, with respect to sequential power delivery. Similar conclusions have been found by Brace et al. [143], that performed experiments on female domestic swine on three simultaneous triaxial antennas. Another reason for why multiple-antennas ablation can be useful is the reduction of temperature peaks, at equal necrosis volume, in order to avoid undesired phenomena like steam pops [115].

In this section, different simultaneous antennas are numerically investigated and compared with the one antenna arrangement; cases with two- or three- antennas are investigated. The mathematical model is built up based on a sphere with uniform heating zones, that simulate antennas heating, in which porous media equations for tissue and blood is employed under the local thermal non equilibrium between the two phases assumption. The model is modified in order to consider two-phase water vaporization (tissue and blood). Furthermore, different blood volume fractions and blood vessels are considered. Governing equations are solved with the commercial finite element code COMSOL Multiphysics®, and comparisons between various antennas are performed at equal total delivered energy, in order to understand if larger ablation zones can be achieved and peaks avoided.

5.1.1. Mathematical model

The biological tissue computational domain is here modelled as a spherical geometry as shown in Figure 35. The tumoral sphere radius is r_1=3.10 cm and the heating volume is represented by internal spheres with different dimensions, depending on the three different antennas configurations analyzed in this work.

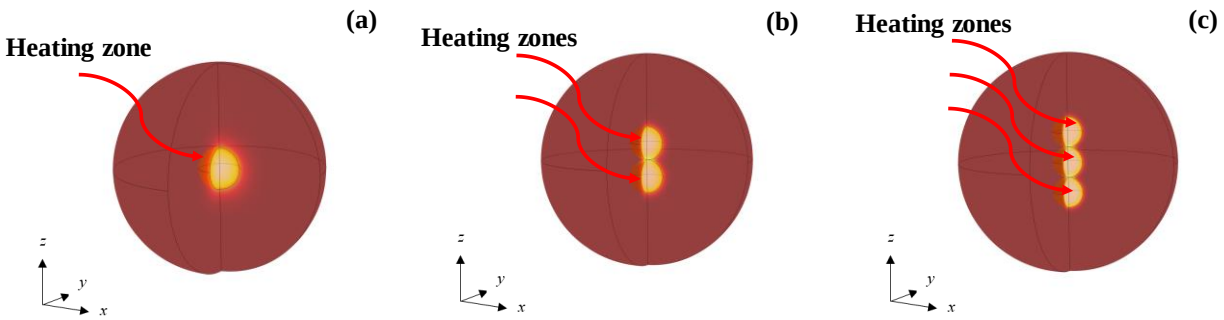

Figure 35. Geometry of the physical domain for the three different antennas configurations: (a) single antenna, (b) double antennas and (c) triple antennas.

In the first case, the single antenna heating volume is described with a single sphere with a radius r_2=0.620 cm, the second arrangement is made up of two antennas and the two heating zones are modelled with two adjacent spheres with the same radius r_3=0.492 cm, and finally, the last arrangement consists of three antennas represented by three identical adjacent spheres with a radius r_4=0.430 cm, where the central sphere is placed in the middle of the whole computational domain. In this way, the total heating volume is the same for all the cases and equal to 1 cm^3. In addition, it is possible to implement a 2D axisymmetric model in order to minimize computing time, since the problem has axial-symmetry, so the computational domains for the three different configurations are displayed in Figure 36.

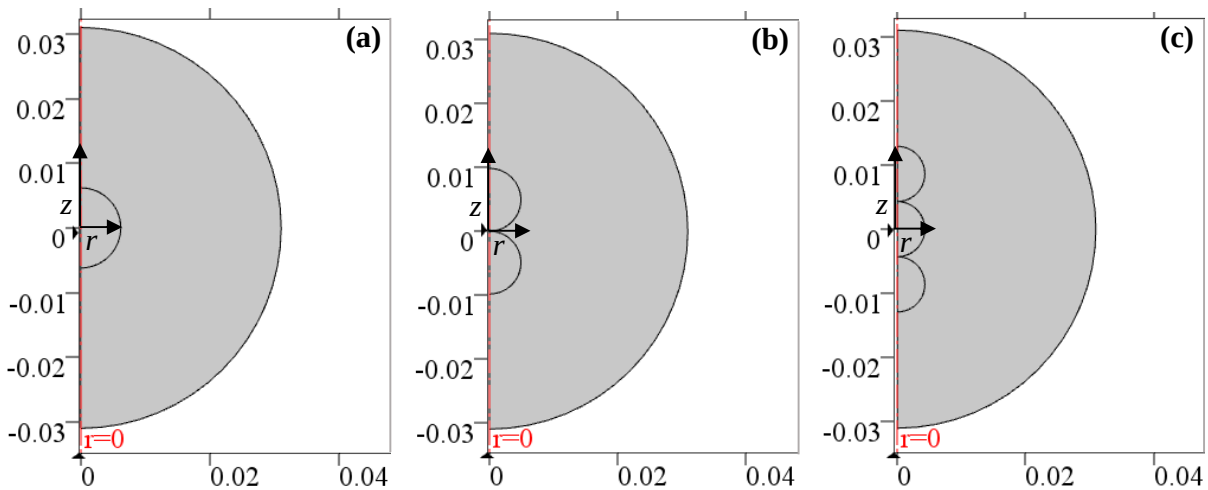

Figure 36. 2D computational domain for the three different antennas configurations: (a) single antenna, (b) double antennas and (c) triple antennas.

The entire domain is treated with the porous media theory [71] as described in the previous paragraph 2.1.2., using a novel Local Thermal Non-Equilibrium bioheat model, modified in order to include the water content vaporization in both the phases. So, two different equations are implemented for the extra-vascular and vascular regions, modifying Eqs. (86) and (87) as follows, to neglect the perfusion term, which does not affect the results.

For the blood phase:

$$\varepsilon(\rho c)_b\left(\frac{\partial\langle T_b\rangle}{\partial t}+\beta\langle\mathbf{u}\rangle\cdot\nabla\langle T_b\rangle\right)=\varepsilon k_b\nabla^2\langle T_b\rangle+ha\left(\langle T_t\rangle-\langle T_b\rangle\right)+\varepsilon Q_{ext}$$

(91)

for the tissue phase:

$$(1-\varepsilon)(\rho c)_t\frac{\partial\langle T_t\rangle}{\partial t}=(1-\varepsilon)k_t\nabla^2\langle T_t\rangle-ha\left(\langle T_t\rangle-\langle T_b\rangle\right)+(1-\varepsilon)Q_{ext} \quad (92)$$

In this case, four different types of blood vessel are considered, following the work of Crezee and Lagendijk [88]. So, diameters and the corresponding blood velocities of capillaries, terminal arteries, terminal branches, and tertiary branches are selected. Moreover, two different values for porosity are employed, i.e., 0.1 and 0.3, to cover the experimental measures found in literature for different liver tissues [126, 128, 131]. The interfacial heat transfer coefficient h is 170 W m^{-2} K^{-1}, as in Yuan [72]. In Table 15 all the values employed for blood velocities and diameters are resumed, with the related specific surface areas a and the resulting volumetric convective coefficients $h_v = a \cdot h$ for all the cases considered.

Table 15. Values employed for diameters and blood velocities and the related specific surface areas and volumetric convective coefficients.

	d (mm)	$\|\mathbf{u}\|$ (cm s^{-1})	a (m^{-1})		h_v (W m^{-3} K^{-1})	
			ε = 0.1	ε =0.3	ε = 0.1	ε =0.3
Capillaries	0.008	0.07	50000	150000	8.50 x 10^6	2.55 x 10^7
Terminal arteries	0.03	0.4	13333	40000	2.27 x 10^6	6.80 x 10^6
Terminal branches	0.05	2	8000	24000	1.36 x 10^6	4.08 x 10^6
Tertiary branches	0.14	3.4	2857	8571	4.86 x 10^5	1.46 x 10^6

Furthermore, Q_{ext} is the external power density applied during the thermal ablation treatment and the symbol <> refers to the volume averaged quantity of a generic variable. As regards the fluid phase, the blood velocity is assumed uniform in all directions in order to simulate a sort of *in vivo* vascular network. Nevertheless, as the coagulation of tumoral tissue occurs, the blood velocity becomes zero, thus the β coefficient is introduced into Eq. (91), equal to 0 or 1 depending on the value of thermal damage function Ω defined here by using the Arrhenius model [33] as previously described in Eq. (82), where, in this case, A = 3.247 x 10^{43} s^{-1} and ΔH = 2.814 x 10^5 J mol^{-1} as in [110]. The thermal damage is evaluated using the D99 thermal damage contour, considering the isoline at Ω = 4.6, that corresponds to the 99% cell death probability, so the β coefficient will be 1 for Ω < 4.6 and 0 for Ω = 4.6. In fact, this value gives a better prediction of coagulation zone size than Ω = 1 (68 % probability of cell death). Moreover, the LTNE equations are modified to include the water content vaporization in both liver tumoral tissue and blood separately, by following the enthalpy method described by Abraham and Sparrow [120], and previously reported in Eqs. (84) and (88) for tissue phase and blood phase respectively, where C_w is the water content inside the tumoral liver tissue (81%) or in the blood (79%) as found in literature [125, 141].

As concerns the initial and boundary conditions, a uniform initial temperature distribution of 37 °C is assumed for both tumoral tissue and blood. For t > 0 temperature is maintained at 37 °C on the external contour, because the domain is large enough to neglect boundary effects from surroundings, and the adiabatic condition is employed on the symmetry axis, because of the axial symmetry of the model. Thermal properties of both tissue and blood phases are assumed to be isotropic through the domain and they are chosen according to Trujillo et al. [109] and Zhang et al. [110] as resumed in Table 16.

The external power density given is Q_{ext} = 5 x 10^6 W m^{-3} for each single heating volume in the different arrangements. The heating time is 100 s for all the cases, so the total external energy transferred to the tissue is 500 J. The LTNE equations are solved numerically by using the finite-element commercial code COMSOL Multiphysics software. A 2D axisymmetric model is employed to minimize computing time. A triangular mesh of 9388 elements is applied, the absolute tolerance used is 0.0001, the time stepping method is the intermediate BDF with initial and maximum steps of 0.001 s and 0.1 s.

Table 16. Characteristics of the materials employed in the model.

	ρ (kg·m^{-3})	c (J·kg^{-1}·K^{-1})	k (W·m^{-1}·K^{-1})
Tumor	1045	3760	0.600
Blood	1000	3639	0.502

The model is validated by comparing tissue temperature profiles at the center of the sphere herein obtained with results from Yuan [72], where the LTNE model is employed for different conditions of porosity, blood velocities and external power densities for a cube-shaped tissue with a single cubic heating zone at the center. To notice that the geometry chosen by Yuan [72] is a cube with the same volume of the spheres used in the present work, so, the external power density is the same. In Figure 37, tissue temperature profiles are reported for two different heating conditions and porosities, considering three different blood velocities; they agree very well in all cases.

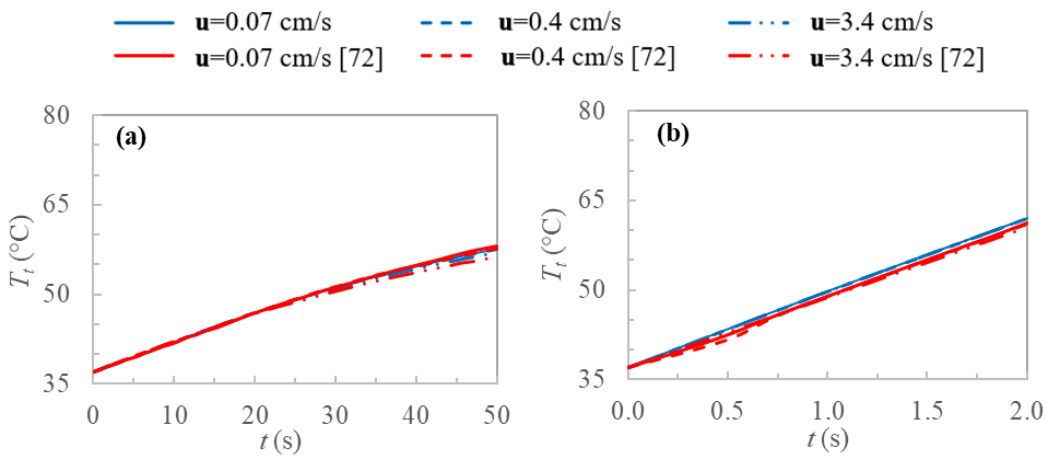

Figure 37. Validation of the model. Tissue temperatures at the center of the sphere for present work and Yuan [72]: (a) ε=0.005, Q_{ext} = 2 x 10^6 W m^{-3} and (b) ε=0.05, Q_{ext} = 50 x 10^6 W m^{-3}.

5.1.2. Results

The outcomes are presented for the three antennas configurations in terms of coagulation zones achieved at the end of the application, maximum temperatures obtained and temperature fields at different heating times, for two different values of porosity, i.e., ε=0.1 and ε=0.3, and four different types of blood vessels, i.e., capillaries, terminal arteries, terminal branches, and tertiary branches. The first result to highlight is that the size of the completely coagulated tissue, obtained at Ω = 4.6, is larger for all the three antennas

arrangements compared at the lowest porosity value ε=0.1, as shown in Figure 38. So, even if the total power and energy are the same in all the configurations, using multiple antennas instead of a single antenna offers a potential solution for creating ablation zones with larger dimensions. The coagulation zone increases by about 6 mm for all the blood vessels considered using the two-antennas configuration, while the three antennas configuration gives the best results with an increase of more than 1 cm for all the vessels, as it is displayed in Table 17.

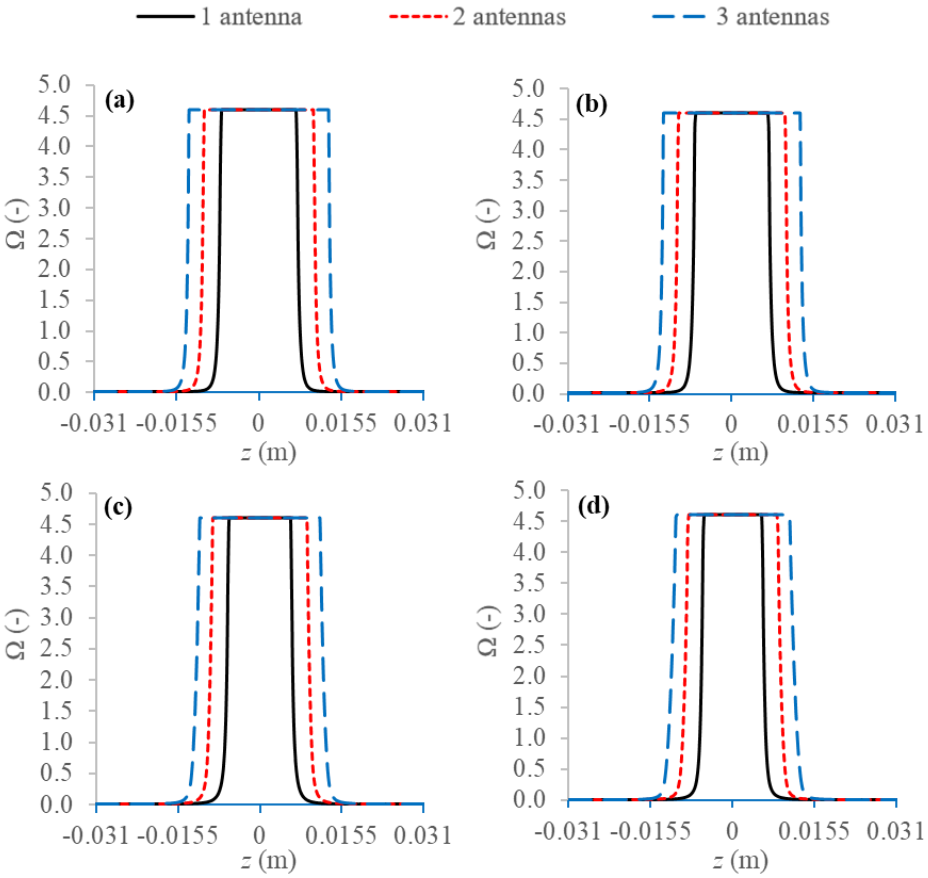

Figure 38. Thermal damage **Ω** at the end of the application and ε=0.1, for the three different antennas configurations, and the different tissue vascularizations: (a) capillaries, (b) terminal arteries, (c) terminal branches and (d) tertiary branches.

Table 17. Coagulation diameters obtained for ε=0.1.

	Coagulation diameter d_c (cm)		
	1 antenna	2 antennas	3 antennas
Capillaries	1.40	2.05	2.62
Terminal arteries	1.36	2.01	2.58
Terminal branches	1.16	1.78	2.27
Tertiary branches	1.08	1.66	2.11

Comparing the different coagulation zones for the same arrangement but at different blood vessels diameters, their width is almost the same or slightly reduces for terminal branches and tertiary branches.

This because as the blood vessel diameter increases, the blood velocity increases too, and the heat is removed more from the tissue phase by the blood phase.

As regards the highest value of porosity ε=0.3, the size of the completely coagulated tissue, obtained at **Ω** = 4.6 is larger for the three antennas configuration when capillaries and terminal arteries are considered. However, simulating terminal branches and tertiary branches for the blood vessels, the 99% cell death probability is not achieved except for the terminal branches with one antenna arrangement, as shown in Figure 39.

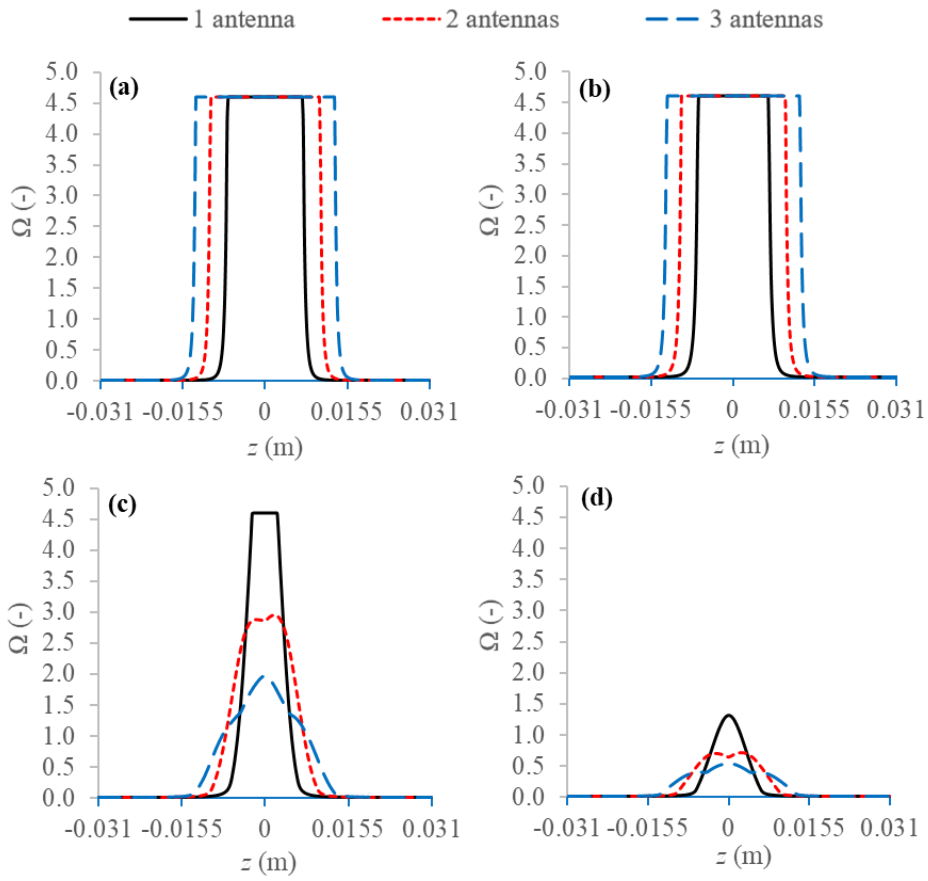

Figure 39. Thermal damage **Ω** at the end of the application and ε=0.3, for the three different antennas configurations, and the different tissue vascularizations: (a) capillaries, (b) terminal arteries, (c) terminal branches and (d) tertiary branches.

For this value of porosity, the coagulation zone increases by about 6.5 mm for capillaries and terminal arteries using the two antennas configuration, while the three antennas configuration gives the best results again, with an increase of 1.2 cm for capillaries and terminal arteries, as it is resumed in Table 18.

Because of the higher amount of blood fraction, in this case the heat removed from the tissue is higher compared to the previous case of lowest porosity, in fact the higher the porosity, the larger the convective contribution of the mass blood flux, so tissue temperatures are generally lower as the same blood vessels

diameters are considered. Thus, another important outcome to highlight regards the maximum tissue temperatures reached as it is shown in Figure 40.

Table 18. Coagulation diameters obtained for ε=0.3.

	Coagulation diameter d_c (cm)		
	1 antenna	2 antennas	3 antennas
Capillaries	1.40	2.05	2.62
Terminal arteries	1.32	1.97	2.50
Terminal branches	0.45	no	no
Tertiary branches	no	no	no

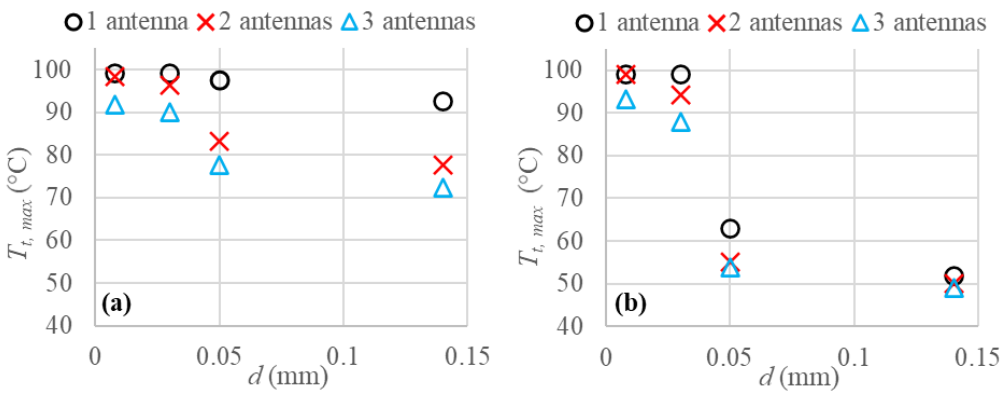

Figure 40. Maximum tissue temperatures achieved for the three different antennas configurations, for the four different tissue vascularizations: (a) ε = 0.1 and (b) ε = 0.3

It is clear from the figure that the three antennas arrangement allows to have lower maximum tissue temperatures in all the cases. This happens because the energy distribution in the single heating volumes in two antennas and three antennas configurations is more uniform, even if the total energy distributed in the heating zones is the same. This is another advantage of thermal ablation with multiple antennas, applying the same total power and energy. In fact, it is important to avoid very high temperatures, because of the complications that can occur such as the steam popping phenomenon [115], the roll off phenomenon [116] using radiofrequencies, the healthy tissue destruction, and the damage of medical devices.

To show more in detail this aspect, in Figure 41 tissue temperature fields are displayed for the three different antennas arrangements at four different heating times, i.e., 25 s, 50 s, 75 s, and 100 s, choosing terminal arteries for blood vessels. This is a reasonable choice according to Chen and Holmes' LTNE model [42] in which blood heat exchange is assumed to occur only downstream of the terminal arteries before the arterioles. As previously displayed, the porosity value does not affect the results for this type of vascularization, so only one case is shown, i.e., for ε = 0.3. Figure 41 gives a clearer overview of temperature distribution during the application; in fact, it can be easily observed the lower mean temperatures obtained as the number of antennas employed increases. The temperature decrease is due to

the lower power applied by the single antenna used in the multiple antennas' configurations, even if the total applied power is the same in the three cases. The wider coagulation zones achieved by multiple antennas is clearly shown by the black lines in Figure 41. Moreover, it can be underlined that the coagulation zones are symmetric along both *r* and *z* directions, thus, considering a different antennas' location, a different arrangement could be selected depending on the tumor shape.

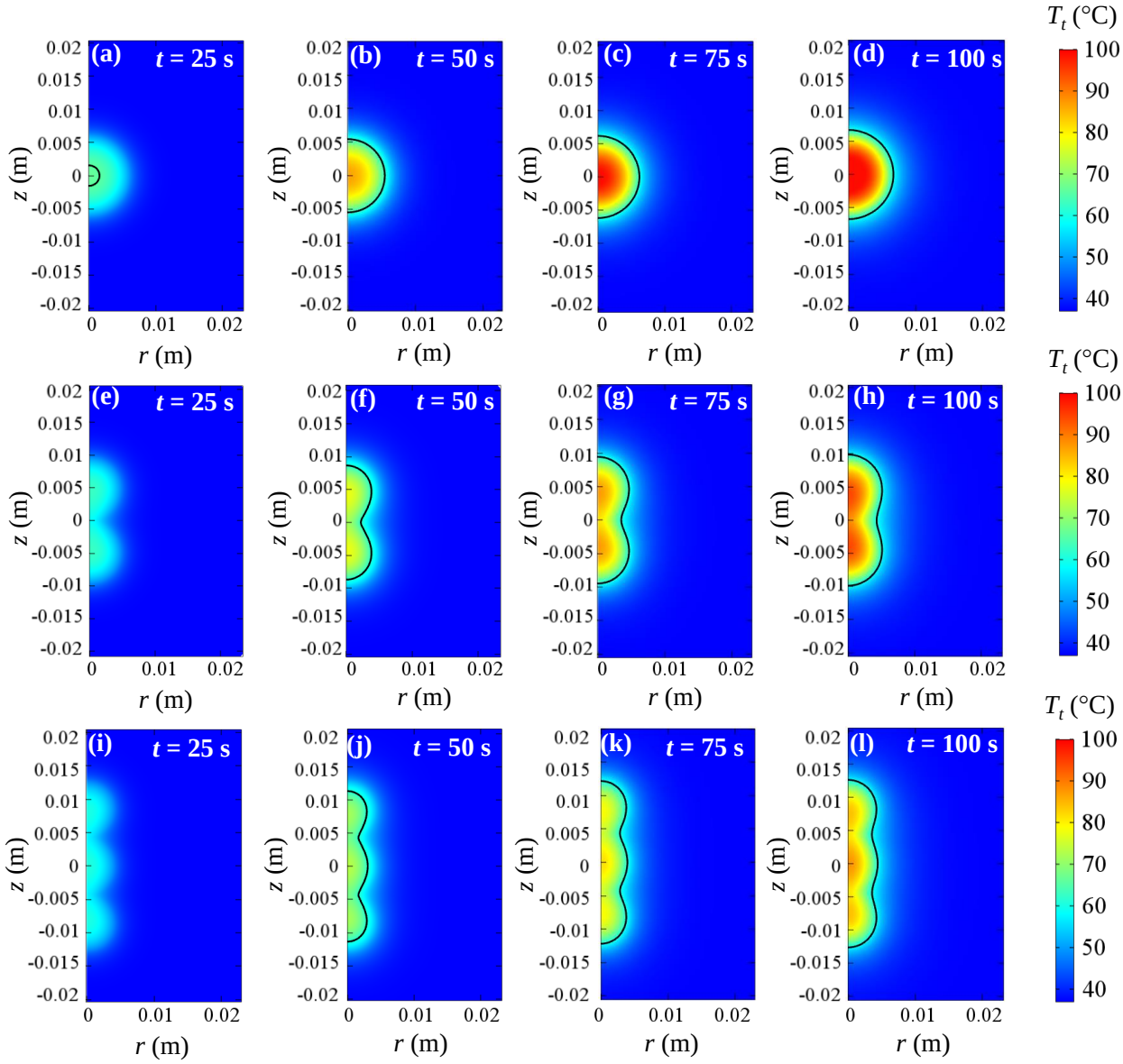

Figure 41. Tissue temperature distributions at different heating times for one antenna (a-d), two antennas (e-h) and three antennas (i-l) configurations. Terminal arteries for the blood vessels and ε = 0.3 for the porosity are considered.

5.2. Conclusions

In this section The purpose the effects of single, double, and triple antennas arrangements on thermal ablation of a tumoral tissue is described. The tissue is modelled as a porous medium. The heat sources are referred only to a part of the tissue domain and they release equal total power and energy for different antennas configurations. A Local Thermal Non-Equilibrium (LTNE) model is employed and modified in

order to take into account the vaporization of the different water content in tumor and blood, and governing equations with the appropriate boundary conditions are solved with the finite-element commercial software COMSOL Multiphysics®. Results are presented in terms of temperature fields and tissue damage for the three different antennas arrangements, different porosities and vascularizations. Even if the total power and energy are the same in all the analyzed arrangements, using multiple antennas instead of a single antenna offers a potential solution for creating ablation zones with larger dimensions. Moreover, the multiple antennas arrangements allow to have lower maximum tissue temperatures in all the cases compared to the single antenna. These results are very important to improve the medical protocols and devices in thermal ablation, in fact, the objective of the treatment is to achieve the complete necrosis of tumoral tissue, avoiding very high temperatures and the related complications such as the steam popping phenomena, the roll off phenomenon in radiofrequency ablation, the healthy tissue destruction and the damage of medical devices. Moreover, along the direction of the antenna's location, the wider coagulation zones achieved by multiple antennas suggests that a different arrangement could be selected depending on the tumor shape.

CONCLUSIONS

This thesis work is focused on the key role that modelling heat transfer can play in thermal therapies, especially in thermal ablation treatments of cancerous tissues, since it is nowadays considered a promising technique to overcome the critical issues of the most common procedures such as surgery, chemotherapy, and radiotherapy. Thermal ablation of tumors, indeed, is a minimally invasive treatment option for cancer, with certain advantages such as minor side effects, shorter hospital stays and consequently lower costs. The most common approach is a percutaneous treatment performed with the aid of imaging techniques, during which an energy source (commonly radiofrequency or microwave) is focused in the target zone (the tumoral tissue) by means of a probe, that causes the tumor destruction. The main shortcoming of performing a thermal ablation is to not achieve the complete tissue ablation, so the risk of a tumor recurrence becomes higher. In this context, modelling heat transfer in thermal therapies allows to develop more and more accurate bioheat models for clinical applications, predicting the final necrotic tissue diameters and volumes. In this thesis work, a general overview of the different employed techniques in hyperthermia treatments of biological tissues and in particular tumors is first of all introduced, together with techniques used to estimate thermal damage. Then, different bioheat models are implemented and numerically solved on distinct simulated biological media, considering various ablation protocols such us the use of pulsating heat sources and probes arrangements, obtaining relevant results.

The first result suggests that the porous media-based Local Thermal Non-Equilibrium equations are the starting point to develop more and more accurate bioheat models, since it is a good compromise between accuracy and complexity. Secondly, the most powerful result achieved using a pulsating heat source instead of a constant one is the decreasing of maximum temperature in any considered case. Furthermore, the evaluation of tissue damage at the end of treatment shows that pulsating heat allows to necrotize the same tumoral tissue area of the non-pulsating heat source. In addition, a more complex model is developed to study a pulsating protocols application for radiofrequency ablation (RFA) of in vivo liver tissue using a cooled electrode and three different voltage levels. Three distinct heat transfer models coupled to the electrical problem are compared and modified to consider two-phase water vaporization. The results in terms of coagulation transverse diameters and temperature fields at the end of the application show significant differences, especially between Pennes equation and the modified LTNE and LTE models at high voltage level. The new modified porous media-based models cover the ranges found in the few in vivo experimental studies in the literature and are closer to the published results with similar in vivo protocol. The same model is applied considering tumoral tissue surrounded by healthy tissue and the outcomes show relevant differences when the tumor is included in the model. Thus, the different electrical conductivity and thermal properties between the two types of tissues play a fundamental role in the outcomes.

Finally, the previous LTNE modified model is applied to a spherical tumoral tissue, in order to investigate the effects of different antennas configurations in thermal ablation. The results show that using multiple antennas instead of a single antenna offers a potential solution for creating ablation zones with larger dimensions and to allow at the same time to have lower maximum tissue temperatures in all the cases compared to the single antenna configuration.

All these outcomes achieved highlight how important could be to perform more and more accurate bioheat models, in order to advance in new thermal ablation protocols and devices, personalizing the treatment depending on different organs, tumors dimensions and patient conditions.

FUTURE PERSPECTIVES

In the future, the next step of this research will regard the experimental validation of the developed bioheat models, using different techniques: first of all, bio-images and histological samples of tumors from hospitals will be used. In particular, data set of re-elaborated computed tomography (CT) images and biopsy samples will be manipulated and employed in specific tumor modelling. The experimental campaign will be aimed at validating the mathematical and numerical models as a valuable tool to simulate and guide therapeutic clinical procedures. The development of hydrogel tissue-mimicking phantoms and of patient-derived tumor models will constitute, with increasing degree of complexity, two pre-clinical models able to closely mimic the physical and geometrical properties of target tissues. The use of hydrogel-based tissue-mimicking phantoms with a well-controlled level of hydration, will provide the possibility to monitor the time-dependent temperature distribution after single or multiple local fast thermal perturbations. These models will constitute the closest approximation to the real tissue of clinical interest for experimental studies of temperature-based therapies and, together with hydrogel phantoms, to evaluate the ability of numerical models to predict the experimental results. Obtaining a more and more accurate bioheat model has a key role in predicting tissue temperature fields and consequently final necrosis volumes. These achievements are relevant in thermal ablation field because the provided data for the medical devices employed nowadays are set on the results from ex vivo or in vivo healthy animal tissues. Thus, the suggested time-power combinations to obtain a certain necrosis zone do not correspond to the real achieved outcomes. This issue becomes more relevant when large vessels are near the target region to be ablated and the heat sink effect plays a significant role. Thanks to the developed tumor models and experimental setup, the real influence of the heat sink effect during a thermal ablation can be studied in depth too. Moreover, on the basis of patient data, patient-specific models will be built, and different ablation settings will be simulated. The optimal ablation values predicted by simulation will be applied on clinical treatments. Real-time measurement of heating of tumor and surrounding tissues and imaging follow up will be used as standard of reference. The final purpose is consequently to achieve personalized thermal ablation protocols in terms of applied power and treatment duration, depending on different organs, tumor characteristics, and clinical conditions of the patient and to improve the thermal ablation devices and techniques.

CONTRIBUTIONS

This PhD thesis is based on the different research works developed and results achieved during the PhD program, which include international conference participations and journal publications. In particular, the contributions related to the different sections are listed as follows and specified in the references section: introduction [144, 145], chapter 2 [145], chapter 3 [146], chapter 4 [147,148], chapter 5 [149].

REFERENCES

[1] "Definition of Hyperthermia," Treccani, accessed September 07, 2020, http://www.treccani.it/enciclopedia/ipertermia_%28Enciclopedia-Italiana%29/

[2] P. S. Yarmolenko, E. J. Moon, C. Landon, A. Manzoor, D. W. Hochman, B. L. Viglianti, M. W. Dewhirst, Thresholds for thermal damage to normal tissues: an update, Int. J. Hyperther. 27 (2011) 320-343.

[3] M. M. Scheinman, F. Morady, D. S. Hess, R. Gonzalez, Catheter-induced ablation of the atrioventricular junction to control refractory supraventricular arrhythmias, Jama 248 (1982) 851-855.

[4] A. Jordan, R. Scholz, K. Maier-Hauff, M. Johannsen, P. Wust, J. Nadobny, H. Schirra, H. Schmidt, S. Deger, S. Loening, W. Lanksch, R. Felix, Presentation of a new magnetic field therapy system for the treatment of human solid tumors with magnetic fluid hyperthermia, J. Magn. Mater. 225 (2001) 118-126.

[5] T. Ohguri, H. Imada, F. Kato, K. Yahara, T. Morioka, K. Nakano, Y. Korogi, Radiotherapy with 8 MHz radiofrequency-capacitive regional hyperthermia for pain relief of unresectable and recurrent colorectal cancer, Int. J. Hyperther. 22 (2006) 1-14.

[6] C. S. Kumar, F. Mohammad, Magnetic nanomaterials for hyperthermia-based therapy and controlled drug delivery, Adv. Drug Deliv. Rev. 63 (2011) 789-808.

[7] J. I. Almeida, J. K. Raines, Radiofrequency ablation and laser ablation in the treatment of varicose veins, Ann. Vasc. Surg. 20 (2006) 547-552.

[8] J. Van der Zee, Heating the patient: a promising approach?, Ann. Oncol. 13 (2002) 1173–1184.

[9] H. Furusawa, K. Namba, S. Thomsen, F. Akiyama, A. Bendet, C. Tanaka, Y. Yasuda, and H. Nakahara, Magnetic resonance-guided focused ultrasound surgery of breast cancer: reliability and effectiveness, J. Am. Coll. Surg. 203 (2006) 54–63.

[10] M. C. Peek, M. Ahmed, A. Napoli, S. Usiskin, R. Baker, and M. Douek, Minimally invasive ablative techniques in the treatment ofbreast cancer: a systematic review and meta-analysis, Int. J. Hyperther. 33 (2016) 1–12.

[11] E. G. Moros, and W. R. Hendee, Physics of Thermal Therapy: Fundamentals and Clinical Applications, Boca Raton: CRC Press, Taylor & Francis Group, 2012, 375 pp.

[12] A.I. Minchinton, and I. F, Tannock. Drug penetration in solid tumors, Nat. Rev. Cancer. 6 (2006) 583–592.

[13] A. J. Primeau, A. Rendon, D. Hedley, L. Lilge, and I. F. Tannock, The distribution of the anticancer drug doxorubicin in relation to blood vessels in solid tumors, Clin. Cancer Res. 11 (2005) 8782–8788.

[14] J. L. Au, S. H. Jang, J. Zheng, C. T. Chen, S. Song, L. Hu, and M. G. Wientjes, Determinants of drug delivery and transport in solid tumors, J. Control. Release. 74 (2001) 31-46.

[15] E. L. Jones, J. R. Oleson, L. R. Prosnitz, T. V. Samulski, Z. Vujaskovic, D. Yu, L. L. Sanders, and M. W. Dewhirst, A Randomized Trial of Hyperthermia and Radiation for Superficial Tumors, J. Clin. Oncol. 23 (2005) 3079-3085.

[16] B. Emami, and C. W. Song, Physiological mechanisms in hyperthermia: a review, Int. J. Radiat. Oncol. Biol. Phys. 10 (1984) 289-295.

[17] T. S. Herman, and B. A, Teicher. Summary of studies adding systemic chemotherapy to local hyperthermia and radiation, Int. J. Hyperther. 10 (1994) 443-449.

[18] R. D. Issels, L. H. Lindner, J. Verweij, P. Wust, P. Reichardt, B. C. Schem, S. Abdel-Rahman, S. Daugaard, C. Salat, C. M. Wendtner, Z. Vujaskovic, R. Wessalowski, K. W. Jauch, H. R. Dürr, F. Ploner, A. Baur-Melnyk, U. Mansmann, W. Hiddemann, J. Y. Blay, P. Hohenberger, and for the European Organisation for Research and Treatment of Cancer Soft Tissue and Bone Sarcoma Group /EORTC-STBSG) and the European Society for Hyperthermic Oncology (ESHO), Neo-adjuvant chemotherapy alone or with regional hyperthermia for localised high-risk soft tissue sarcoma: a randomised phase 3 multicentre study, Lancet Oncol. 11 (2010) 561-570.

[19] R. T. Bourdon, B. B. Nelson-Cheeseman, J. P. Abraham, Prediction, identification, and initial treatment guide for scald injuries, Aust. J. Emerg. Crit. Care Med 3 (2016) 1043.

[20] J. P. Abraham, B. Plourde, L. Vallez, J. R. Stark, K. R. Diller, Estimating the time and temperature relationship for causation of deep-partial thickness skin burns, Burns 41 (2015) 1741-1747.

[21] J. P. Abraham, M. P. Hennessey, W. J. Minkowycz, A simple algebraic model to predict burn depth and injury, Int. Commun. Heat Mass 38 (2011) 1169-1171.

[22] M. W. Dewhirst, J. P. Abraham, B. Viglianti, Evolution of thermal dosimetry for application of hyperthermia to treat cancer, Adv. Heat Transf. 47 (2015) 397-421.

[23] S. A. Sapareto, W. C. Dewey, Thermal dose determination in cancer therapy, Int. J. Radiol. Oncol. Biol. Phys. 10 (1984) 787-800.

[24] W. C. Dewey, L. E. Hopwood, S. A. Sapareto, L. E. Gerweck, Cellular responses to combinations of hyperthermia and radiation, Radiology 123 (1977) 463-474.

[25] M. J. Borrelli, L. L. Thompson, C. A. Cain, W. C. Dewey, Time-temperature analysis of cell killing of BHK cells heated at temperatures in the range of 43.5 C to 57.0 C, Int. J. Radiol. Oncol. Biol. Phys. 19 (1990) 389-399.

[26] S. A. Baldwin, A. Pelman, J. L. Bert, A heat transfer model of thermal balloon endometrial ablation, Ann. Biomed. Eng. 29 (2001) 1009-1018.

[27] I. A. Chang, U. D. Nguyen, Thermal modeling of lesion growth with radiofrequency ablation devices, Biomed. Eng. Online 3 (2004) 27.

[28] J. Pearce, Mathematical models of laser-induced tissue thermal damage, Int. J. Hyperther. 27 (2011) 741-750.

[29] J. P. Abraham, B. B. Nelson-Cheeseman, E. M. Sparrow, J. E. Wentz, J. M. Gorman, S. E. Wolf, Comprehensive method to predict and quantify scald burns from beverage spills, Int. J. Hyperther. 32 (2016) 900-910.

[30] R. T. Bourdon, B. B. Nelson-Cheeseman, J. P. Abraham, Review of the initial treatment and avoidance of scald injuries, World J. Dermatol. 6 (2017) 17-26.

[31] N. N. Johnson, J. P. Abraham, Z. I. Helgeson, W. J. Minkowycz, E. M. Sparrow, An archive of skin-layer thicknesses and properties and calculations of scald burns with comparisons to experimental observations, J. Therm. Sci. Eng. Appl. 3 (2011) 011003.

[32] P. Mertyna, W. Goldberg, W. Yang, S. N. Goldberg, Thermal ablation: A comparison of thermal dose required for radiofrequency-, microwave-, and laser-induced coagulation in an ex vivo bovine liver model, Acad. Radiol. 16 (2009) 1539-1548.

[33] I. A. Chang, Considerations for thermal injury analysis for RF ablation devices, Open Biomed. Eng. J. 4 (2010) 3-12.

[34] S. B. Field, G. P. Raaphorst, Thermal Dose, in: S. B. Field, J. W. Hand (Eds.), An introduction to the practical aspects of clinical hyperthermia, Taylor and Francis, London (UK), 1990, pp. 69-76.

[35] S. Weininger, J. Pfefer, I. Chang, Factors to consider in a risk analysis for safe surface temperature, in: Proceedings of the IEEE Symposium on Product Safety Engineering, Schaumberg (Illinois), 2005, pp. 83-91.

[36] M. K. Jain, P. D. Wolf, A three-dimensional finite element model of radiofrequency ablation with blood flow and its experimental validation, Ann. Biomed. Eng. 28 (2000) 1075-1084.

[37] L. J. Vallez, B. D. Plourde, J. E. Wentz, B. B. Nelson-Cheeseman, J. P. Abraham, A review of scald burn injuries, Intern. Med. Rev 3 (2017) 1-18.

[38] B. L. Viglianti, M. W. Dewhirst, J. P. Abraham, J. M. Gorman, E. M. Sparrow, Rationalization of thermal injury quantification methods: application to skin burns, Burns 40 (2014) 896-902.

[39] H. H. Pennes, Analysis of tissue and arterial blood temperatures in the resting human forearm, J. Appl. Physiol. 1 (1948) 93-122.

[40] W. Wulff, The energy conservation equation for living tissue, IEEE Trans. Biomed. Eng. 6 (1974) 494-495.

[41] H. G. Klinger, Heat transfer in perfused biological tissue I: general theory, Bull. Math. Biol. 36 (1974) 403-415.

[42] M. M. Chen, K. R. Holmes, Microvascular contributions in tissue heat transfer, Ann. Ny. Acad. Sci. 335 (1980) 137-150.

[43] S. Weinbaum, L. M. Jiji, D. E. Lemons, Theory and experiment for the effect of vascular microstructure on surface tissue heat ttzouransfer—Part I: anatomical foundation and model conceptualization, J. Biomech. Eng. 106 (1984) 321-330.

[44] S. Weinbaum, L. M. Jiji, D. E. Lemons, Theory and experiment for the effect of vascular microstructure on surface tissue heat ttzouransfer—Part II: model formulation and solution, J. Biomech. Eng. 106 (1984) 331-341.

[45] S. Weinbaum, and L. Jiji, A new simplified bioheat equation for the effect of blood flow on local average tissue temperature, J. Biomech. Eng. 107 (1985) 131–141.

[46] D. Y. Tzou, A unified field approach for heat conduction from macro- to micro-scales, J. Heat Transf. 117 (1995) 8–16.

[47] D. Y. Tzou, Experimental support for the lagging behaviour in heat propagation, J. Thermophys. Heat Transf. 9 (1995) 686–693.

[48] Y. Xuan, W. Roetzel, Bioheat equation of the human thermal system, Chem. Eng. Technol. 20 (1997) 268-276.

[49] A. R. Khaled, K. Vafai, The role of porous media in modeling flow and heat transfer in biological tissues, Int. J. Heat Mass Tran. 46 (2003) 4989-5003.

[50] K. Khanafer, and K. Vafai, The role of porous media in biomedical engineering as related to magnetic resonance imaging and drug delivery, Int. J. Heat Mass Transf. 42 (2006) 939–953.

[51] A. Nakayama, F. Kuwahara, A general bioheat transfer model based on the theory of porous media, Int. J. Heat Mass Tran. 51 (2008) 3190-3199.

[52] E. J. Berjano, Theoretical modeling for radiofrequency ablation: state-of-the-art and challenges for the future, Biomed. Eng. Online. 18 (2006) 5-24.

[53] D. Yang, M. C. Converse, D. M. Mahvi, J. G. Webster, Expanding the bioheat equation to include tissue internal water evaporation during heating, IEEE Trans. Biomed. Eng. 54 (2007) 1382-1388.

[54] M. Jaunich, S. Raje, K. Kim, K. Mitra, and Z. Guo, Bio-heat transfer analysis during short pulse laser irradiation of tissues, Int. J. Heat Mass Transf. 51 (2008) 5511-5521.

[55] M. Cavagnaro, R. Pinto, and V. Lopresto, Numerical models to evaluate the temperature increase induced by ex vivo microwave thermal ablation, Phys. Med. Biol. 60 (2015) 3287-331.

[56] Y. L. Shao, B. Arjun, H. L. Leo, and K. J. Chua, Nano-assisted radiofrequency ablation of clinically extracted irregularly-shaped liver tumours, J. Therm. Biol. 66 (2017) 101-113.

[57] K. C. Leong, C. Yang, and S. M. S. Murshed, A model for the thermal conductivity of nanofluids–the effect of interfacial layer, J. Nanopart. Res. 8 (2006) 245–254.

[58] G. D. Guerrero López, M. F. J. Cepeda Rubio, J. I. Hernández Jácquez, A. Vera Hernandez, L. Lejia Salas, F. Valdes Perezgasga, and F. Flores Garcia, Computational fem model, phantom and ex vivo swine breast validation of an optimized double-slot microcoaxial antenna designed for minimally invasive breast tumor ablation: theoretical and experimental comparison of temperature, size of lesion, and swr, preliminary data, Comput. Math. Methods Med. 1 (2017) 1-11.

[59] R. Ortega Palacios, C. J. Trujillo Romero, and M. F. J. Cepeda Rubio, A feasibility of using a novel 2.45 GHz double short distance slot coaxial antenna for minimally invasive cancer breast microwave ablation therapy: computational model, phantom, and in vivo swine experimentation, J. Healthc. Eng. (2018) 1-10.

[60] E. Majchrzak, G. Dziatkiewicz, and M. Paruch, The modelling of heating a tissue subjected to external electromagnetic field, Acta Bioeng. Biomech. 10 (2008), 29-37.

[61] P. Keangin, T. Wessapan, and P. Rattanadecho, Analysis of heat transfer in deformed liver cancer modeling treated using a microwave coaxial antenna, Appl. Therm. Eng. 31 (2011) 3243-3252.

[62] P. Keangin, P. Rattanadecho, and T. Wessapan, An analysis of heat transfer in liver tissue during microwave ablation using single and double slot antenna, Int. Commun. Heat Mass Transf. 38 (2011) 757–766.

[63] T. W. H. Sheu, M. A. Solovchuk, A. W. J. Chen, and M. Thiriet, On an acoustics–thermal–fluid coupling model for the prediction of temperature elevation in liver tumor, Int. J. Heat Mass Transf. 54 (2011) 4117-4126.

[64] J. A. Lopez Molina, M. J. Rivera, and E. Berjano, Analytical model based on a cylindrical geometry to study RF ablation with needle-like internally cooled electrode, Math. Probl. Eng.(2012) 1-16.

[65] P. K. Gupta, J. Singh, and K. N. Rai, A numerical study on heat transfer in tissues during hyperthermia, Math. Comput. Model. 57 (2013) 1018-1037.

[66] P. K. Gupta, J. Singh, K. N. Rai, and S. K. Rai, Solution of the heat transfer problem in tissues during hyperthermia by finite difference–decomposition method, Appl. Math. Comput. 219 (2013) 6882-6892.

[67] L. A. Bermeo Varon, H. R. Barreto Orlande, and G. E. Eliçabe, Estimation of state variables in the hyperthermia therapy of cancer with heating imposed by radiofrequency electromagnetic waves, Int. J. Therm. Sci. 98 (2015) 228-236.

[68] L. A. Bermeo Varon, H. R. Barreto Orlande, and G. E. Eliçabe, Combined parameter and state estimation in the radio frequency hyperthermia treatment of cancer, Num. Heat Transf. A- Appl. 70 (2016) 581-594.

[69] R. F. Reis, F. Dos Santos Loureiro, and M. Lobosco, 3D numerical simulations on GPUs of hyperthermia with nanoparticles by a nonlinear bioheat model, J. Comput. Appl. Math. 295 (2016) 35-47.

[70] J. A. Lopez Molina, M. J. Rivera, and E. Berjano, Analytical transient-time solution for temperature in non perfused tissue during radiofrequency ablation, Appl. Math. Model. 42 (2017) 618-635.

[71] K. Vafai, Handbook of Porous Media, third ed., CRC Press, Boca Raton (Florida), 2015.

[72] P. Yuan, Numerical analysis of temperature and thermal dose response of biological tissues to thermal non-equilibrium during hyperthermia therapy, Med. Eng. Phys. 30 (2008) 35-43.

[73] S. Mahjoob, and K. Vafai, Analytical characterization of heat transport through biological media incorporating hyperthermia treatment, Int. J. Heat Mass Transf. 52 (2009) 1608-1618.

[74] D. Y. Lee, and K. Vafai. Analytical characterization and conceptual assessment of solid and fluid temperature differentials in porous media, Int. J. Heat Mass Transf. 42 (1999) 423–435.

[75] S. Mahjoob, and K. Vafai, Analysis of bioheat transport through a dual layer biological media, ASME J Heat Transf. 132 (2010) 031101-14.

[76] S. Mahjoob, and K. Vafai, Analysis of Heat Transfer in Consecutive Variable Cross-Sectional Domains: Applications in Biological Media and Thermal Management, ASME J Heat Transf. 133 (2011) 011006-1-9.

[77] L. A. Dombrovsky, V. Timchenko, M. Jackson, and G. H. Yeoh, A combined transient thermal model for laser hyperthermia of tumors with embedded gold nanoshells, Int. J. Heat Mass Transf. 54 (2011) 5459-5469.

[78] L. A. Dombrovsky, V. Timchenko, and M. Jackson, Indirect heating strategy for laser induced hyperthermia: An advanced thermal model, Int. J. Heat Mass Transf. 55 (2012) 4688-4700.

[79] P. Keangin, and P. Rattanadecho, Analysis of heat transport on local thermal non-equilibrium in porous liver during microwave ablation, Int. J. Heat Mass Transf. 67 (2013) 46-60.

[80] P. Keangin, and P. Rattanadecho, Numerical study of heat transfer and blood flow in two-layered porous liver tissue during microwave ablation process using single and double slot antenna, Int. J. Heat Mass Transf. 58 (2013) 457-470.

[81] K. Wang, F. Tavakkoli, S. Wang, and K. Vafai, Analysis and analytical characterization of bioheat transfer during radiofrequency ablation, J. Biomech. 48 (2015) 930-940.

[82] D. C. M. Vyas, S. Kumar, and A. Srivastava, Porous media based bio-heat transfer analysis on counter-current artery vein tissue phantoms: applications in photo thermal therapy, Int. J. Heat Mass Transf. 99 (2016) 122-140.

[83] K. C. Liu, H. T. Chen, Analysis for the dual-phase-lag bio-heat transfer during magnetic hyperthermia treatment, Int. J. Heat Mass Tran. 52 (2009) 1185-1192.

[84] D. K. Kumar, and K. N. Rai, Numerical simulation of time fractional dual-phase-lag model of heat transfer within skin tissue during thermal therapy, J. Therm. Biol. 67 (2017) 49-58.

[85] K. Khanafer, J. L. Bull, I. Pop, and R. Berguer, Influence of pulsatile blood flow and heating scheme on the temperature distribution during hyperthermia treatment, Int. J. Heat Mass Transf. 50 (2007) 4883–4890.

[86] M. Nabil, P. Decuzzi, and P. Zunino, Modelling mass and heat transfer in nano-based cancer hyperthermia, R. Soc. Open Sci. 2 (2015 150447.

[87] M. Nabil, and P. Zunino, A computational study of cancer hyperthermia based on vascular magnetic nanoconstructs, R. Soc. Open Sci. 3 (2016) 160287.

[88] J. Crezee, and J. J. W. Lagendijk, Temperature uniformity during hyperthermia: the impact of large vessels, Phys. Med. Biol. 37 (1992) 1321-37.

[89] J. C. Chato, Heat transfer to blood vessels, J. Biomech. Eng. -T ASME 102 (1980) 110-118.

[90] H. S. Kou, T. C. Shih, and W. L. Lin, Effect of the directional blood flow on thermal dose distribution during thermal therapy: an application of a Green's function based on the porous model, Phys. Med. Biol. 48 (2003) 1577-1589.

[91] F. A. Duck, A. C. Baker, and H. C. Starrit, Ultrasound in medicine, London: Institute of Physics Publishing, (1998) 57-88.

[92] A. Vera, and L. Leija, Microcoaxial Double slot antenna for interstitial hyperthermia: design, modeling and validation, in: International Conference on Advances in Electronics and Micro-electronics ENICS2008 (2008) 138-143.

[93] C. Yang, and A. Nakayama, A synthesis of tortuosity and dispersion in effective thermal conductivity of porous media, Int. J. Heat Mass Transf. 53 (2010) 3222-3230.

[94] A. Nakayama, Y. Sano, and K. Yoshikawa, A rigorous derivation of the bioheat equation for local tissue heat transfer based on a volume averaging theory, Heat Mass Transf. 46 (2010) 739-746.

[95] A. Nakayama, F. Kuwahara, and W. Liu, A Macroscopic Model for Countercurrent Bioheat Transfer in a Circulatory System, J. Porous Media 12 (2009) 289-300.

[96] R. Hoffmann, H. Rempp, L. Erhard, G. Blumenstock, P. L. Pereira, C. D. Claussen, S. Clasen, Comparison of four microwave ablation devices: an experimental study in ex vivo bovine liver, Radiology 268 (2013) 89-97.

[97] R. C. Simpson, M. Kohl, M. Essenpreis, and M. Cope, Near-infrared optical properties of ex vivo human skin and subcutaneous tissues measured using the Monte Carlo inversion technique, Phys. Med. Biol. 43 (1998) 2465–2478.

[98] M. E. Sluijter, Non-thermal radiofrequency procedures in the treatment spinal pain," Pain in Europe. Barcelona: 2nd Annual Congress of the European Federation of IASP Chapters, 326 (1997).

[99] M. E. Sluijter, Principles of radiofrequency lesions and strategy for treatment, First Maastricht Workshop on Radiofrequency in the Treatment of Spinal Pain, Maastricht, (1997) 9–14.

[100] R. Munglani, The longer-term effect of pulsed radiofrequency for neuropathic pain, Pain 80 (1999) 437-439.

[101] S. P. Cohen, and A. Foster, Pulsed radiofrequency as a treatment for groin pain and orchialgia, Urology 61 (2003) 645xxi-645xxiii.

[102] D. R. Emril, and K. Y. Ho, Treatment of trigeminal neuralgia: role of radiofrequency ablation, J. Pain Res. 3 (2010) 249-254.

[103] A. Asopa, Systematic review of radiofrequency ablation and pulsed radiofrequency for management of cervicogenic headache, Pain physician 18 (2015) 109-130.

[104] S. K. Wu, C. F. Chiang, Y. H. Hsu, H. C. Liou, W. M. Fu, W. L. Lin, Pulsed-wave low-dose ultrasound hyperthermia selectively enhances nanodrug delivery and improves antitumor efficacy for brain metastasis of breast cancer,

Ultrason. Sonochem. 36 (2017) 198-205.

[105] S. N. Goldberg, M. C. Stein, G. S. Gazelle, R. G. Sheiman, J. B. Kruskal, M. E. Clouse, Percutaneous radiofrequency tissue ablation: optimization of pulsed-radiofrequency technique to increase coagulation necrosis, J. Vasc. Interv. Radiol. 10 (1999) 907-916.

[106] M, Ahmed, S. M. Lobo, J. Weinstein, J. B. Kruskal, G. S. Gazelle, E. F. Halpern, S. K. Azfal, R. E. Lenkinski, S. N. Goldberg, Improved coagulation with saline solution pretreatment during radiofrequency tumor ablation in a canine model, J. Vasc. Interv. Radiol. 13 (2002) 717-724.

[107] J. A. López Molina, M. J. Rivera, M. Trujillo, E. J. Berjano, Thermal modeling for pulsed radiofrequency ablation: analytical study based on hyperbolic heat conduction, Med. Phys. 36 (2009) 1112-1119.

[108] T. Fukushima, K. Ikeda, Y. Kawamura, Y. Sorin, T. Hosaka, M. Kobayashi, S. Saitoh, H. Sezaki, N. Akuta, F. Suzuki, Y. Suzuki, Y. Arase, H. Kumada, Randomized controlled trial comparing the efficacy of impedance control and temperature control of radiofrequency interstitial thermal ablation for treating small hepatocellular carcinoma, Oncology 89 (2015) 47-52.

[109] M. Trujillo, J. Bon, M. José Rivera, F. Burdío, E. Berjano, Computer modelling of an impedance-controlled pulsing protocol for RF tumour ablation with a cooled electrode, Int. J. Hyperther. 32 (2016) 931-939.

[110] B. Zhang, M. A. Moser, E. M. Zhang, Y. Luo, W. Zhang, Numerical analysis of the relationship between the area of target tissue necrosis and the size of target tissue in liver tumours with pulsed radiofrequency ablation, Int. J. Hyperther. 31 (2015) 715-725.

[111] M. Bedoya, A. M, del Rio, J. Chiang, C. L. Brace, Microwave ablation energy delivery: influence of power pulsing on ablation results in an ex vivo and in vivo liver model, Med. Phys. 41 (2014).

[112] G. Biffi Gentili, C. Ignesti, Dual applicator thermal ablation at 2.45 GHz: a numerical comparison and experiments on synchronous versus asynchronous and switched-mode feeding, Int. J. Hyperther. 31 (2015) 528-537.

[113] B. Dietrich, W. Schabel, M. Kind, H. Martin, Pressure drop measurements of ceramic sponges determining the hydraulic diameter, Chem. Eng. Sci. 64 (2009) 3633-3640.

[114] M. Iasiello, S. Cunsolo, N. Bianco, V. Naso, M. Oliviero, W. M. Harris, W. K. S. Chiu, Forced convective heat transfer in metal foams: the characteristic length issue, Proc. of 3rd Int. Conf. On Comput. Methods for Therm. Problems (2014) 117-120.

[115] J. M. Cooper, J. L. Sapp, U. Tedrow, C. P. Pellegrini, D. Robinson, L. M. Epstein, W. G. Stevenson, Ablation with an internally irrigated radiofrequency catheter: learning how to avoid steam pops, Heart. Rhythm. 1 (2004) 329-333.

[116] B. Zhang, M. A. Moser, E. M. Zhang, Y. Luo, H. Zhang, W. Zhang, Study of the relationship between the target tissue necrosis volume and the target tissue size in liver tumours using two-compartment finite element RFA modelling, Int.

J. Hyperther. 30 (2014) 593–602.

[117] M. Nikfarjam, V. Muralidharan, C. Christophi, Mechanisms of Focal Heat Destruction of Liver Tumors, J. Surg. Res. 127 (2005) 208-223.

[118] G. Reddy, M. R. Dreher, C. Rossmann, B. J. Wood, D. Haemmerich D, Cytotoxicity of hepatocellular carcinoma cells to hyperthermic and ablative temperature exposures: In vitro studies and mathematical modelling, Int. J. Hyperther. 29 (2013) 318–323.

[119] D. Haemmerich, L. Chachati, A.S. Wright, D.M. Mahvi, F.T. Lee, J.G. Webster, Hepatic radiofrequency ablation with internally cooled probes: effect of coolant temperature on lesion size, IEEE Trans. Biomed. Eng. 50 (2003) 493-499.

[120] J.P. Abraham, E.M. Sparrow, A thermal-ablation bioheat model including liquid-to-vapor phase change, pressure- and necrosis-dependent perfusion, and moisture-dependent properties, Int. J. Heat. Mass Transf. 50 (2007) 2537-2544.

[121] T. Pätz, T. Kröger, T. Preusser, Simulation of radiofrequency ablation including water evaporation, IFMBE Proc. 25/IV (2009) 1287-1290.

[122] M. Trujillo, J. Alba, E. Berjano, Relation between roll-off occurrence and spatial distribution of dehydrated tissue during RF ablation with cooled electrodes, Int. J. Hyperthermia 28 (2012) 62-68.

[123] S. Jacques, S. Rastegar, S. Thomsen, M. Motamedi, The role of dynamic changes in blood perfusion and optical properties in laser coagulation tissue, IEEE J. Sel. Top Quantum Electron. 2 (1996) 922-933.

[124] S.K. Hall, E.H. Ooi EH, S.J. Payne, Cell death, perfusion and electrical parameters are critical in models of hepatic radiofrequency ablation, Int. J. Hyperthermia 31 (2015) 538-550.

[125] H.Q. Woodard, D.R. White, The composition of body tissues, Br. J. Radiol. 59 (1986) 1209-1219.

[126] H. Taniguchi, M. Masuyama, H. Koyama, A. Oguro, T. Takahashi, Quantitative measurement of human tissue hepatic blood volume by C15O inhalation with positron-emission tomography, Liver 16 (1996) 258-262.

[127] E.L. Dobson, G.F. Warner, C.R. Finney, M.E. Johnston, The Measurement of Liver Circulation by Means of the Colloid Disappearance Rate, Circulation 7 (1953) 690-695.

[128] H.C. Schwickert, T.P.L. Roberts, D.M. Shames, C.F. Van Dijke, A. Disston, A. Mühler, J.S. Mann, R.C. Brasch, Quantification of liver blood volume: comparison of ultra short ti inversion recovery echo planar imaging (ulstir-epi), with dynamic 3d-gradient recalled echo imaging, Magn. Reason. Med. 34 (1995) 845-852.

[129] C.A. Cuenod, D. Balvay, Perfusion and vascular permeability: Basic concepts and measurement in DCE-CT and DCE-MRI, Diagn. Interv. Imaging 94 (2013) 1187-1204.

[130] C. Brace, Thermal Tumor Ablation in Clinical Use, IEEE Pulse 2 (2011) 28-38.

[131] E. E. Stewart, X. Chen, J. Hadway, T. Y. Lee, Correlation between Hepatic Tumor Blood Flow and Glucose Utilization in a Rabbit Liver Tumor Model, Radiology 239 (2006) 740-750.

[132] P. Keangin, K. Vafai, P. Rattanadecho, Electromagnetic field effects on biological materials, Int. J. Heat Mass Transf. 65 (2013) 389-399.

[133] Y. He, H. Liu, R. Himeno, J. Sunaga, N. Kakusho, H. Yokota, Finite element analysis of blood flow and heat transfer in an image-based human finger, Comput. Biol. Med. 38 (2008) 555–562.

[134] R. P. Gilbert, Y. Liu, J. P. Groby, E. Ogam, A. Wirgin, Y. Xu, Computing porosity of cancellous bone using ultrasonic waves. II: The muscle, cortical, cancellous bone system, Math. Comput. Model. 50 (2009) 421-429.

[135] T. Wessapan, P. Rattanadecho, Specific absorption rate and temperature increase in human eye subjected to electromagnetic fields at 900 MHz, ASME J. Heat Transf. 134 (2012) 91101-1–91101-11.

[136] R. M. Effros, J. Lowenstein, D. S. Baldwin, F. P. Chinard, Vascular and extravascular volumes of the kidney of man, Circ. Res. 20 (1967) 162-173.

[137] K. Giering, O. Minet, I. Lamprecht, G. Müller, Review of thermal properties of biological tissues, Proceedings of SPIE – The International Society for Optical Engineering, (2015) 45-65.

[138] S. Laufer, A. Ivorra, V. E. Reuter, B. Rubinsky, S. B. Solomon, Electrical impedance characterization of normal and cancerous human hepatic tissue, Physiol. Meas. 31 (2010) 995-1009.

[139] M. Trujillo, E. Berjano, Review of the mathematical functions used to model the temperature dependence of electrical and thermal conductivities of biological tissue in radiofrequency ablation, Int. J. Hyperther. 29 (2013) 590-597.

[140] D. Haemmerich, S. T. Staelin, J. Z. Tsai, S. Tungjitkusolmun, D. M. Mahvi, J. G. Webster, In vivo electrical conductivity of hepatic tumours, Physiol. Meas. 24 (2003) 251-260.

[141] S. R. Smith, K. R. Foster, G. L. Wolf, Dielectric Properties of VX-2 Carcinoma Versus Normal Liver Tissue, IEEE Trans. Biomed. Eng. BME-33 (1986) 522-524.

[142] C. M. Harari, M. Magagna, M. Bedoya, F. T. Lee Jr, M. G. Lubner, J. L. Hinshaw, C. L. Brace, Microwave ablation: comparison of simultaneous and sequential activation of multiple antennas in liver model systems, Radiology 278 (2015) 95-103.

[143] C. L. Brace, P. F. Laeseke, L. A. Sampson, T. M. Frey, D. W. van der Weide, F. T. Lee Jr, Microwave ablation with multiple simultaneously powered small-gauge triaxial antennas: results from an in vivo swine liver model, Radiology 244 (2007) 151-156.

[144] A. Andreozzi, M. Iasiello, C. Tucci, An overview of mathematical models and modulated-heating protocols for thermal ablation, Adv. Heat Transf. (2020) Article in Press.

[145] A. Andreozzi, L. Brunese, M. Iasiello, C. Tucci, G. P. Vanoli, Modeling heat transfer in tumors: a review of thermal therapies, Ann. Biomed. Eng. 47 (2019) 676-693.

[146] A. Andreozzi, L. Brunese, M. Iasiello, C. Tucci, G. P. Vanoli, Bioheat transfer in a spherical biological tissue: a comparison among various models, J. Phys. (2019, May) Conference Series (Vol. 1224, No. 1, p. 012001). IOP Publishing.

[147] A. Andreozzi, L. Brunese, M. Iasiello, C. Tucci, G. P. Vanoli, Numerical analysis of the pulsating heat source effects in a tumor tissue, Comput. Methods Programs Biomed. 200 (2021) 105887.

[148] C. Tucci, M. Trujillo, E. Berjano, M. Iasiello, A. Andreozzi, G. P. Vanoli, Pennes' bioheat equation vs. porous media approach in computer modeling of radiofrequency tumor ablation, Sci. Rep. 11 (2021), 1-13.

[149] A. Andreozzi, L. Brunese, M. Iasiello, C. Tucci, G. P. Vanoli, A novel local thermal non-equilibrium model for biological tissue applied to multiple-antennas configurations for thermal ablation, Num. Heat Transf. A- Appl. 79 (2020) 111-121.